



HAL
open science

Tomography of subduction zones using regional earthquakes: methodological developments and application to the Ionian slab.

Marco Calo'

► **To cite this version:**

Marco Calo'. Tomography of subduction zones using regional earthquakes: methodological developments and application to the Ionian slab.. Geophysics [physics.geo-ph]. Université de Strasbourg, 2009. English. NNT: . tel-00438598

HAL Id: tel-00438598

<https://theses.hal.science/tel-00438598>

Submitted on 16 Jan 2013

HAL is a multi-disciplinary open access archive for the deposit and dissemination of scientific research documents, whether they are published or not. The documents may come from teaching and research institutions in France or abroad, or from public or private research centers.

L'archive ouverte pluridisciplinaire **HAL**, est destinée au dépôt et à la diffusion de documents scientifiques de niveau recherche, publiés ou non, émanant des établissements d'enseignement et de recherche français ou étrangers, des laboratoires publics ou privés.



Thèse en cotutelle

*présentée pour obtenir le grade de Docteur de
l'Université de Strasbourg et de l'Université de Messine
par*

Marco Calò

**Tomography of subduction zones using regional
earthquakes: methodological developments and
application to the Ionian slab.**

**Tomographie des zones en subduction en utilisant les
séismes locaux: développements méthodologiques et
applications pratiques à la plaque Ionienne.**

Soutenue publiquement le 19 mars 2009

Discipline : Géophysique / Geofisica per l'Ambiente e il Territorio XXI ciclo

Directeur de Thèse :	Dr. Catherine Dorbath	E.O.S.T. Strasbourg
Co-directeur de Thèse :	Pr. Dario Luzio	C.F.T.A. Palermo
Rapporteur Interne :	Pr. Frédéric Masson	I.P.G. Strasbourg
Rapporteur Externe :	Dr. Serge Lallemand	C.N.R.S. Montpellier
Rapporteur Externe :	Pr. Attilio Sulli	Dip. di Geologia Palermo
Examineur :	Pr. Domenico Schiavone	Dip. di Geologia Bari
Examineur :	Pr. Maurizio Fedi	Dip. di Scienze della Terra Napoli

To my love,
and to my grandparents.

Résumé

Dans les modèles géodynamiques les plus couramment admis, la sismicité intermédiaire et profonde de la zone Tyrrhénienne méridionale et de l'arc de la Calabre a été attribuée à un processus assez développé de subduction de la lithosphère océanique, où la lithosphère Ionienne s'enfonce sous la lithosphère de la mer Tyrrhénienne amincie, jusqu'à environ 500 km de profondeur. L'archipel des îles Éoliennes et les monts sous-marins voisins sont aussi associés au processus de subduction, et la Mer Tyrrhénienne méridionale interprétée comme bassin arrière-arc.

L'hétérogénéité des mécanismes des sources sismiques présentes dans la Mer Tyrrhénienne méridionale, en Sicile et en Calabre témoigne de la complexité du processus géodynamique en cours. L'étude de cette zone présente encore de nombreuses questions ouvertes, dues aux connaissances limitées des unités géologiques sur lesquels agissent les forces, et en particulier au détail insuffisant des modèles géophysiques de la lithosphère.

Les techniques tomographiques utilisées jusqu'aujourd'hui dans la région tyrrhénienne ont contribué à déterminer à grande échelle les structures géologiques de la croûte et du manteau supérieur, mais elles n'ont pas une résolution suffisante pour distinguer les différentes unités qui les constituent.

De plus, souvent, les analyses de la fiabilité des estimations de vitesse et de la stabilité du problème inverse traité, qui sont des paramètres fondamentaux pour une étude géophysique, sont peu développées.

La reconstruction détaillée de la géométrie actuelle de la subduction Ionienne et des structures de la lithosphère de la Mer Tyrrhénienne méridionale et de l'Italie sud-occidentale pourrait fournir d'importants apports pour la définition d'un modèle cinématique évolutif de la mer Tyrrhénienne entière. En outre, la détermination et la description détaillée des structures responsables de l'activité sismique présente dans le secteur Calabro-Sicilien et les bassins environnants pourraient apporter des contributions considérables à la modélisation de la sismicité dans les domaines de l'espace, du temps et de la magnitude.

L'étude détaillée des structures lithosphériques et intramantelliques présentes dans cette partie de l'Italie méridionale a été réalisée, pendant cette thèse de doctorat, en effectuant une tomographie sismique tridimensionnelle à résolution élevée en ondes de volume.

Les principaux développements de cette thèse peuvent être résumés en trois principales sections: dans la première, qui comprend les chapitres 1 et 2, on retrace synthétiquement l'histoire de la tomographie sismique et les méthodes proposées pendant les vingt dernières années. Le deuxième chapitre est entièrement dédié à l'explication du programme d'inversion *TomoDD* (*Zangh and Thurber, 2003*), choisi pour réaliser les premiers images tomographiques, qui utilise la méthode de la double-différence pour l'obtention de la solution du problème inverse tomographique.

Dans la deuxième partie (chapitres 3 et 4), on développe les aspects méthodologiques et théoriques pour la réalisation d'une tomographie à haute résolution en mettant en oeuvre une nouvelle technique de post-processing appelée WAM (Weighted Average Model).

Comme données expérimentales, on a utilisé les enregistrements des tremblements de terre s'étant produits en Italie méridionale depuis 1981 jusqu'en 2005, effectués par les stations du réseau sismique national italien et des réseaux locaux. Seuls les séismes enregistrés par plus de 10 stations, et localisés avec un RMS (Root Mean Square) inférieur à 0.5 s avec un modèle 1D optimal de la région d'étude, ont été sélectionnés pour la réalisation de la tomographie.

Cette partie du travail de thèse a visé à la réalisation des nombreux tests avec des données synthétiques et des données expérimentales, pour évaluer la dépendance du modèle final d'une tomographie « DD classique » aux paramètres initiaux.

En particulier, on a appliqué le « resolution restoration test » (*Zhao et al., 1992*) comme test synthétique pour évaluer la capacité des données sélectionnées à reconstruire la distribution du champ de vitesse obtenu par une inversion expérimentale. La dépendance du modèle final aux conditions initiales a été évaluée en réalisant trois types de tests expérimentaux : 1) estimation de la dépendance du modèle de vitesse final à la grille d'inversion utilisée en faisant plusieurs inversions en changeant la géométrie de la grille; 2) estimation de la dépendance du modèle final au modèle initial en faisant des inversions tomographiques avec différents modèles initiaux 1D et 3D ; 3) estimation de la dépendance du modèle final à la sélection des données expérimentales et au système de pondération entre les données absolues et relatives en faisant de multiples inversions en changeant les règles de sélection des données et le système de pondération.

Tous les tests ont démontré qu'une inversion tomographique réalisée en utilisant les données et la méthode choisie produisent des modèles 3D de vitesse V_p et V_s très détaillés et fiables pour la description de la géométrie des corps présents jusqu'à la profondeur de 350 km. Par contre, l'estimation des valeurs absolues de vitesse dans certaines parties des modèles a montré une variabilité et une dépendance aux conditions initiales qui ne permettaient pas d'utiliser les résultats pour en faire une interprétation pétrologique. Pour surmonter ces limitations, on a imaginé de réaliser un modèle moyen pratiquement indépendant des conditions initiales et donc plus fiable. La construction du modèle moyen est réalisée en faisant un re-échantillonnage des nombreux modèles de vitesse, déjà produits avec tomoDD, dans un grille fixée (WAM grid), en utilisant la même règle d'interpolation que celle utilisée par le programme de tomographie. Dans notre cas la règle d'interpolation est tri-linéaire. Les valeurs de DWS (Derivative Weight Sum, *Toomey and Foulger, 1989*), paramètre lié à la quantité d'information expérimentale utilisée pour estimer la valeur de la vitesse à chaque nœud du modèle, sont aussi interpolées dans un grille identique. La valeur de DWS a été utilisée comme facteur de pondération dans le calcul de la vitesse moyenne, ainsi dans les nœuds de la WAM grid on pourra donner plus de poids à une valeur de vitesse estimée avec plus de résolution pendant les inversions tomographiques.

Les valeurs de la déviation standard et la DWS du modèle WAM sont calculées avec la même méthode.

Pour évaluer l'efficacité de la méthode de pondération et la validité du modèle de vitesse WAM, on a réalisé un test synthétique de type échiquier intégré avec l'estimation d'un paramètre de restauration (R) qui donne une estimation quantitative (exprimée en %) de la capacité de reconstruction du modèle. De plus, en comparant la distribution de R et la déviation standard, on a pu vérifier qu'il existe une loi d'anti-corrélation entre ces deux paramètres: dans les parties du modèle synthétique WAM où l'on trouve des hautes valeurs de déviation standard on trouve des faibles valeurs de R et vice versa. Par ce moyen, on a pu lier directement le paramètre quantitatif du pouvoir de restauration (R) à la déviation standard du modèle expérimental WAM.

En principe, la méthode WAM, étant un post-processing, pourrait être utilisée avec chaque programme de tomographie, permettant ainsi d'obtenir une plus grande fiabilité des modèles pour leur interprétation.

Dans la troisième partie de la thèse (chapitres 5 et 6), on a appliqué la méthode WAM à l'Italie du Sud. La grande fiabilité du modèle WAM obtenu avec une haute résolution a nous permis la reconstruction de la géométrie des corps intérieurs au slab Ionien et au manteau tyrrhénien. La première caractéristique des modèles WAM pour les vitesses des ondes P et S est la présence de corps à faible vitesse ($7.0 < V_p < 7.7$ km/s et $3.8 < V_s < 4.2$

km/s) jusqu'à la profondeur de 220-250 km dans le slab en subduction par ailleurs caractérisé par des valeurs hautes ($8.2 < V_p < 8.8$ km/s et $4.75 < V_s < 5$ km/s).

Ces corps ont des dimensions variables, entre 15 et 35 km de largeur et 35 à 55 km de longueur, et sont compatibles avec zones de la lithosphère ionienne serpentinisées à 20-30 % (*Christensen, 2004*).

L'hydratation de l' harzburgite à serpentine est provoquée par une partie des fluides du slab qui migrent dans la lithosphère par des zones plus poreuses comme les « fault bends ».

L'inclinaison du slab joue un rôle dominant pour la répartition des fluides qui migrent soit dans la lithosphère même soit dans le manteau autour (*Abers, 2005*).

A des profondeurs plus grandes, les conditions de température et pression font que le processus de déshydratation transforme les minéraux de la serpentine en phases de plus haute pression comme la phase « A » qui a des caractéristiques très similaires à l' harzburgite anhydre (*Fumagalli and Poli, 2005; Hacker et al., 2003*).

Avec le WAM on a pu reconstruire la forme 3D du slab Ionienne et mettre en évidence sa géométrie très particulière qui peut être comparée à un *sablier* incliné de 69° - 72° vers le N-W.

Dans le manteau Tyrrhénien, jusqu'à la profondeur de 180 km, on peut remarquer d'importantes zones caractérisées par des faibles valeurs de vitesse soit des ondes P soit des ondes S, qui suggèrent la présence de grandes quantités de matériaux partiellement en fusion au dessous des volcans actifs présents dans le bassin (Stromboli et Marsili). On pense que ces corps à faible vitesse sont des zones de production de magma déclenchée par une partie des fluides migrés du slab en subduction.

De plus, dans le WAM des ondes S, on peut remarquer des corps à faible vitesse à profondeur lithosphérique (20-40 km), juste au dessous du mont sous-marin Marsili et du volcan Stromboli, interprétés comment de probables zones d'accumulation du magma qui migre vers la surface.

La possibilité de mettre en relation les considérations pétrologiques avec des modèles de vitesse détaillés a permis de formuler un nouveau modèle de circulation du manteau dans la région d'étude.

Enfin, dans un dernier chapitre sont présentées certaines potentialités de la méthode WAM dans notre région d'étude qui montrent la possibilité de construire des modèles à grande échelle en préservant haute résolution et fiabilité.

RIASSUNTO

All'interno dei quadri geodinamici oggi più accreditati, la sismicità intermedia e profonda dell'area tirrenica meridionale e dell'arco Calabro, è stata attribuita ad un processo abbastanza sviluppato di subduzione di litosfera oceanica, nel quale la placca ionica subduce al di sotto della litosfera assottigliata tirrenica, fino a circa 500 km di profondità. L'arcipelago delle isole Eolie e i seamounts vicini vengono anch'essi associati al processo di subduzione e il mar Tirreno meridionale interpretato come bacino di retro-arco. L'eterogeneità dei meccanismi delle sorgenti sismiche presenti nel mar Tirreno meridionale, nella Sicilia e nella Calabria testimoniano la complessità del processo geodinamico in corso.

Lo studio di questa area presenta ancora numerosi problemi aperti a causa delle limitate conoscenze dei corpi geologici sui quali agiscono gli sforzi tettonici ed in particolare dell'insufficiente dettaglio dei modelli geofisici della litosfera. Le tecniche tomografiche utilizzate fino ad oggi nell'area tirrenica hanno contribuito ad individuare le principali strutture geologiche della crosta e del mantello superiore, ma non hanno un potere risolutivo adeguato per discriminare le diverse unità che le costituiscono.

Spesso, inoltre, le analisi di l'affidabilità delle stime di velocità e di stabilità del problema inverso affrontato, che sono parametri fondamentali per uno studio di natura geofisica, sono svolte in maniera molto approssimativa.

La ricostruzione dettagliata delle caratteristiche geometriche attuali dello slab ionico e delle strutture crostali del mar Tirreno meridionale e dell'Italia sud-occidentale potrebbe fornire importanti vincoli per la definizione di un modello cinematico-evolutivo dell'intera area tirrenica. Inoltre l'individuazione e la descrizione dettagliata delle strutture responsabili dell'attività sismica presenti nel settore calabro-siciliano e dei bacini circostanti potrebbero apportare notevoli contributi alla modellazione della sismicità nei domini dello spazio, del tempo, e della magnitudo e quindi alla mitigazione del rischio sismico.

In questa tesi di dottorato lo studio dettagliato delle strutture litosferiche e inframantelliche presenti nel Tirreno meridionale è stato realizzato effettuando una tomografia sismica tridimensionale ad elevata risoluzione con onde di volume.

Gli argomenti della tesi possono essere riassunti in tre sessioni principali: nella prima, che comprende i capitoli 1 e 2, si ripercorre brevemente la storia della tomografia sismica e le metodologie proposte negli ultimi vent'anni. Il secondo capitolo è interamente rivolto alla descrizione del programma di inversione *TomoDD* (Zangh and Thurber, 2003), scelto per realizzare le prime immagini tomografiche e che utilizza il metodo della 'doppia-differenza' per la soluzione del problema inverso tomografico.

Nella seconda parte della tesi (capitoli 3 e 4) si sono approfonditi alcuni aspetti metodologici e teorici che hanno permesso l'implementazione di un nuovo metodo di post-processing chiamato WAM (Weighted Average Model) per la realizzazione di modelli tridimensionali di velocità affidabili e ad elevata risoluzione.

Come dati sperimentali si sono utilizzate le registrazioni dei terremoti avvenuti in Italia meridionale dal 1981 al 2005 effettuate dalle stazioni della rete sismica nazionale e di alcune reti locali. Sono stati selezionati solo gli eventi registrati da almeno 10 stazioni e localizzati con un modello 1D ottimizzato per la regione di studio con un RMS (Root Mean Square) inferiore a 0.5s.

In questa parte di tesi sono mostrati i numerosi test, realizzati sia con tempi calcolati che con tempi sperimentali, per valutare la dipendenza del modello finale di una tomografia "DD classica" dai parametri iniziali che è necessario imporre in uno studio tomografico.

In particolare, si mostrano i risultati del test sintetico “restoration resolution test” (Zhao *et al.*, 1992) realizzato per valutare la capacità dei dati selezionati a ricostruire la distribuzione del campo di velocità ottenuto precedentemente mediante un’ inversione dei dati sperimentali. La dipendenza del modello finale dai parametri di input è stata invece valutata mediante la realizzazione di tre tipi di test sperimentali: 1) stima della dipendenza del modello finale di velocità dalla griglia di inversione utilizzata, realizzando numerose inversioni deformando e cambiando la geometria della griglia ; 2) stima della dipendenza del modello finale dal modello iniziale, realizzando inversioni con differenti modelli iniziali 1-D e 3-D; 3) stima della dipendenza del modello finale dalle regole di selezione dei dati sperimentali e dal sistema di pesi tra dati *assoluti* e dati *relativi*, realizzando inversioni cambiando le regole di selezione dei dati assoluti e i sistemi di ponderazione.

Tutti i test mostrano come un’ inversione tomografica realizzata utilizzando i dati e il metodo scelti produce modelli 3-D di velocità V_p e V_s molto dettagliati e affidabili per la descrizione della geometria dei corpi presenti nell’ area fino ad una profondità di 350 km.

Tuttavia, la stima dei valori assoluti di velocità in alcune parti del modello mostra una variabilità ed una dipendenza dai parametri di input che ne riducono l’ affidabilità limitando le possibilità di poter effettuare considerazioni di natura petrologica. Per superare queste limitazioni del modello si è pensato di realizzare un modello medio di velocità praticamente indipendente dai parametri di input e quindi più affidabile. La costruzione del modello medio è stata realizzata effettuando un ricampionamento dei numerosi modelli di velocità, già prodotti con tomoDD, in una griglia fissa (WAM grid) utilizzando la stessa regola di interpolazione utilizzata dal programma di tomografia. In tomoDD la regola di interpolazione è di tipo trilineare. I valori di DWS (Derivative Weight Sum, *Toomey and Foulger, 1989*), parametro legato alla quantità di informazione sperimentale utilizzata per stimare il valore di velocità in ciascun nodo della griglia, sono stati interpolati su una griglia identica. Il valore di DWS è stato utilizzato come fattore di ponderazione durante il calcolo della velocità media, in tal modo ai nodi della WAM grid è stato possibile assegnare un peso maggiore ai valori stimati con maggiore informazione sperimentale durante le inversioni tomografiche. Con lo stesso metodo si sono determinati i valori della deviazione standard e delle DWS pesate. Per valutare l’ efficacia del sistema di ponderazione e la validità del modello medio di velocità si è realizzata una versione estesa del checkerboard test integrandolo con un parametro (R) che determina la capacità percentuale di ricostruzione di un modello sintetico dopo un’ inversione. Inoltre, si è osservato che esiste una legge di anticorrelazione tra la distribuzione dei valori di R e quella della deviazione standard: nelle porzioni del WAM sintetico caratterizzate da elevati valori di deviazione standard si osservano bassi valori di R e vice versa. In questo modo è stato possibile trovare un legame diretto tra un parametro quantitativo capace di stimare il grado di ricostruzione di un modello sintetico (R) e la deviazione standard di un WAM sperimentale. In principio, il metodo WAM, essendo una procedura di post-processing, potrebbe esser utilizzata con qualsiasi programma di inversione tomografica offrendo la possibilità di ottenere modelli di velocità più affidabili.

Nella terza parte della tesi (capitoli 5 e 6) si mostra l’ applicazione del metodo WAM ai dati sperimentali relativi ai terremoti avvenuti nell’ Italia meridionale. La grande affidabilità dei WAM (V_p e V_s) e la loro elevata risoluzione hanno permesso la ricostruzione delle geometrie dei corpi interni allo slab Ionico e al mantello tirrenico. La caratteristica principale dei modelli WAM delle V_p e V_s è la presenza di corpi caratterizzati da bassi valori di velocità ($7.0 < V_p < 7.7$ km/s e $3.8 < V_s < 4.2$ km/s) rintracciabili fino ad una profondità di 220-250 km all’ interno dello slab in subuzione che è caratterizzato da alti valori di velocità ($8.2 < V_p < 8.8$ km/s e $4.75 < V_s < 5$ km/s). Questi corpi hanno dimensioni variabili tra 15 km e 35 km di larghezza e hanno velocità delle onde sismiche compatibili con quelle di una litosfera serpentizzata che può raggiungere il 20-30% vol. (*Christensen, 2004*). L’ idratazione dell’ harzburgite in serpentino è

provocata da una parte dei fluidi rilasciati dallo slab che migrano all'interno della litosfera Ionica attraverso zone a maggiore "permeabilità" come le "fault bends". L'inclinazione dello slab ha un ruolo dominante sulla ripartizione dei fluidi che migrano sia all'interno della litosfera stessa sia nel mantello circostante (Abers, 2005). A maggiori profondità l'aumento della pressione e della temperatura permettono il completamento dei processi di disidratazione trasformando i minerali del serpentino in fasi di più alta pressione come la fase "A" che presenta caratteristiche sismiche simili a quelle dell'harzburgite anidra (Fumagalli and Poli, 2005; Hacker et al., 2003).

Grazie al metodo WAM è stato possibile ricostruire dettagliatamente la forma tridimensionale dello slab Ionico e mettere in luce la sua geometria che potrebbe essere paragonata a quella di una *clessidra* asimmetrica inclinata 69° - 72° in direzione N-W.

Nel mantello tirrenico, fino a profondità di 180 km si possono individuare regioni caratterizzate da bassi valori di velocità sia delle onde P che delle onde S che suggeriscono la presenza di grandi volumi di mantello parzialmente fuso sotto i vulcani attivi presenti nel bacino sud tirrenico (Stromboli e Marsili). Parte di questi corpi potrebbero essere prodotti da una parte dei fluidi rilasciati dallo slab in subduzione.

Inoltre, nel WAM relativo alle velocità delle onde S è possibile riconoscere corpi caratterizzati da bassi valori di velocità a profondità litosferiche (20-40 km), in corrispondenza del bacino del Marsili e del Vulcano Stromboli. Tali anomalie sono state interpretate come probabili zone di accumulo di magmi che migrano verso la superficie. La possibilità di mettere in relazione evidenze petrologiche con i modelli di velocità ha permesso di formulare un nuovo modello sulla cinematica del mantello nella regione di studio.

Infine, in un ultimo capitolo, si mostrano alcune peculiarità del metodo WAM che può essere utilizzato per costruire modelli di velocità a grande scala mantenendo inalterate le caratteristiche di affidabilità e risoluzione dei modelli prodotti.

Abstract

Most of the geodynamic models ascribe the intermediate and deep seismicity occurring in the southern Tyrrhenian and in the Calabrian arc as a developed subduction of the Ionian oceanic lithosphere down to about 500 km in depth. The Aeolian Archipelago and the nearest seamounts are associated to the subduction process and the southern Tyrrhenian Sea interpreted as back-arc basin.

The heterogeneity of the source seismic mechanism occurring in the southern Tyrrhenian Sea in Sicily and in Calabria suggests the complex geodynamic contest.

However the study of this region raises several questions due to the lack of an exhaustive knowledge of the geologic structures caused by the insufficient resolution of the proposed geophysical models.

The tomographic techniques applied up to now have provided insights into the construction of large scale models of the Tyrrhenian region, though their lack of detail does not allow for discriminating the smaller structures within the larger ones. Often the reliability analyses of the recovered velocity field and the stability of the inverse problem (that are fundamental parameters for a geophysics studies) are not entirely addressed.

Only a detailed reconstruction of the geometric features of the actual subducting Ionian lithosphere may offer an important contribution to the cinematic models existing for the central Mediterranean. Furthermore, the detailed description of the structures responsible for the seismic activity in the Calabrian-Sicilian sector and for the surrounding basins may contribute to the seismic modelling in the space, time and magnitude domains.

In this thesis we presented a detailed study of the lithospheric and intra-mantellic structures of the southern Tyrrhenian region by performing a high resolution Local Earthquake Tomography (LET). The principal developments of the study consist of three key sections.

First, Chapters 1 and 2 briefly retraces the history of the seismic tomography and the proposed methodology over the last twenty years. The second chapter explicates the method used by the program *tomoDD* (Zangh and Thurber, 2003) which uses the double-difference method to solve the solution of the tomographic inverse problem, and which is the code adopted to perform the first tomographic images of this work.

Second, Chapters 3 and 4 develop methodological and theoretical aspects of a high resolution seismic tomography by creating a new post-processing technique that we called WAM (Weighted Average Model). The experimental data employed are form the earthquakes that occurred in the southern Italy between 1981-2005, and recorded by local and national networks of seismic stations. There are 1800 selected events, recorded by at least 10 stations and marked by RMS less than 0.50s after the relocation with a 1-D optimal model. This second part of the thesis focuses on the realization of the numerous tests carried out using both synthetic and experimental data. The tests allowed us to evaluate the dependency of the final model of a 'DD classic' tomography on the several input parameters. I performed the restoration-resolution test (Zhao *et al.*, 1992) as a synthetic test, to evaluate the ability of the selected data to recover the features of an experimental model previously obtained. The dependency of the final model on the initial parameters was assessed by performing three types of experimental tests; 1) assessment of the dependency of the final model on the inversion grid, by performing several inversions while rotating, translating and deforming the inversion grid; 2) assessment of the dependency of the final model on the initial one, by performing inversions with different 1-D and 3-D initial models; 3) assessment of the dependency of the final model on the selection of the experimental data and on the weights assigned to the absolute and differential times, by performing inversions while varying the amount of the absolute and differential data and the weighting scheme between absolute and differential times. All the

tests performed showed that using TomoDD the location of the anomalies is well constrained by the experimental data, however in some inversions their extension and mean velocity value are not sufficiently constrained in few but important portions of the *investigated volume*. This is due to the spatial heterogeneity of the hypocentral distribution, to the unsatisfactory azimuth coverage of the network (primary imputed to geographical factors) and especially to the impossibility of a complete optimization of the numerous parameters that affect the tomographic problem. The impossibility of exhaustively performing this optimization was the first motivation that pushed us to carry out a method that attempts to recover velocity models less dependent on the initial input parameters and thus more reliable. The average model was constructed by resampling the several velocity models obtained during the experimental tests into a fixed grid (called WAM grid), applying the same interpolation algorithm used to determine the continuous velocity model in TomoDD (in our case it is a trilinear interpolation algorithm). The DWS (Derivative Weight Sum, *Toomey and Foulger, 1989*), that is a parameter linked to the amount of the experimental data used to determine the velocity value in each node of the inversion grid, are interpolated in an identical grid. The DWS are used as a weighting factor to calculate the mean velocity into the nodes of the WAM grid. In this way more weight is given to the velocity values determined with more experimental information and then resolved with more reliability during the inversions. The weighted standard deviations and the weighted DWS distributions were determined with the same scheme. An *extended* version of the checkerboard test to evaluate the effectiveness and the validity of the WAM was performed by integrating the test with a parameter, the Restoration index (R), that permits a quantitative estimate (in %) of the reconstruction power of the checkerboard model. Furthermore, by comparing the R distributions and the standard deviations, we verified that an anticorrelation law exists between these parameters; in fact where there are high values of the standard deviation, low values of R were recovered in the part of the synthetic WAM and vice versa. With this analysis it was possible to link a quantitative parameter of the reconstruction capability (R) to the standard deviation that can be determined in the experimental WAM. In principle, the WAM method, being a post-processing technique, can be applied using any tomographic code, obtaining more reliability on the interpreted models.

In the third part of the thesis, Chapters 5 and 6, we applied the WAM method to the southern Italian region. The high reliability obtained and the high resolution of the WAM allowed us to reconstruct some geometric features of bodies within the Ionian slab and in the Tyrrhenian mantle. The major characteristic the Vp and Vs WAMs is the presence of some low velocity bodies ($7.0 < V_p < 7.7$ km/s and $3.8 < V_s < 4.2$ km/s) within the subducting Ionian lithosphere that is characterised by high velocity values ($8.2 < V_p < 8.8$ km/s and $4.75 < V_s < 5$ km/s). These low velocity bodies have variable horizontal dimensions between 15 -35 km and vertical ones between 35-55 km and have velocities compatible with serpentized zones (20-30% Vol, *Christensen, 2004*) of the Ionian lithosphere. The migration of the released fluids from the slab that serpentizes the harzburgite, is due to porous channels such as the ‘fault-bends’. The dip angle of the slab plays a fundamental role for the partitioning of the released fluids that migrate both in the mantle above and within the subducting lithosphere (*Abers, 2005*). At a depth greater than 230-250 km the pressure-temperature conditions allow the complete dehydration transforming the serpentines into high pressures phases, such as the phase-A that is highly similar to anhydrous lherzolite minerals in their seismic properties (*Fumagalli and Poli, 2005; Hacker et al., 2003*). With the WAMs I was able to reconstruct the 3-D shape of the Ionian slab that can be compared to an *hourglass* dipping 69° - 72° into N-W direction.

The low-Vp and Vs bodies imaged within the Tyrrhenian lithosphere down to 180 km of depth argue for the accumulation of significant amounts of partial mantle melting beneath the major active volcanoes (Stromboli, and less clearly Marsili). which feeds the present-

day volcanic activity. The low velocity regions are triggered by the released slab fluids. In addition, in the Vs WAM there are noticeable low velocity bodies located at a depth of 20-40 km beneath the Stromboli and the Marsili seamount basin that are interpreted as probable zones of accumulation of the magma migrating toward the surface.

Thanks to the merging of the petrological inferences and the 3-D detailed velocity models, we proposed a new mantle flow model for the studied region.

Finally, Chapter 7, presents some capabilities of the WAM method to carry out a large scale model while preserving its reliability and resolution.

ACKNOWLEDGMENTS

I would like to express my gratitude to a number of people for their help in a way or another throughout this work.

This work would never reached an end without the unconditional and continuous support of my love Daniela and of my parents, who were daily beside me, encouraging and thrusting this project.

Firstly, I thank Dario Luzio and Catherine Dorbath who offered me the possibility to investigate more deeply this subject. Working under their supervision was very interesting and stimulating.

I am grateful to Giuseppe D'Anna and to the INGV institute to the “real” support gave me, without which this work would not exist.

A particular thank go to the Prof. Silvio Rotolo, that pushed me toward new frontiers on the interdisciplinary aspects of my work.

Particular thanks are reserved to the components of the PhD jury: Prof. M. Fedi, Dr. S. Lallemand, Prof. F. Masson Prof. D. Schiavone, Prof A. Sulli, for their comments that pushed me to improve the manuscript and to produce interesting considerations.

I will never forget Jean Charlety, Rosaria Tondi and Alessia Maggi, who helped me sincerely while in Strasbourg.

Many thanks are reserved to Massimo Vitale for the friendship and consistent support, co-worker that everybody would like to have.

To those I missed to mention, I express as well my thanks and gratitude.

Contents

Abstract (in French)	v
Abstract (in Italian)	ix
Abstract (in English)	xiii
Acknowledgments	xvii
Contents	1
Introduction	
Area Under Study and Motivations	5
1. General principles of tomography	11
1.1 The Birth of Tomography	11
1.2 The Radon Transform	12
1.3 The Fourier Slice Theorem	14
1.4 Filtered Back Projection (FBP)	15
1.5 Medical Tomography	16
1.6 Seismic Tomography	17
1.6.1 <i>Travel-Time Tomography</i>	18
1.6.2 <i>Waveform Tomography</i>	19
1.6.3 <i>Diffraction Tomography</i>	20
1.6.4 <i>Surface-Wave Tomography</i>	21
1.7 Scale of Investigation	22
1.7.1 <i>Teleseismic Tomography</i>	23
1.7.2 <i>Regional Scale Tomography</i>	24
1.7.3 <i>Small Scale Tomography</i>	25
1.8 Local Earthquake Tomography	26
1.8.1 <i>Field Parameterization</i>	26
1.8.2 <i>Ray Path and Travel Time Calculation</i>	32
1.8.3 <i>Ray Illumination</i>	35
1.8.4 <i>Hypocenter-Velocity Structure Coupling</i>	36
1.8.5 <i>Inversion Methods</i>	37
1.8.6 <i>Quality Solutions</i>	39
2. Double Difference Tomography	41
2.1 The Double-Difference Method	41
2.2 The Double-Difference tomography	42
2.3 tomoDD Code	43
2.4 Construction of the Differential Data	45
3. Synthetic and Experimental Tests on the “DD” Tomography of the Southern Tyrrhenian Sea	47
3.1 Experimental Data	47
3.1.1 <i>Absolute Data and 1Dstarting Model</i>	48
3.1.2 <i>Differential Data</i>	49
3.2 Inversion Grid	50
3.3 Restoration Resolution Test	50
3.4 Dependency of the Velocity Model on the Inversion Grid	52
3.5 Dependency of the Velocity Model on the Initial Model	53
3.6 Dependency of the Velocity Model on the Experimental Data Selection Rules	56

3.6.1	<i>Dependency on the Absolute Data Selection</i>	56
3.6.2	<i>Dependency on the Differential Data Selection</i>	56
3.6.3	<i>Dependency on the Ratio of the Absolute/Differential Data</i>	57
3.7	Conclusions	59
4.	WAM Tomography and its Reliability: Application to the Southern Tyrrhenian Sea	61
4.1	Introduction	61
4.2	WAM Method	61
4.3	WAM Grid	62
4.4	Weighting Scheme	63
4.5	Reliability Test	64
4.6	Restoration Index	65
4.7	Comparison between “DD” Tomography Models and WAM	65
4.7.1	<i>Traditional Checkerboard Test with TomoDD</i>	65
4.7.2	<i>Dependency of the Velocity Model on the Hypocentral Incertitude</i>	67
4.7.3	<i>Dependency of the Velocity Model on the Picking Errors</i>	68
4.7.4	<i>Dependency of the Velocity Model on the Inversion Grid</i>	69
4.7.5	<i>WAM Test</i>	72
4.8	Effectiveness of the WAM Method	73
4.8.1	<i>Relationships between Restoration Index and Order of the WAM</i>	73
4.8.2	<i>Relationships between Restoration Index and Standard Deviation</i>	74
4.8.3	<i>Inferences on the WAM Grid an its Importance</i>	76
5.	WAM Models of the Southern Tyrrhenian Sea	79
5.1	Introduction	79
5.2	V _p WAM. Deep Structures	79
5.3	V _s WAM. Deep Structures	88
5.4	V _p /V _s WAM. Deep Structures	92
5.5	V _p and V _s WAM. “Shallow” Structures	94
5.6	Conclusions	97
6.	Petrological Inferences on the Ionian slab Structure and Geodynamical Modelling	99
6.1	Introduction	99
6.2	Petrological Constraints for Subducted Lithospheres	99
6.3	Discussion	103
6.3.1	<i>Inferences on the Ionian Slab</i>	103
6.3.2	<i>Comparison with other Tomographic Models</i>	109
6.3.3	<i>Inferences of the WAM Tomography on the Dynamics of the Mantle Flow</i>	110
7.	Prospective	114
	Appendix 1: LSQR	121
	References	124
	List of the Publications	135

Introduction

Area Under Study and Motivations

The Mediterranean Basin is the location of an interplate system where coexist both compressional and extensional regimes. It is the result of two major tectonic processes: the subduction of the African plate underneath the Eurasian plate and the progressive closure of the Mediterranean Sea involving a series of submarine-insular sills.

The Central part of the Mediterranean Basin exemplifies the juxtaposition of compressional and extensional tectonic activity. The region bordered by the Eastern Sicily up to the Calabrian Arc (including the Tyrrhenian and Ionian Seas) exhibits a particular set of features which my study will focus on.

The present-day tectonic setting of the Tyrrhenian-Apennine system is the result of the complex and slow convergence between Eurasian and African plates (0.5–1 cm/yr, De Mets et al., 1990), that has been active since at least 65 Ma (Dercourt et al., 1986; Dewey et al., 1989; Patacca et al., 1992). After the Alpine orogenesis (Eocene-Oligocene), the geodynamic evolution of the Tyrrhenian-Apennine system was driven by the eastward migration of the subduction hinge (Malinverno and Ryan, 1986). A factor that further increases the complexity of the central Mediterranean is that average Tertiary-Present rollback rates, and therefore subduction rates, increase from north to south (from less than 1 cm/year to more than 3 cm/year; Gueguen et al., 1998). The temporal evolution of the system is again under debate however, the most of scientific community is agreeing to subdivide the subduction-line migration into three main steps coincident with the probable main changes of rate subduction (Faccenna et al., 2001).

The Adriatic lithosphere, subducting westward beneath the European plate, underwent a gravitative roll-back. This generated both the shortening of the Adriatic accretionary wedge (Apennine Orogen) and the rifting in the back-arc region (Tyrrhenian Basin). During the late Oligocene–early Miocene (23–26 Ma) a phase of rifting began (figure 1.1.1a) that led to the opening of the Ligurian-Provencal basin as a result of the southeastward roll-back of an older northwest dipping subduction zone (e.g., Faccenna et al., 1996; Rosenbaum and Lister, 2004).

The opening of this basin was accompanied by a counter clockwise rotation of the Corsica-Sardinia (figure 1.1.1b) together with the former western margin of Adria (Apulia) and gave rise to the formation of the Apennines (Patacca and Scandone, 1989; Patacca et al., 1992). During this tectonic phase, the Apennine accretionary wedge underwent shortening. The roll-back of the subducting Ionian slab produced the opening of the southern Tyrrhenian Basin since Tortonian (10 Ma). At that time the lithospheric rifting separated the Calabria block from the Sardinia basement. This event led to the formation of new oceanic crust generating westward the Vavilov Basin (4.3–2.6 Ma, Sartori (1989); 8.5–4.5 Ma, Argnani, (2000)) and then south-eastward the Marsili Basin (1.6 Ma, Kastens et al. (1988); 2.0–1.7 Ma, Argnani (2000)). The highest rate of opening of the southern Tyrrhenian Basin was estimated up to 6 cm/yr by Faccenna et al. (2001). This evolution was accompanied by calcalkaline volcanism that migrated from west to southeast, from Sardinia (32–13 Ma) to the currently active Aeolian Island Arc (Marani and Trua, 2002).

The lithosphere and asthenosphere structure of the Tyrrhenian Basin have been analysed by several authors using different approaches, such as gravimetric methods (Morelli, 1970, 1997), seismic exploration (Finetti and Del Ben, 1986; Pascucci et al., 1999, Finetti, 2005 (figure 1.1.2a)), and dragging and volcanological studies (e.g., Kastens et al., 1988; Francalanci et al., 1993). Most of the published studies pointed out a slab beneath the Marsili Basin, the Ionian lithosphere subducting below the Calabrian Arc (e.g., Anderson and Jackson, 1987; Giardini and Velona', 1991; Selvaggi and Chiarabba, 1995).

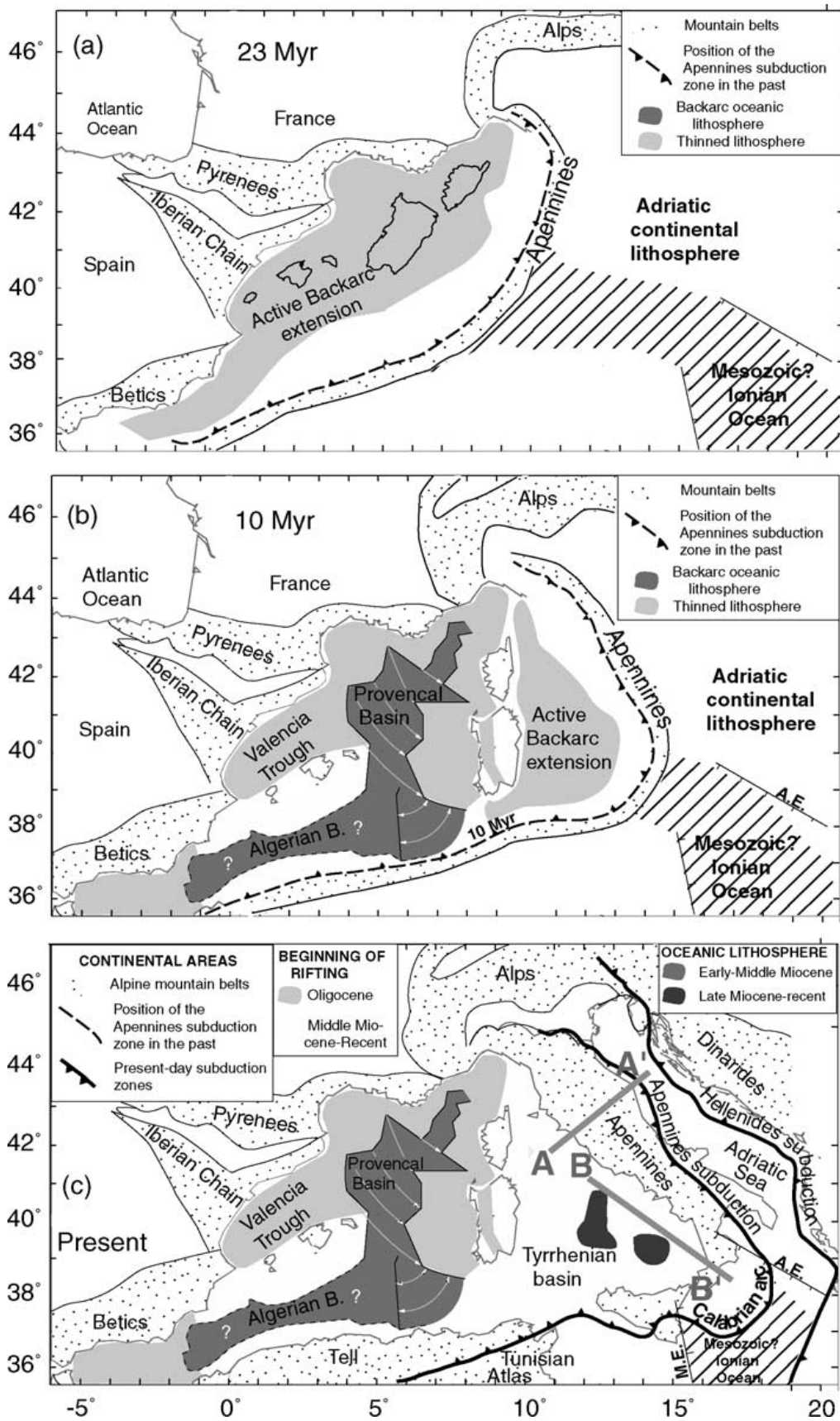


Fig. 1.1.1 – Probable geodynamic evolution of the southern Tyrrhenian Sea (from Carminati et al., 2005). In the last 23 Ma the evolution of the Mediterranean region is driven by an eastward migration of the subduction front allowing the opening of the Ligurian-Provencal basin (a), of the Vavilov one (b) and in the last of the Marsili basin (c).

The oceanic nature of the subducted lithosphere is derived by heat flow measurements (e.g., Della Vedova et al., 1984), calc-alkaline magmatism of the Aeolian Islands (e.g., Barberi et al., 1973), and crustal thickness and seismic reflection profiles in the Ionian Sea (e.g., De Voogd et al., 1992; Catalano et al., 2001 (figure 1.1.2b)).

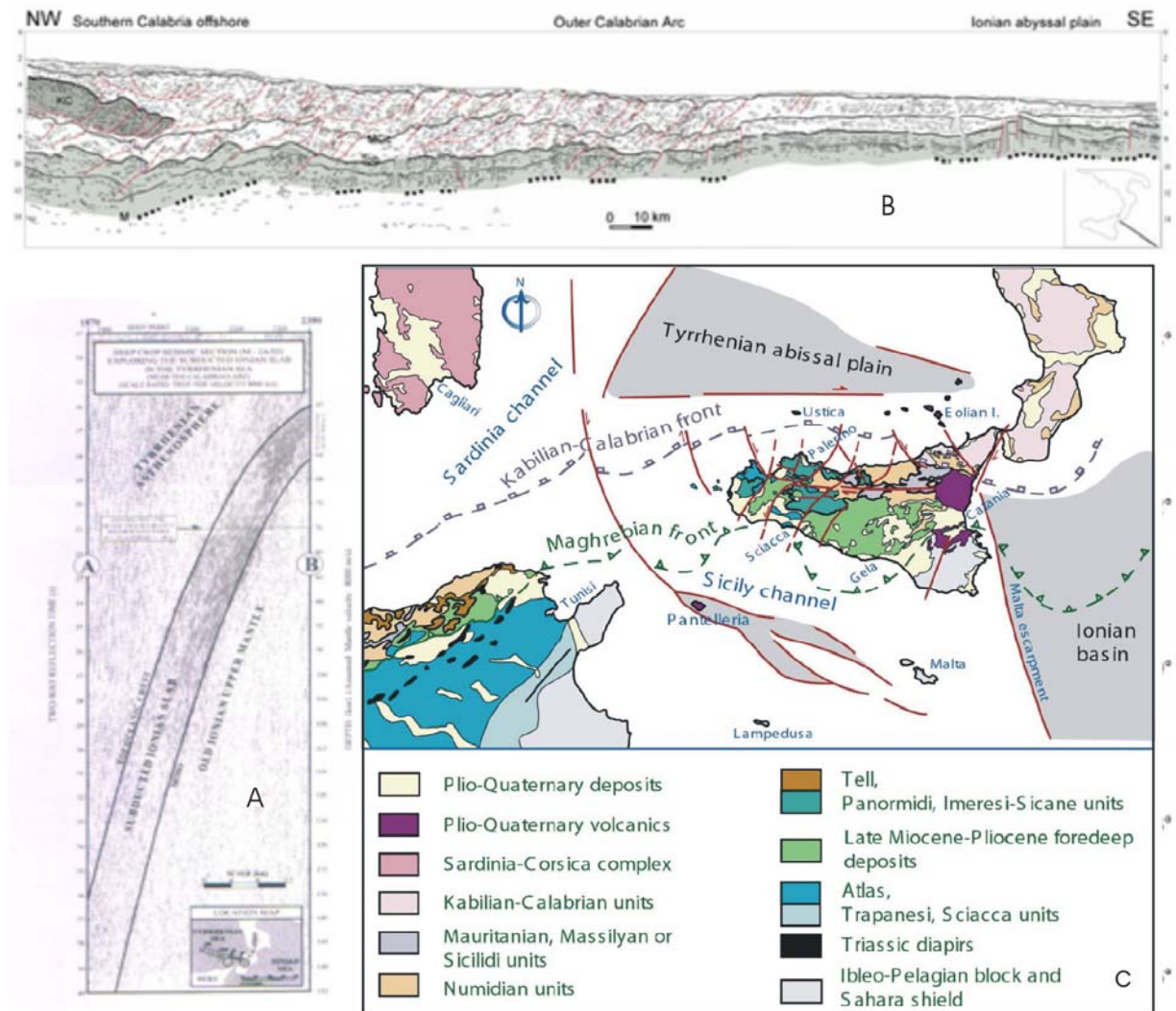


Fig. 1.1.2 – a) NVR section realized in the southern Tyrrhenian sea (from Finetti, 2005); b) NVR section realized in the Ionian Sea (from Catalano et al., 2001); c) Schematic tectonic map of the southern Tyrrhenian region.

The presence of this slab is supported by the occurrence of intermediate and deep earthquakes (fig. 1.1.3), which define a continuous, well-documented Wadati-Benioff zone from the surface to at least 500 km depth (e.g., Caputo et al., 1970, 1972; Anderson and Jackson, 1987; Giardini and Velonà, 1991; Selvaggi and Chiarabba, 1995, Cimini and Marchetti, 2006).

The Ionian lithosphere is estimated to be 125 km thick (Gvirtzman and Nur, 2001; Ponteviso and Panza, 2006, figure 1.1.4) and it is mainly composed of a 6-8 km thick Meso-Cenozoic sedimentary cover overlying an 8-9 km thick Mesozoic oceanic crust; the latter is a remnant of the former Tethyan realm (Catalano et al., 2001). The floor of the Tyrrhenian Basin is a much younger (6 - 2 Ma) oceanic crust as thin as 7-10 km in the Vavilov and Marsili sub-basins (Panza et al., 2007).

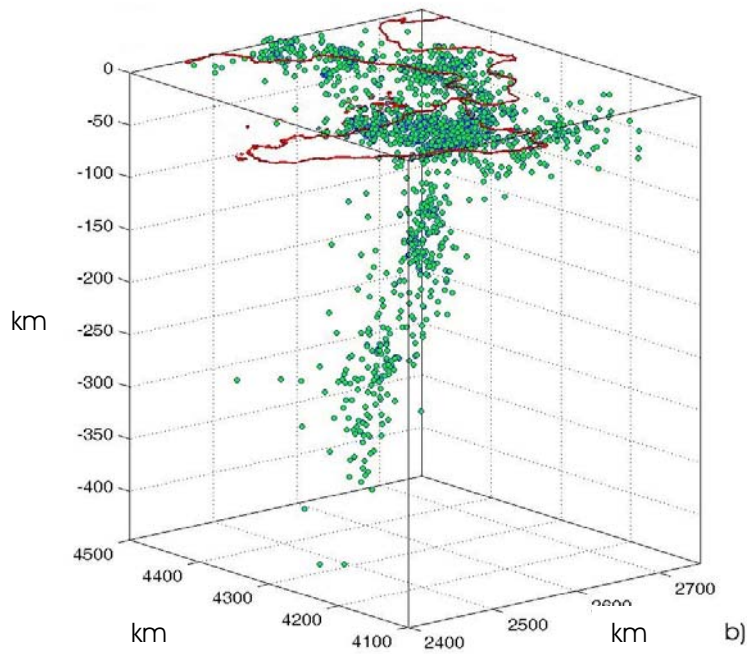


Fig. 1.1.3 – a) Hypocenters relative to deep earthquakes occurred in the southern Tyrrhenian sea. It is clearly visible the well-documented Wadati-Benioff zone.

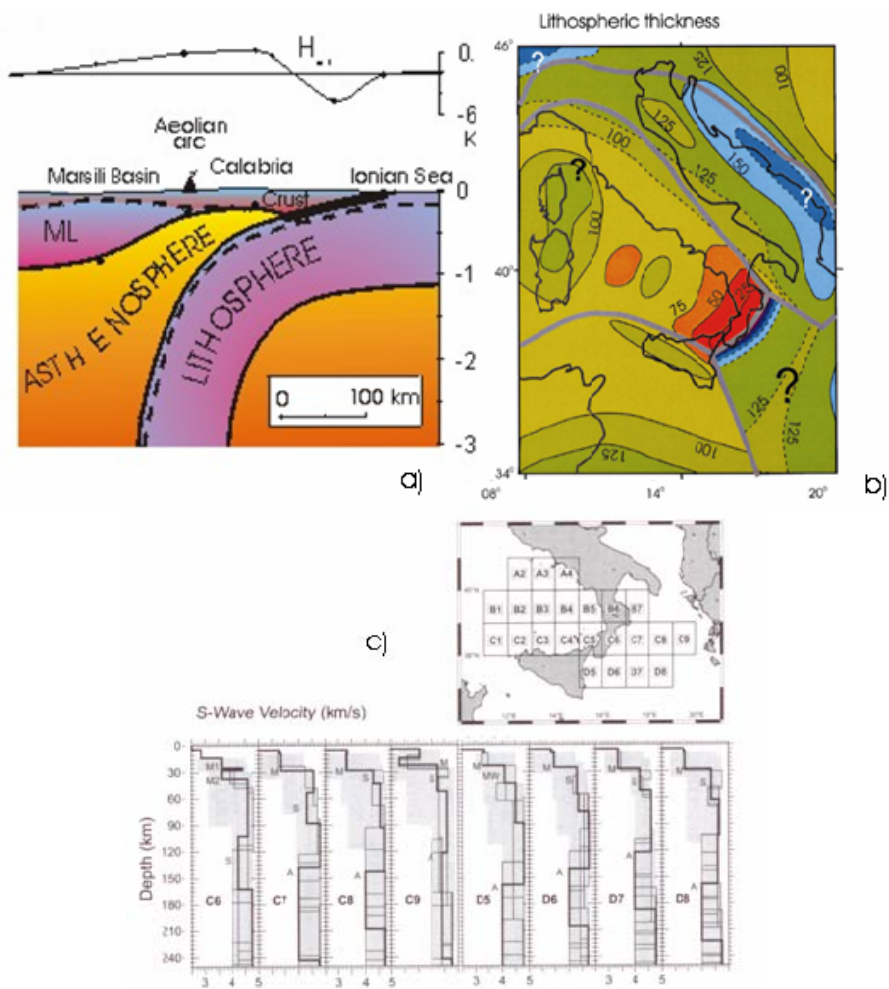


Fig. 1.1.4 – a and b) Probable thickness of the Ionian subducting lithosphere (Gvirtzman and Nur, 2001); c) 1D S-velocity models around the Ionian region (from Pontevivo and Panza, 2006).

In the last decades, many tomographic studies have been performed to define the seismic velocity field in the crust and upper mantle beneath the Tyrrhenian-Apennine system in order to provide constraints on the geodynamic evolution of the western Mediterranean Sea (e.g., Scarpa, 1982; Spakman, 1990; Amato et al., 1993a, 1993b; Cimini and Amato, 1993; Piromallo and Morelli, 1997; Lucente et al., 1999; Cimini, 1999; Di Stefano et al., 1999; Cimini and De Gori, 2001; Piromallo and Morelli, 2003; Spakman and Wortel, 2004; Montuori et al., 2007). All tomographic models, using teleseismic data (e.g., Amato et al., 1993b) or both regional and teleseismic events reported by International bulletins (e.g., Spakman et al., 1993) highlight a subvertical oceanic slab underneath Calabrian Arc dipping 70° – 75° NW down to 400 km depth (figure 1.1.5).

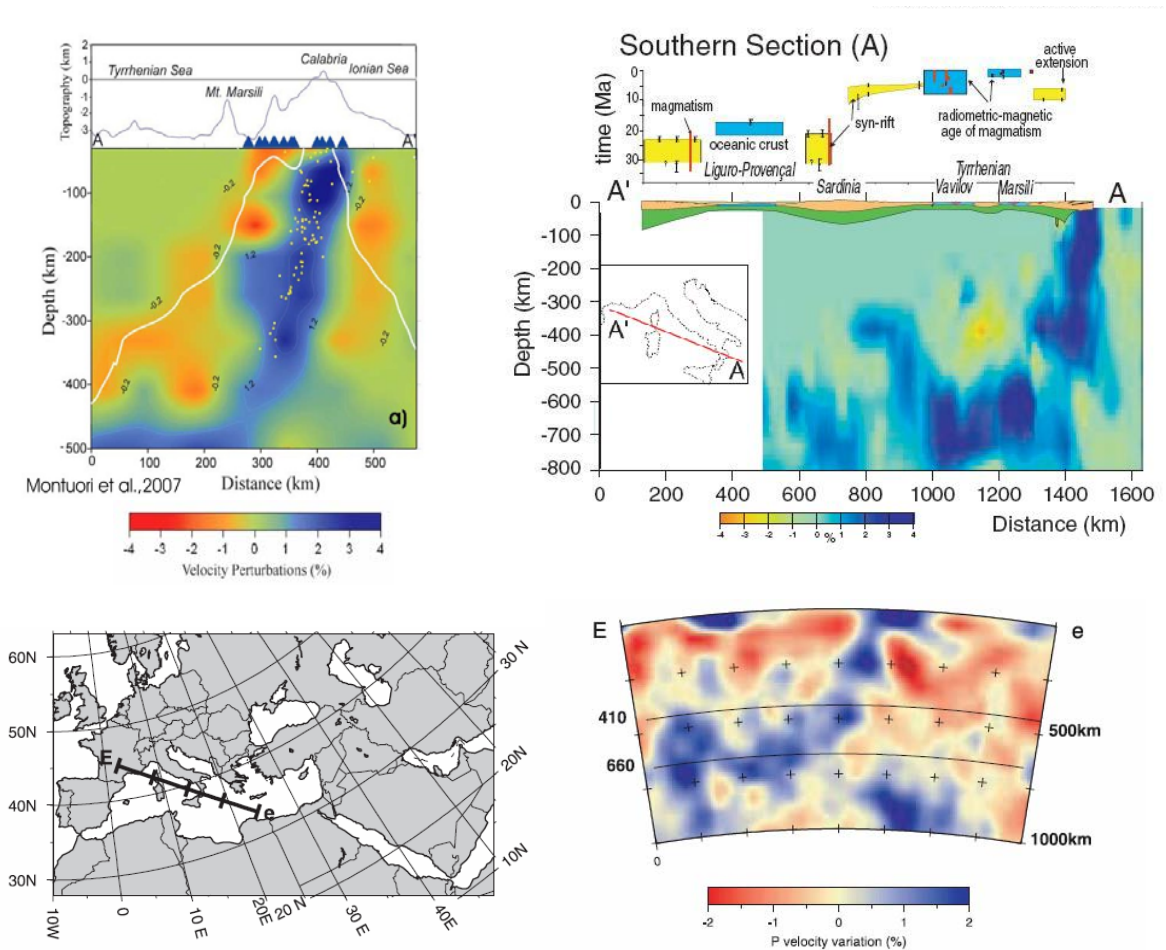


Fig. 1.1.5 – Some tomographies performed using teleseismic data showing the main features of the subducting Ionian Slab. Faccenna et al., 2001 (left), Piromallo and Morelli, 2003 (centre), Montuori et al., 2007 (right).

Below this depth, a sub-horizontal deflection of the slab is observed jointly with the north-westward shift of the deep seismicity. The subcrustal seismicity, located between 40 and 350 km depth, correlates well with the strong high-velocity anomaly imaged by the tomographies.

Nevertheless, the resolution of the existing tomographies have not allowed an investigation into heterogeneities within the subducting lithosphere, and the absolute values of the velocity field are not so reliable enough use them to make petrological inferences about the mineral phases existing at high pressure and temperature in this geodynamic context. The lack of resolution of the structures and the low reliability of the absolute velocity values are due essentially to the used technique (the teleseismic one) which

is, however, useful for global seismic modeling of the Earth with a resolution of about 100 km. The lack of these peculiarities strongly limits the use of the tomographies to constrain the geodynamical models and to understand the several processes linked to the plate-margins as the associate volcanism and the hinge zones.

The principal aim of this work is to obtain a high-resolution seismic tomography based on local earthquake data applying the *Weighted Average Model* method. In this thesis I will show, beside the classic approach used to realize a local earthquake tomography using the tomoDD program (Zhang and Thurber, 2003) in the southern Tyrrhenian Sea, the methodological guideline to realize and apply the WAM method. This method was completely implemented during the PhD study period as necessity to overcome some limits noticed during the taking in place of the DD tomography.

In fact, thanks to the reliability of the WAM, we interpreted the velocity model in the light of mineral phase equilibria governing the progressive dehydration of H₂O-Mg-bearing silicates in the ultramafic portion of the subducted lithosphere giving important insight about the distribution of the mineral phases within the Ionian slab and of the surrounding mantle.

Furthermore, the detail of the WAM allow an accurate identification of the shape of the Ionian slab and the geometry of some bodies around it, down to about 350 km, with a resolution never obtained before.

Finally, in the last chapter, I will show interesting prospective about the WAM method and its further application that will permit to unify several adjacent WAMs to construct a wide velocity model (more than regional scale) which always having an higher reliability and resolution than an conventional large scale tomography.

Chapters 1 and 2 are not available because under revision.

3. Synthetic and Experimental Tests on the “DD” Tomography of the Southern Tyrrhenian Sea

3.1 Experimental Data

In this work the experimental data employed are the arrival times of the first impulses P and S, relative to the events located in the window 14°30' E - 17°E and 37°N - 41°N and recorded during the period 1981-2005.

The seismicity of the southern Tyrrhenian region can be subdivided into 2 subsets (figure 3.1.1). The first one contains the shallow seismicity (less than 40 km) produced by the brittle behaviour of the upper portion of the thinned southern Tyrrhenian lithosphere. This is a part of the hinge zone between the African and European plates. This set is elongated in an E-W direction and it runs in latitude from the Sicilian coastline to the Aeolian islands. The second set contains the deep seismicity (down to 500-600 km of depth) mostly located in the eastern part of the southern Tyrrhenian sea between the Aeolian archipelago and the Calabrian coastline. The hypocentres of this set are located in a well developed Wadati-Benioff zone having average dip of 69°-72° and NW polarity, as a result of the subduction of the Ionian lithosphere beneath the Calabrian arc and Tyrrhenian sea.

In this work we used both shallow and deep events to realize a local earthquake tomography in the Southern Tyrrhenian sea using the TomoDD code and then the WAM method.

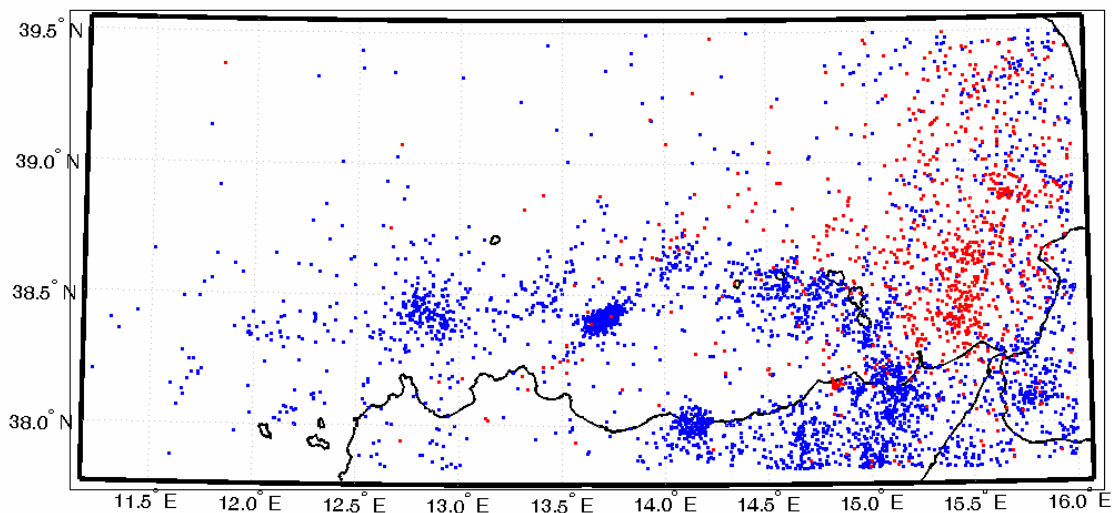


Fig. 3.1.1 – a) Map of the seismicity of the southern Tyrrhenian region. The blue points mark the shallow earthquakes (less than 40 km) while the red squares the deep events.

The data set used mainly contains P and S arrival-times taken from the INGV¹'s Italian seismicity catalogue (CSI² and others). We integrated the INGV data set with arrival times, picked out on wave-forms recorded from some temporary arrays. The 1-D model that uses

¹ Italian National Institute of Geophysics and Volcanology

² Seismic Italian Catalogue

the INGV to locate the Italian events is a simple model with only 3 layers. The mean RMS for the events located in this region is estimated on 0.45 s. The absence of a 1-D optimal model for the Tyrrhenian region and the integration of the arrival times induced us to perform a preliminary re-location of the about 4000 recorded events and the optimization of the 1-D model.

3.1.1 ABSOLUTE DATA AND 1-D STARTING MODEL

The preliminary hypocentral re-location and the optimisation of the initial 1-D V_p and V_s models have been performed by a procedure designed to optimize the hypocentral coordinates, the velocity models and the station residuals by minimizing both the L_2 norm of the residuals travel times and their coherence in the offset domain (Giunta et al., 2004). This technique is derived from the observation that the cinematic forward problem solved for a set of events an unsuitable velocity model produces biases on the travel times which show large coherence intervals in the offset domain.

This procedure, initially implemented for HYPOPC71 code (Lee and Lahr, 1985), was adapted to HYPOINVERSE-2000 code (Klein, 2002) to produce an initial 1-D model with constant vertical gradients within the layers, as required by the TomoDD code. The model obtained (that we called MC) represents the initial vertical velocity distribution for the tomographic inversions and for the synthetic and experimental tests (figure 3.1.1). The mean probable error on the epicentral coordinates of the about 4000 re-located events is ~ 2.5 km, whereas on the hypocentral depths it is ~ 4.5 km.

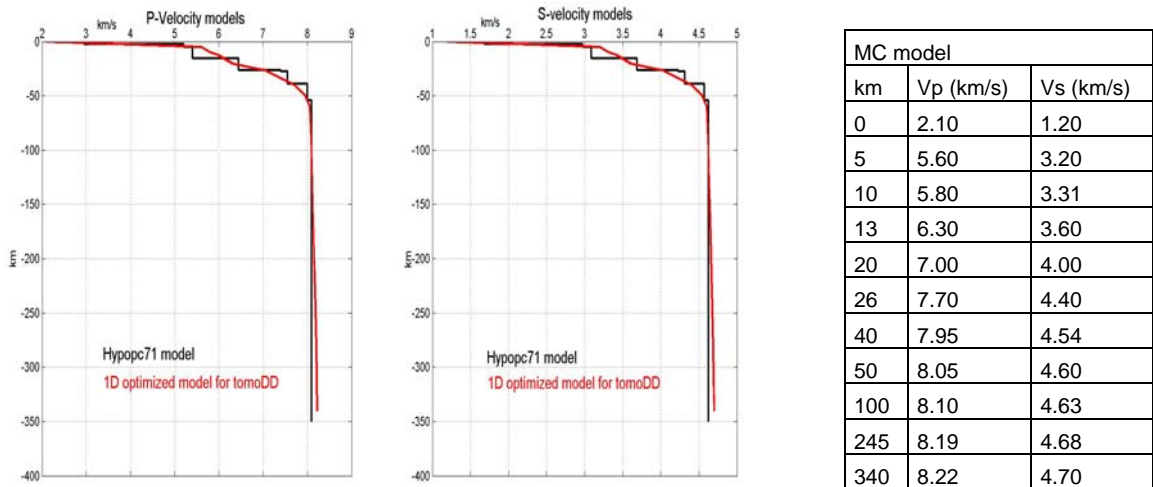


Fig. 3.1.1 – Velocities and depth of the MC model obtained with HYPOPC71 (black) and HYPOINVERSE-2000 (red).

The events selected from this optimized data set to perform the tomography are recorded by at least 10 stations and marked by RMS (weighted mean square residual) less than 0.50 s after the relocation. The resulting data set refers to 1800 earthquakes (figure 3.1.2a) recorded by on average 16 stations, for a total of 28873 P- and 9990 S- arrival times and relocated with mean RMS = 0.30 s. The total number of stations which recorded the 1800 events was 183 and are mostly located inside the target area.

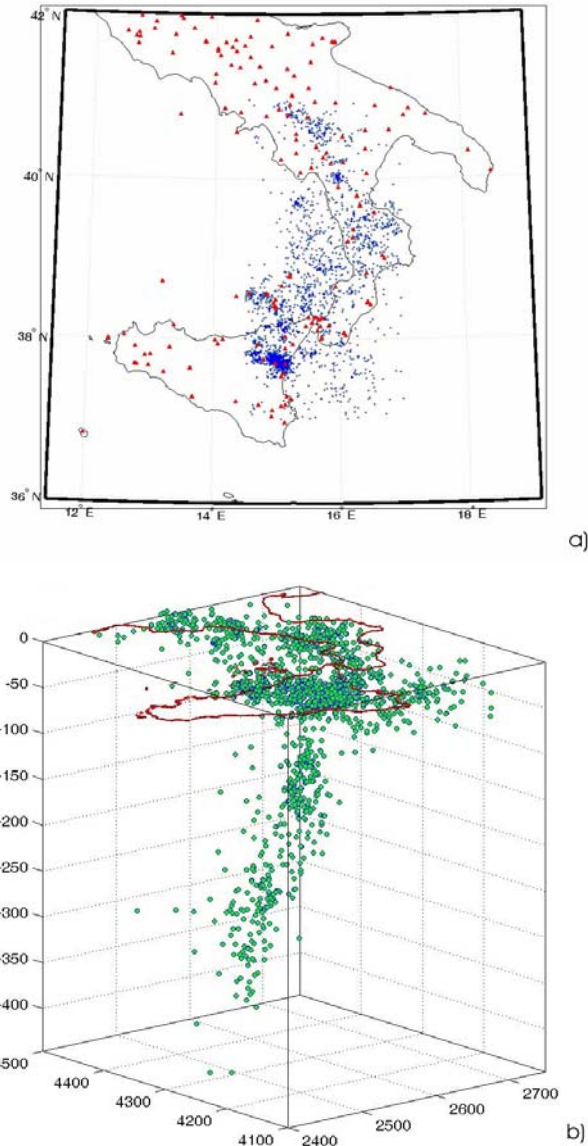


Fig. 3.2.1 – a) Map of the selected epicentres and stations. b) 3-D view of the hypocentres showing the down-dip distribution beneath the southern Tyrrhenian sea.

The subcrustal events in this database, located between a depth of 40 and 360 km, are 419. Their hypocentres are concentrated within the subducting Ionian lithosphere (figure 3.2.1b).

3.1.2 DIFFERENTIAL DATA

We performed several differential data selections to evaluate how much this data set affects the inversion results and if it really improves the reliability of the velocity models. Tests on the importance of the differential data selection will be discussed in section 3.6.3.

In particular, we used several thresholds of some parameters discussed in 2.4 to extract many differential data sets. The least numerous one, obtained fixing the maximum inter-event distance to 10 km, contains 55467 P- and 23992 S- differential times, while the largest, obtained with a threshold of 20 km, encloses 79985 P- and 28370 S- differential times.

3.2 Inversion Grid

We parameterized the V_p and V_s models assigning velocity values to the nodes of a rectilinear 3-D inversion grid. The continuous velocity field is determined inside each cell using a tri-linear interpolation algorithm (Thurber, 1993). We carried out several inversions using numerous grids with different node positions using both experimental data and synthetic data to perform subsequent tests. The total number of the nodes of each inversion grid is 3276 excluding the marginal nodes. The average lengths of the horizontal grid edges, excluding the boundary nodes, were 310 km and 190 km (figure 3.2.2) whereas the vertical one was 340 km. The average spacing along each direction was 17 km, 38 km and 13 km, respectively. The figure 3.2.1 shows the node positions of the reference inversion grid used for most of the synthetic and experimental tests. This grid has origin of the Cartesian system centred at $38^{\circ}.667$ N and $15^{\circ}.5$ E and the points are at $X = -150, -130, -115, -100, -85, -70, -55, -40, -25, -5, 20, 35, 60, 80, 100, 120, 140, 160$ km, at $Y = -220, -100, -40, 10, 50, 9, 200$ km, and at $Z = 0, 5, 10, 13, 20, 26, 40, 50, 60, 70, 80, 90, 100, 115, 130, 150, 165, 180, 195, 215, 230, 245, 265, 280, 310, 340$ km.

We essentially preferred the anisotropic spacing of the grid along the two horizontal directions with inter-distance ratio between the nodes ~ 0.5 because previous studies suggested that there is a dominant strike of the deep structures approximately perpendicular to the maximum node density direction. Other authors used similar grids to investigate quasi-2-D structures having strike known *a priori* (Zhang and Thurber, 2003; Shelly et al., 2006).

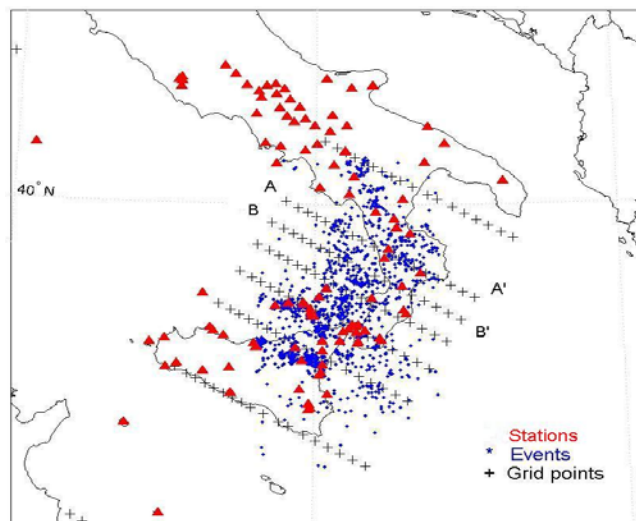


Fig. 3.2.2 – Map of the selected epicentres and stations, and inversion grid used for most of the synthetic and experimental tests. The profiles A-A' and B-B' regard the sections discussed in the synthetic and experimental tests.

3.3 Restoration Resolution Test

To perform the synthetic tests we used the real distribution of the stations and the hypocenters located with the MC model. We calculated the travel-times with the 3-D model (figure 3.3.1) resulting from an experimental data inversion (MCS). In these test (both synthetic and experimental ones) we will assess the reliability only for the velocity model of the P-waves. In the sections A-A' and B-B' of the MCS V_p model a low velocity body is clearly visible, in the right part of the pictures located approximately beneath the Calabrian arc region. These characteristic bodies are inside the well constrained part of the model (marked by the red line delimiting areas having $DWS > 50$, value often used by

other authors to delimit the well constrained part of the model, e.g. Shelly et al., 2006) but confined in its border area. In this work we called the part of the model characterised by DWS values greater than 50 the *investigated volume*. Synthetic tests could help to assess the reliability of the geometries obtained, or reveal some distortions as smearing effects. Furthermore, just beside the low V_p bodies high values of velocity are visible down to 100 km of depth in the section A-A' and down to 300 km in B-B'. High velocities of the seismic P-waves are typical in the subducting slabs and we will see in the Chapter 6 that the 3-D shape of the Ionian slab justifies this peculiar geometry.

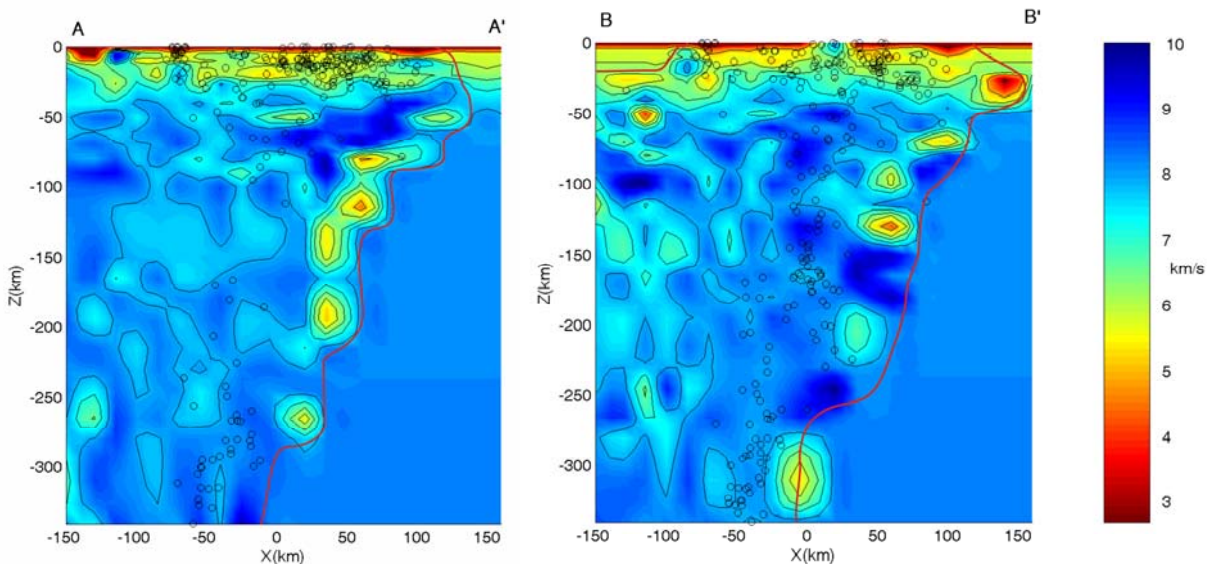
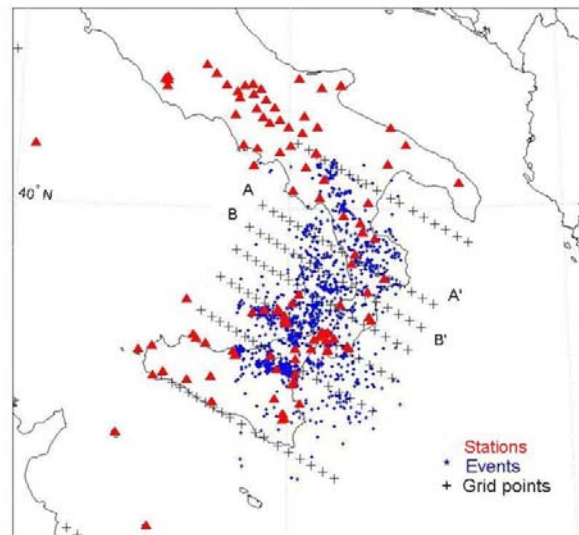


Fig. 3.3.1 – Map of the selected epicentres and stations, and inversion grid used for the and experimental test. The profiles A-A' and B-B' regard the sections of the MCS velocity model. The red lines limit the portion of the poorly resolved model ($DWS < 50$).

Starting from the MC model and using the synthetic data without adding any noise, the result of the test showed that the information contained in the calculated travel times was able to reconstruct velocity distributions closely matching the MCS model in the volumes where the DWS is greater than 50 (figure 3.3.2 left) and that only in section B-B' a low V_p

zone is noticeable not recovered in the MCS. However, this body is outside of the well constrained area and it does not affect the features of the model that we will interpret. We performed the restoration-resolution test (Zhao et al, 1992), consisting in the inversion of the synthetic data perturbed with a random noise having standard deviation equal to the L_2 norm of the residuals of the experimental data inversion that in our work is estimated of 0.62 s.

The result of this test (figure 3.3.2 right) highlights the stability of the inverse problem and the ability of the selected data to recover the information contained in a 3-D model with strong lateral heterogeneities.

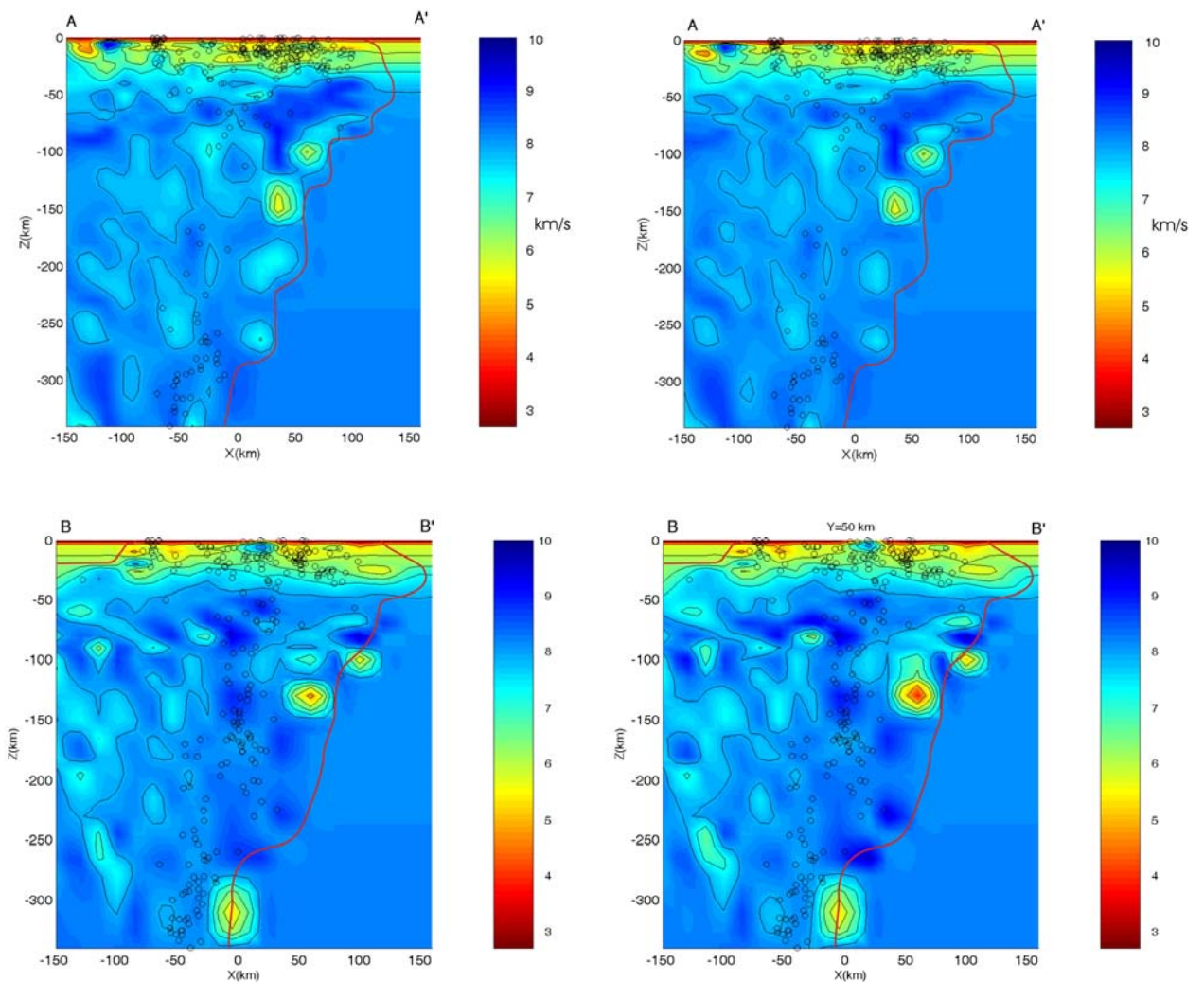


Fig. 3.3.2 – Synthetic test with exact data (left). Restoration Resolution test (right). The red lines limit the portion of the poorly resolved model ($DWS < 50$).

3.4 Dependency of the Velocity Model on the Inversion Grid

To evaluate the dependence of the final velocity model on the nodes position of the inversion grid, we carried out several experimental tests, by rotating, translating and deforming the reference inversion grid.

An example of these tests is imaged in figure 3.4.1 that shows the horizontal slices at a depth of 100 km of two velocity models carried out using two different inversion grids.

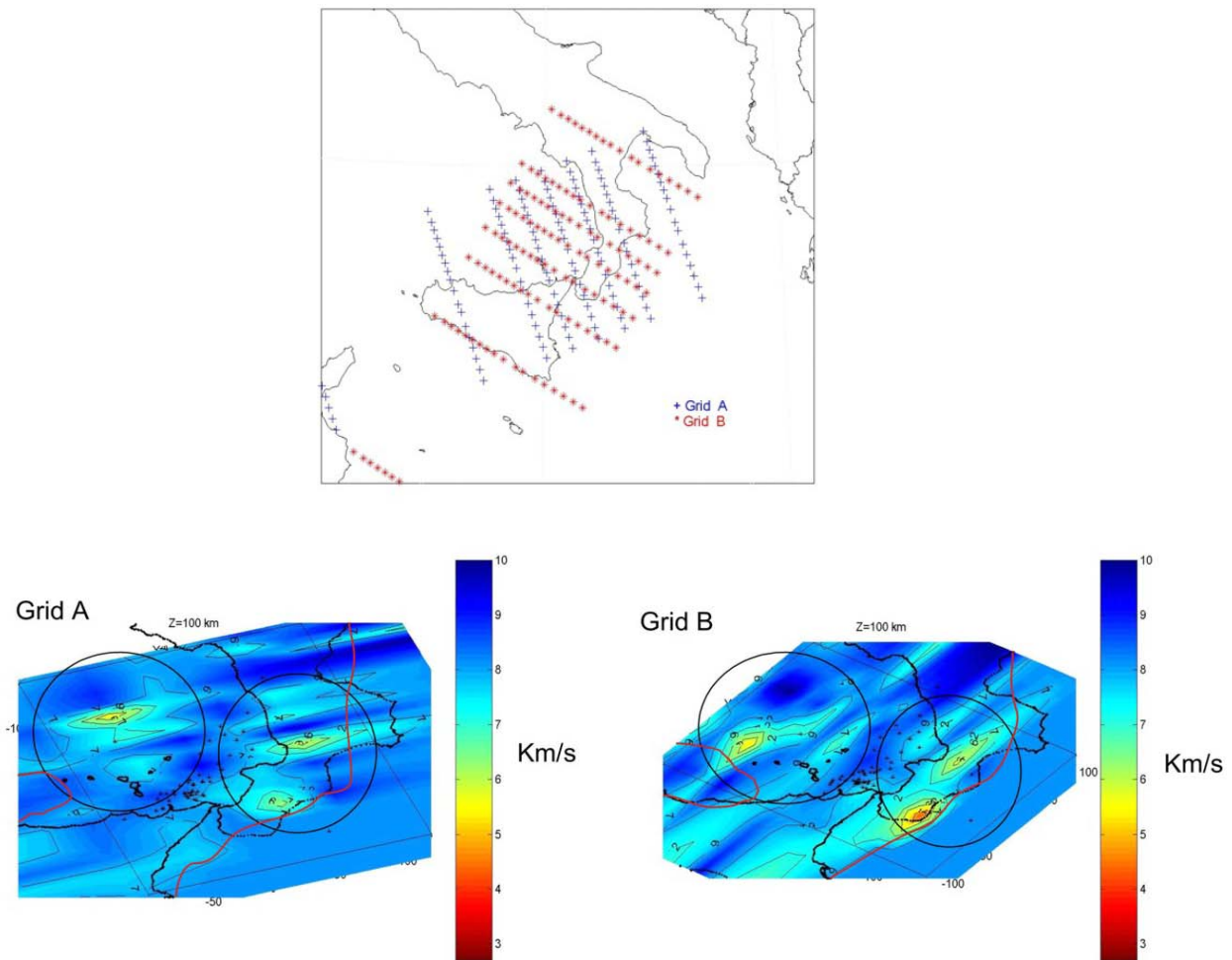


Fig. 3.4.1 – Models regarding grids A and B used for the experimental tests. The two horizontal sections (centre and right) show the plane at a depth of 100 km. Compare the similarity of the velocity patterns within the circled areas. The red lines limit the portion of the poorly resolved model ($DWS < 50$).

Both the inversions show low velocity bodies below the Calabrian arc and the southern Tyrrhenian sea north of the Aeolian archipelago. The part of the models between the Calabrian-Sicilian coastline and the Aeolian islands is characterized by high values of seismic velocity. It is worth noting that the ‘stretching’ of the velocity models due to the anisotropic inversion grids used is clearly visible. Nevertheless, the main features of the velocity distributions are clearly congruent.

The relative standard deviation of the velocity estimates obtained in 15 inversions is $\sim 1\%$ in the volumes around the earthquake hypocentres, but increase up to $\sim 7\%$ in the border of the investigated volumes (characterized by $DWS > 50$). This variability does not change the features of the velocity anomalies having linear dimensions greater than 15-25 km.

3.5 Dependency of the Velocity Model on the Initial Model

In this paragraph we show the models obtained in some tests, carried out to evaluate the influence of the initial model on the final velocity distribution. The experimental data inversions were performed using different starting 1-D and 3-D models. The 3-D models are characterized by the presence of slow and/or fast bodies that simulate the investigable portion of the down-going slab (figure 3.5.2 and 3.5.3).

In the first test we used an initial model close to MCS (figure 3.5.2 first column) while in the second one a model characterised by high velocity in the volumes where MCS depicts low velocities (figure 3.5.2 second column). Subsequently, we tested an initial model with an intermediate 3-D velocity distribution (figure 3.5.3 first column). In all these tests the experimental data produced 3-D models comparable to the MCS model.

A 1-D model with velocities 1 km/s higher than the MC below a depth of 40 km (figure 3.5.3 second column) led to a velocity distribution similar to that of MCS showing the low influence of the 1-D initial condition on the final velocity model.

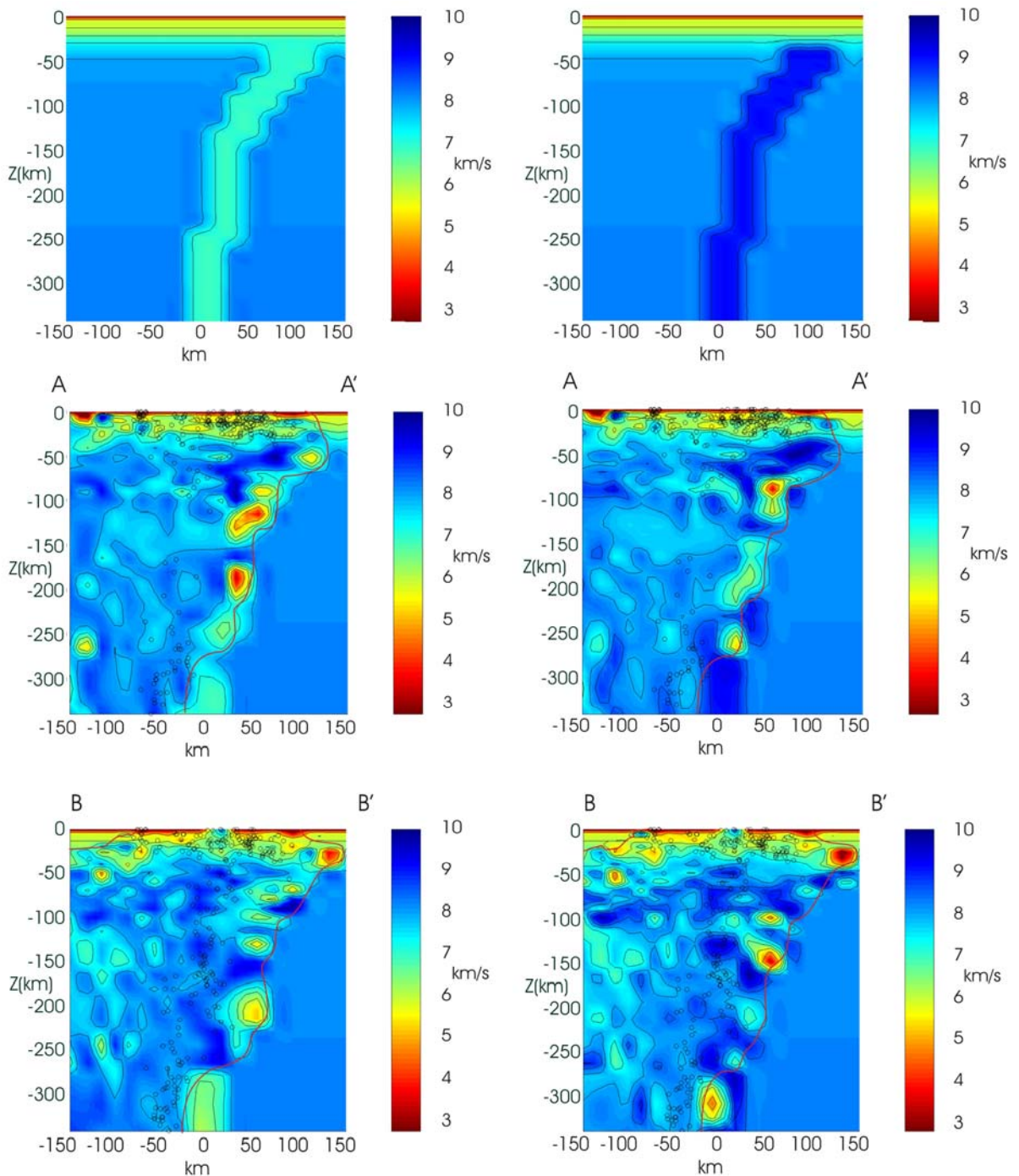


Fig. 3.5.2 – Dependency of the tomographic results on the initial models. In the first row 3-D initial models are displayed. Below the initial model it is possible to see the vertical sections obtained along the profiles A-A' and B-B'. The red lines limit the portion of the poorly resolved model ($DWS < 50$).

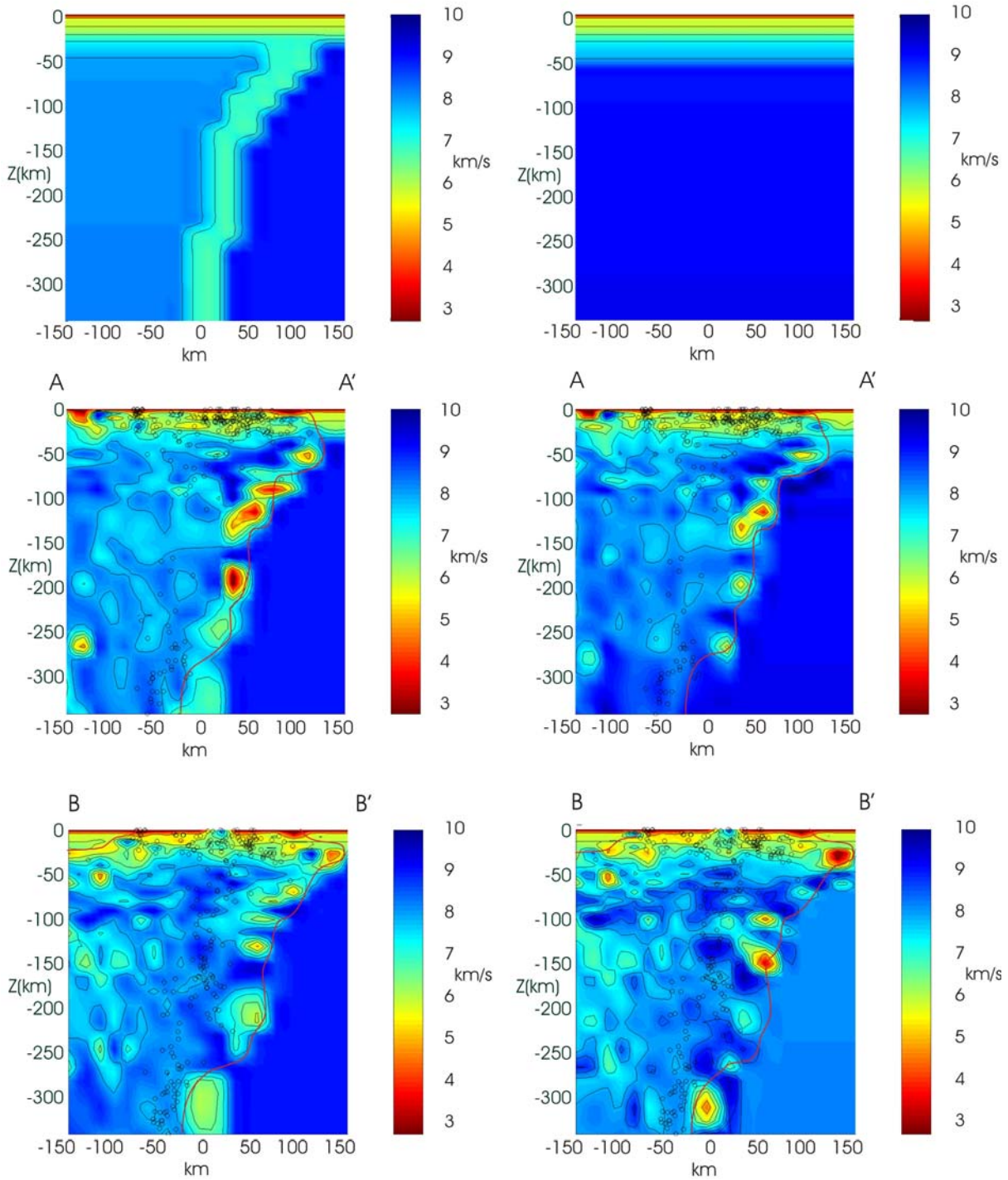


Fig. 3.5.3 – Dependency of the tomographic results on the initial models. In the first row 3-D and 1-D initial models are displayed. Below the initial model it is possible to see the vertical sections obtained along the profiles A-A' and B-B'. The red lines limit the portion of the poorly resolved model ($DWS < 50$).

In conclusion, these tests showed that with the selected data set the inverse problem is practically independent of the initial model and always reconstructs the features of the MCS model, even if we observed some biases on the absolute velocity values, especially in the border areas where are depicted important features of the V_p model.

3.6 Dependency of the Velocity Model on the Experimental Data Selection Rules

3.6.1 DEPENDENCY ON THE ABSOLUTE DATA SELECTION

To assess the dependence of the tomographic model on the data selection procedure we inverted the following data sets: a) the first one includes the events that occurred between 1988 and 2002, having RMS less than 0.5s and at least 10 P-arrival times per event; the total number of selected events was 1492; b) the second one covers the 1981-2005 period, uses the same thresholds of RMS and number of registration per event, for a total of 1800 events selected; c) the last data set contains the events recorded in the 1981-2005 period having at least 10 registrations per event and RMS less than 0.7s; the total number of selected events was 2434. The differential data for all the sets have been determined with the same construction scheme.

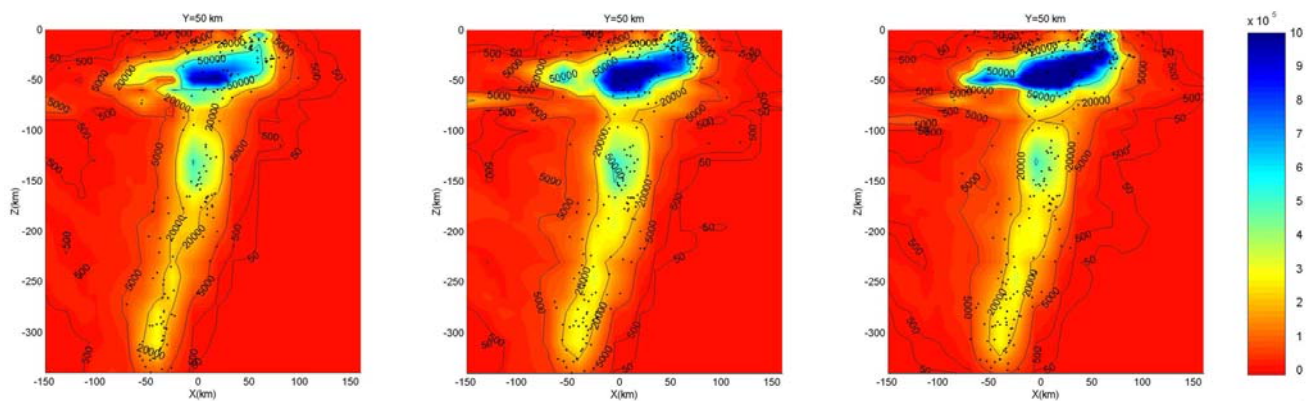


Figure. 3.6.1 – DWS distributions relative to the three data sets containing 1428 (left), 1800 (centre) and 2463 (right) events, respectively.

The inversions gave coherent results, however the largest data set, even if it includes data with larger errors, seems to have produced more reliable models, increasing consistently the *DWS* in many nodes that were poorly constrained by the smaller data set (figure 3.6.1) without dramatically altering the velocity distribution.

3.6.2 DEPENDENCY ON THE DIFFERENTIAL DATA SELECTION

Different differential data sets have been obtained by varying the parameters as the maximum distance between event pair and station, the maximum hypocentral separation between the events of a pair (inter-event distance), the maximum number of neighbors per event and the minimum number of links required to define a neighbour.

Several inversions have been performed for the three absolute data sets assessing the influence of the individuation rules of event pairs on the final velocity model and hypocentral location.

The table 3.6.3.1 illustrates how the size of the differential data set strongly depends on the setting of the input parameters. In this case we highlighted the importance of the maximum inter-event distance threshold during the dataset construction.

Number of events	maxsep (km)	abs. P	abs. S	dt P	dt S	mean RMS of the hypocentres
1428	6km	22742	8389	23992	7492	0.125
1428	10km	22742	8389	40063	13021	0.129
1428	20km	22742	8389	78352	26086	0.133
1428	50km	22742	8389	100924	32225	0.138
1800	10km	28873	9990	55467	15239	0.116
1800	15km	28873	9990	72995	22983	0.115
1800	20km	28873	9990	79985	28370	0.119
2463	6km	37159	13802	54409	18092	0.146
2463	10km	37159	13802	61926	20255	0.131
2463	15km	37159	13802	84777	27992	0.139

Table. 3.6.2.1 – Table showing the dependence of the size of the differential data set as function of the inter-event threshold. In the last colon are reported the mean RMS of the events re-located with the absolute and differential data displayed in the table and with the same weighting scheme for all the inversions.

The low spreading of the RMS reported in the table shows that the hypocentral location (and the velocity inversion) are stable with respect to the change of the differential data set. Waldhauser suggests to fix the threshold MAXSEP taking into account the hypocentral incertitude location and starting values of 10 km is considered as reasonable. In our case to fix 10 km as the inter-event distance threshold (two times the incertitude of the hypocentral depth) seems to be the best solution for the largest absolute datasets while for the smallest one seems to be 6 km.

3.6.3 DEPENDENCY ON THE RATIO OF THE ABSOLUTE DATA/DIFFERENTIAL DATA

Subsequently, we tested how much the weighting scheme of TomoDD, between absolute and differential data, could affect the final results.

The authors of the program (Zhang and Thurber) suggest that a good strategy for the iterative procedure is to alternate joint inversions (velocity model and hypocentral location) to simple re-locations. Besides to alternate joint/simple inversions, the authors suggest giving high weight to absolute data in the first steps and to subsequently increase the differential data weights gradually to add more details to the velocity structures determined during the first steps. They affirmed that this strategy gives the smallest location and velocity errors.

The table 3.6.3.1 reports 10 inversion schemes relative to different weighting strategies. In the tests 1, 2 and 3 we generally gave high weight to the differential data in the first steps while in the 4, 5 and 6 tests we used an opposite strategy. In the last 4 tests, we tested the strategy suggested by Thurber and others with mixed weights.

1	NITER	WTCTP	WTCTS	WRCT	WDCT	WTCD	DAMP	JOINT
	2	1	1	-9	-9	0.1	140	1
	1	1	1	-9	-9	0.1	95	0
	3	1	1	6	6	1	120	1
	1	1	1	6	-9	1	100	0
	3	1	1	6	6	10	110	1
	1	1	1	6	6	10	100	0
2	NITER	WTCTP	WTCTS	WRCT	WDCT	WTCD	DAMP	JOINT
	1	10	10	-9	-9	0.1	120	1
	2	1	1	-9	-9	0.1	110	1

	3	1	1	6	6	1	170	1
	1	1	1	6	-9	1	120	0
	3	0.1	0.1	6	6	10	160	1
	1	0.1	0.1	6	6	10	100	0
3	NITER	WTCTP	WTCTS	WRCT	WDCT	WTCD	DAMP	JOINT
	2	0.1	0.1	-9	-9	1	120	1
	1	0.1	0.1	-9	-9	1	100	0
	2	1	1	-9	-9	1	150	1
	2	1	1	6	-9	0.5	120	1
	2	1	1	6	6	0.1	120	1
	1	1	1	6	6	0.1	100	0
4	NITER	WTCTP	WTCTS	WRCT	WDCT	WTCD	DAMP	JOINT
	3	0.1	0.1	-9	-9	10	160	1
	1	0.1	0.1	-9	-9	10	120	0
	1	10	10	-9	-9	1	105	0
	3	10	10	6	-9	0.1	130	1
	3	0.1	0.1	6	6	10	120	1
	1	10	10	8	6	0.1	130	1
5	NITER	WTCTP	WTCTS	WRCT	WDCT	WTCD	DAMP	JOINT
	2	0.1	0.1	-9	-9	10	160	1
	1	1	1	-9	-9	10	90	0
	3	1	1	-9	-9	1	135	1
	1	1	1	6	-9	1	100	0
	3	10	10	6	6	0.1	120	1
	1	10	10	8	6	0.1	95	0
6	NITER	WTCTP	WTCTS	WRCT	WDCT	WTCD	DAMP	JOINT
	2	1	1	-9	-9	10	130	1
	1	1	1	-9	-9	10	95	0
	3	1	1	-9	6	1	80	1
	2	10	10	10	10	1	150	1
	2	10	10	6	6	0.1	130	1
	1	10	10	6	6	0.1	90	0
7	NITER	WTCTP	WTCTS	WRCT	WDCT	WTCD	DAMP	JOINT
	3	10	10	-9	-9	0.1	130	1
	2	10	10	-9	-9	0.1	120	0
	3	1	1	-9	-9	1	130	1
	2	1	1	10	10	1	120	1
	3	0.1	0.1	8	8	1	130	1
	2	0.1	0.1	8	8	1	120	0
8	NITER	WTCTP	WTCTS	WRCT	WDCT	WTCD	DAMP	JOINT
	1	10	10	-9	-9	1	110	0
	2	1	1	-9	-9	10	180	1
	2	1	1	-9	-9	1	110	1
	2	10	10	6	-9	0.1	160	1
	1	10	10	6	6	0.5	140	1
	1	10	10	8	6	0.1	100	0
9	NITER	WTCTP	WTCTS	WRCT	WDCT	WTCD	DAMP	JOINT
	3	1	1	-9	-9	1	170	1
	1	10	10	-9	-9	0.1	120	1
	1	0.1	0.1	-9	6	10	80	1
	3	1	1	10	10	1	170	1
	3	0.1	0.1	6	6	10	130	1
	1	0.8	0.8	6	6	1	80	0

10	NITER	WTCTP	WTCTS	WRCT	WDCT	WTCD	DAMP	JOINT
	1	1	1	-9	-9	0.1	120	1
	1	1	1	6	10	0.1	80	0
	2	1	1	6	6	1	170	1
	2	1	1	6	-9	0.1	110	1
	2	1	1	6	6	10	180	1
	1	0.1	0.1	6	6	10	60	0

Table. 3.6.3.1 – Data weighting and re-weighting strategies. NITER is the number of iterations for each cycle; WTCTP and WTCTS are the weights of catalog P, S data; WRCT is the residual threshold in sec for catalog data; WDCT is the max dist [km] between catalog linked pairs; WTCD is the relative weighting between abs and diff data; JOINT: =1, simultaneous inversion: =0, event relocation only DAMP is the damping for lsqr method. A value of -9 means that the weighting of that type is not used on that iteration, corresponding to a very large value of event separation in km or large misfit in seconds.

The best weighting strategy tested is the N 6 as well suggested by the mean RMS reported in the table 3.6.3.2. This weighting scheme does not alternates between ‘strictly’ joint and simple inversions but agrees the progressively increment of the weights of the differential data.

Strategy	RMS	St.Dev
1	0.1301	0.063
2	0.1266	0.0511
3	0.1269	0.0607
4	0.1217	0.058
5	0.1219	0.0579
6	0.1189	0.0581
7	0.1384	0.069
8	0.1254	0.0533
9	0.1222	0.058
10	0.1255	0.0587

Table. 3.6.3.2 – Mean RMS and standard deviation relative to the ten weighting strategies.

It is worth noting that the results synthesised in table 3.6.3.2 always show good weighting schemes in term of RMS and of velocity models obtained. The low RMS variability confirms the capability of the experimental data to constrain, not only the velocity model, but also the hypocentral model.

3.7 Conclusions

The spatial distribution of the differences between arbitrary pairs of models obtained in the experimental tests always shows, in addition to a low spatially incoherent component, low systematic misfits which have never skewed the main velocity anomalies.

All the tests performed showed that using TomoDD the location of the anomalies is well constrained by the experimental data, however in some inversions their extension and mean velocity value are not sufficiently constrained in few but important portions of the *investigated volume*. This is due to the spatial heterogeneity of the hypocentral distribution, to the unsatisfactory azimuth coverage of the network (primary imputed to geographical factors) and especially to the impossibility of a complete optimization of the numerous parameters that affect the tomographic problem. The impossibility of exhaustively performing this optimization was the first motivation that pushed us to carry out a method that attempts to recover velocity models less dependent on the initial input parameters and thus more reliable.

4. WAM Method and its Reliability: Application on the Southern Tyrrhenian Sea

4.1 Introduction

To reduce the spread of the set of the *possible* models, obtained with TomoDD, we constructed average models. These models show a lower mutual variability compared to those relatives to the ‘classic’ tomographies because they are less dependent on the subjective choice of the parameters that affect the inversion process.

In this section we describe the construction method of the Weighted Average Model (WAM) and we give an assessment of its reliability and of its resolving power.

The WAM method is a post-processing technique that could be used with any tomographic inversion code; it probes the space of the *possible* models to synthesize a new model and not to find the best model or to define a probability density of the class of the models.

4.2 WAM Method

The WAM method consists of 6 steps which are used to firstly achieve the experimental velocity model and then to realize an *integrated* synthetic test showing the reliability of the WAM.

These steps are:

- 1) Sampling of the space of the compatible models with the data by performing several inversions with different set of input parameters (figure 4.2.1).
- 2) Re-sampling of each velocity model into the nodes of a fixed grid (WAM grid). Each node will contain a vector of velocity values with dimension equal to the number of inversions carried out.
- 3) Interpolation of the *DWS* grid of each inversion in an identical WAM grid. Each node will contain a vector of *DWS* values with dimension equal to the number of inversions carried out.
- 4) Building of the velocity WAM by assigning to the nodes of the WAM grid a weighted mean of the velocities obtained from each inversion.
- 5) Computation of the velocity weighted standard deviation into the nodes of the WAM grid.
- 6) Estimation of the reliability of the velocity anomalies on the basis of the local values of the standard deviation and of the restoration index determined during the *integrated* synthetic test.

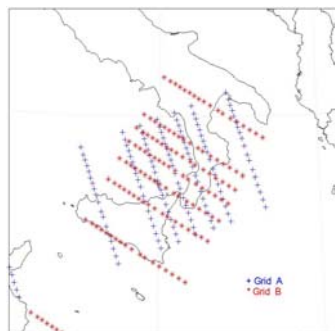


Fig. 4.2.1 – Example of a random sampling of the space of the models compatible with the dataset. In this figure are imaged two of the several inversion grids used to realize the “classic” DD tomographies.

The main advantage of the WAM method is that several models, obtained by using different input parameters (initial model, inversion grid, data selection etc.), can be synthesized in an average model giving a quasi statistical independence on the choice of the input parameters and this peculiarity guarantees a more reliability of the WAM than any 'single' model produced with a 'classic' tomography.

4.3 WAM Grid

The WAM grid is the fixed grid used to construct the WAM. Each velocity model, excluding the external cells, carried out by an i -th inversion with TomoDD, is re-sampled into the WAM grid with the same trilinear algorithm used to determine the continuous velocity field in each cell of the inversion grid (figure 4.3.1).

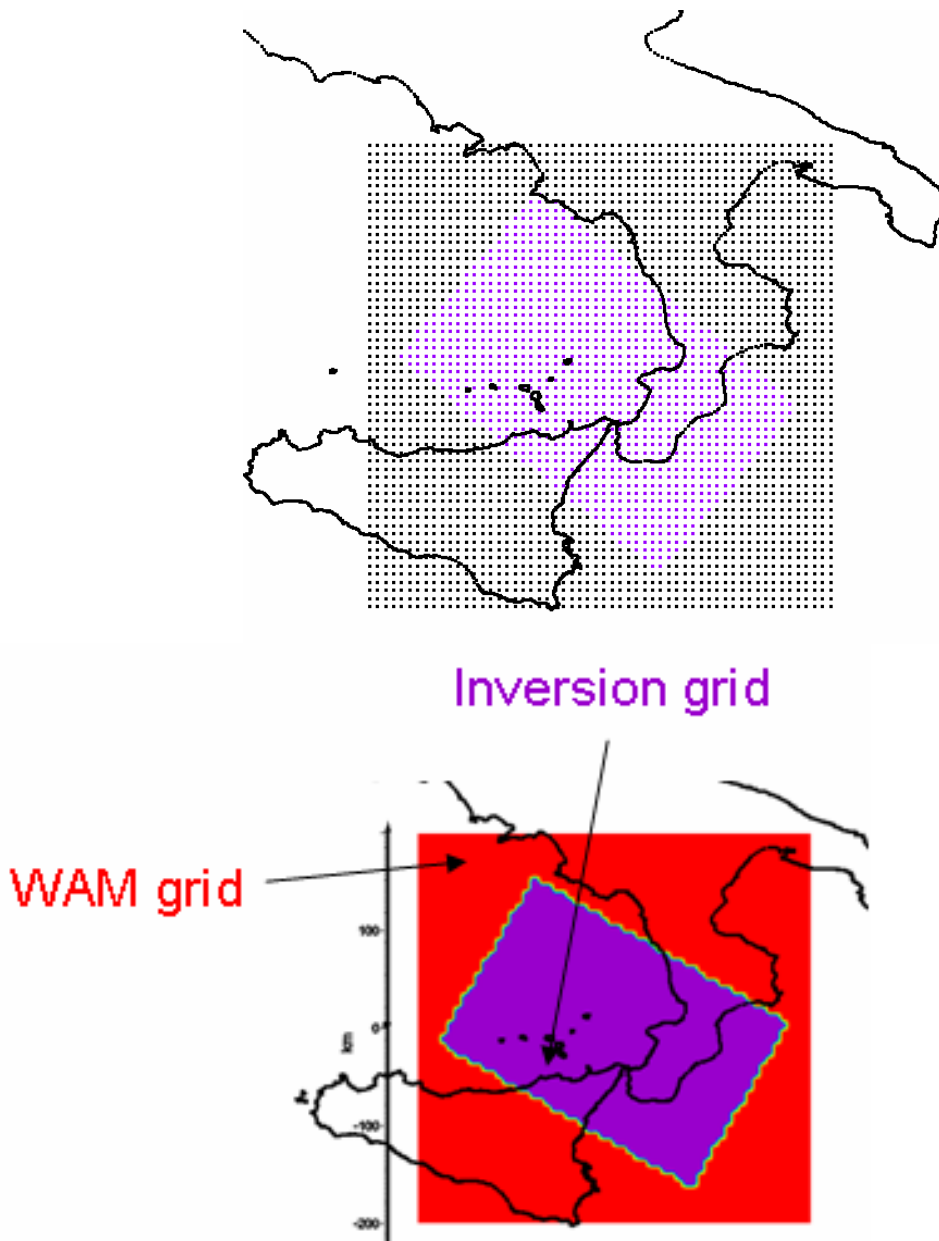


Fig. 4.3.1 – Map showing the density of the nodes of the WAM grid (top) and example of an inversion grid re-sampled on the WAM grid (bottom).

It is worth noting that in this way the velocity model is exactly ‘transported’ exactly into the WAM grid even though the spacing between the nodes of the WAM grid is smaller than the mean spacing of the nodes of the inversion grids used.

We verified the statement that the transport of models to the WAM grid does not produce biases by performing an inverse transport of a model to the starting inversion grid. In this work the WAM grid has a dimension of 400x400x350 km³, is centred at 38°40’N-15°30’E, and has horizontal spacing of 7 km and vertical spacing of 6 km. The total number of the nodes is 198476.

In paragraph 4.7.3 we tested the absence of a bias caused by using cells of the WAM grid finer than the mean size of the cells of the inversion grid.

An analogue WAM grid is constructed to describe the *DWS* spatial distributions relative to the inversions. The *DWS* values are determined using the same algorithm of trilinear interpolation used for the velocity models.

4.4 Weighting Scheme

We determined the velocity values of the final WAM as weighted mean of the velocities relative to the numerous inversions previously performed. In this study we used the *DWS* as the weight factor because it is directly linked to the experimental information used to determine the velocity during the *i*-th inversion.

The equations used to determine the weights for the velocity values are:

$$\text{If: } DWS_i = 0 \Rightarrow w_i = 0$$

$$\text{If: } DWS_i \leq LIM \Rightarrow w_i = \frac{LIM}{50}$$

$$\text{If: } DWS_i > LIM \Rightarrow w_i = \frac{\overline{DWS}_i}{\overline{DWS}_{i_{max}} - LIM} (DWS_i - LIM) + LIM$$

where $DWS_{i_{max}}$ and \overline{DWS}_i are the maximum and averaged *DWS* values in the *i*-th inversion respectively, *LIM* a threshold of *DWS* defined to pick out the nodes where the velocity estimates have been considered reliable and the constant 50 was empirically optimized. The *DWS* was set to zero in the nodes where it was not possible to assign a velocity estimate. The *LIM* value was fixed at a *DWS* threshold equal to 100, as often adopted in literature to delimit well resolved areas (Zhang et al., 2004).

The isosurface $DWS = LIM$ will enclose the *investigated volume* of the final tomographic model. We used the same weights both to calculate the mean velocity and to determine the weighted standard deviations of the velocities in each node.

The $DWS(i,j,k)$ in the (i,j,k) -node of the WAM grid was determined with the following relationship:

$$DWS(i, j, k) = \frac{\sum_{i=1}^n w_i DWS_i(i, j, k)}{\sum_{i=1}^n w_i}$$

Where w_i are the weights previously defined.

It is obvious that this simple weighting scheme is able to give more weight to the velocity values that have been determined in the *best reliability conditions*, because they are constrained by a more experimental information, and thus may better contribute to estimating the mean velocity into the nodes of the WAM grid.

4.5 Reliability Test

We implemented an *extended* version of a checkerboard test, that should always be performed before an experimental WAM *tomography*, to assess the effectiveness of the WAM method compared to a ‘classic’ tomography.

In this study we calculated the synthetic arrival times of P waves for a checkerboard model (figure 4.5.1) using the station and hypocentre distributions of the experimental data set. Each patch is $28 \times 28 \times 24 \text{ km}^3$ large (4 inter-distance nodes of the WAM grid along each direction) and has velocity +6 % and -6% alternatively with respect to the MC model. Between two patches a transition zone is present with a constant gradient superimposed on that of MC. The size of the patches is consistent with the mean resolution power that we expected from the tests performed on the single DD inversions (see cap. 3).

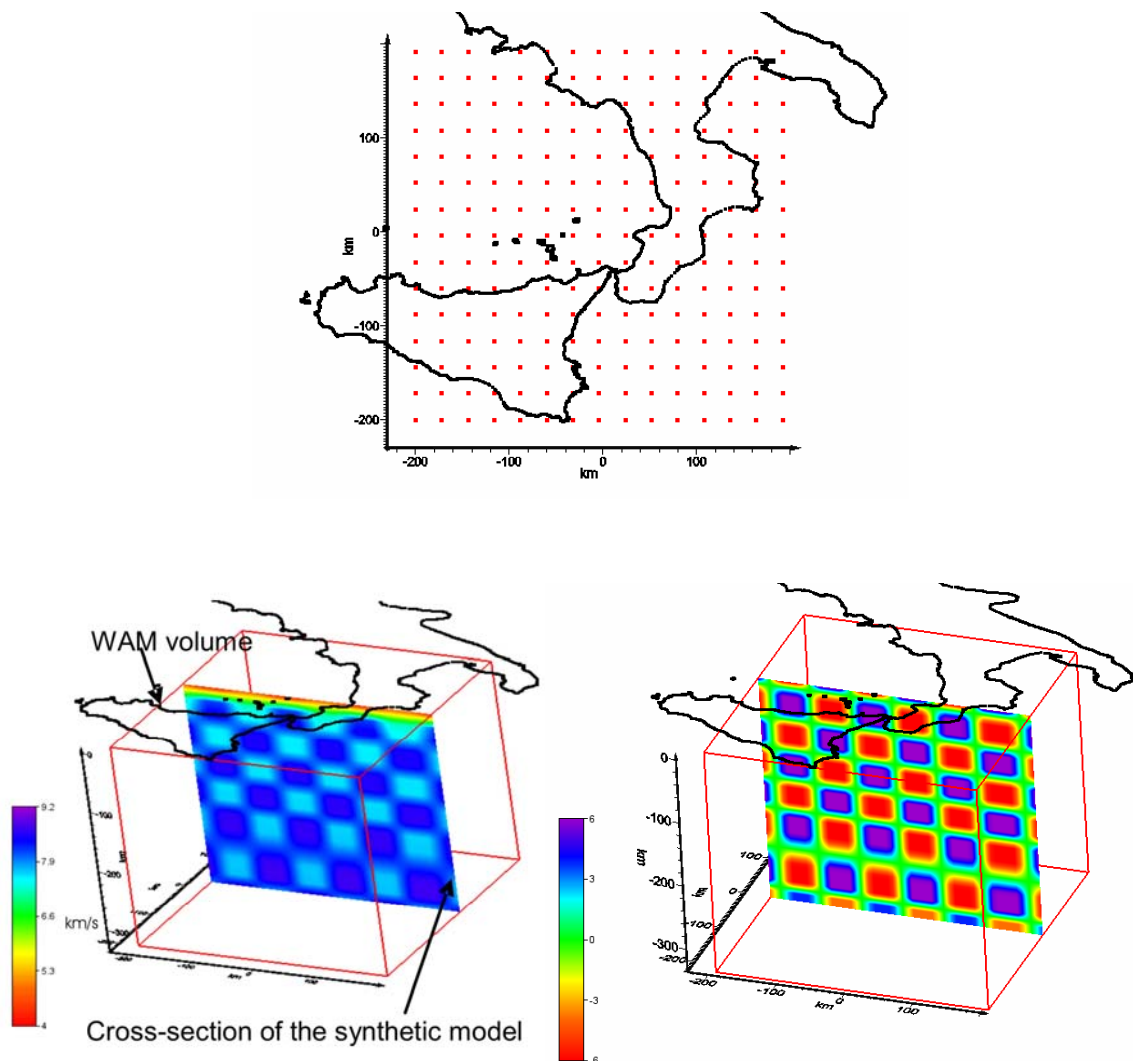


Fig. 4.5.1 – Grid points (top), checkerboard V_p model (left) and corresponding V_p percent anomalies (right) used to calculate the synthetic travel-times. To calculate the travel times was used the real positions of the events and of the stations.

Afterwards, we perturbed the synthetic travel-times with increments normally distributed with null mean and standard deviation 0.6 s.

To construct the synthetic WAM we performed about 60 inversions changing the input parameters but only a subset has been used to construct it. In fact we chose only the inversions that sampled the model space producing significant differences between arbitrary pairs of the models.

4.6 Restoration Index

The tool *restoration index* (R) was introduced to quantify the mean recovery of the synthetic model and it is defined as:

$$R(i, j, k) = 100 \left(1 - \frac{|x_t(i, j, k) - x_v(i, j, k)|}{|x_i(i, j, k) - x_v(i, j, k)|} \right)$$

where:

$x_t(i, j, k)$ is the velocity value in the node (i, j, k) after a single inversion

$x_v(i, j, k)$ is the velocity value in the node (i, j, k) in the 3-D true model

$x_i(i, j, k)$ is the velocity value in the node (i, j, k) in the 1-D initial model.

We have the complete restoration of the velocity in a node when R is 100, if R = 0, the node was not inverted, while, when R < 0 the velocity estimate differs from the true value more than initial velocity.

In most tomographic studies the recovered velocity models are only displayed without any indication about the errors on the velocity estimates. With R it is possible to quantify, not only the ability to reconstruct the shape of the patches but also the degree of re-approach to the true velocity on the whole *investigated volume*.

4.7 Comparison between 'DD' Tomography Models and WAM

In this paragraph we will discuss the results of the *extended* checkerboard test applied to a Vp "DD" classic tomography and to the Vp WAM. Bear to mind that the *investigated volume* is the part of the grid with DWS greater than 100 in the inversion.

The checkerboard test is able to give insight into the reconstruction power of the data using a synthetic model. Often the scientific community does not consider some aspects about the meaning of the results or does not fully carry out the test. Now we will show all the aspects that are sometimes not completely discussed in the scientific papers.

4.7.1 TRADITIONAL CHECKERBOARD TEST WITH TOMODD

The first step of an analysis of reconstruction capability using the checkerboard test starts with the study of the results obtained inverting; 1) the exact synthetic P travel times; 2) the exact hypocentre locations and; 3) a perfect parameterization of the model, i.e. by using as inversion grid the same which was used to calculate the synthetic travel-times.

The results show how the patches of the model are well reconstructed for the most part for the *investigated volume*, and that the R distribution indicates, quantitatively, the recovery power of the method and of the data (figure. 4.7).

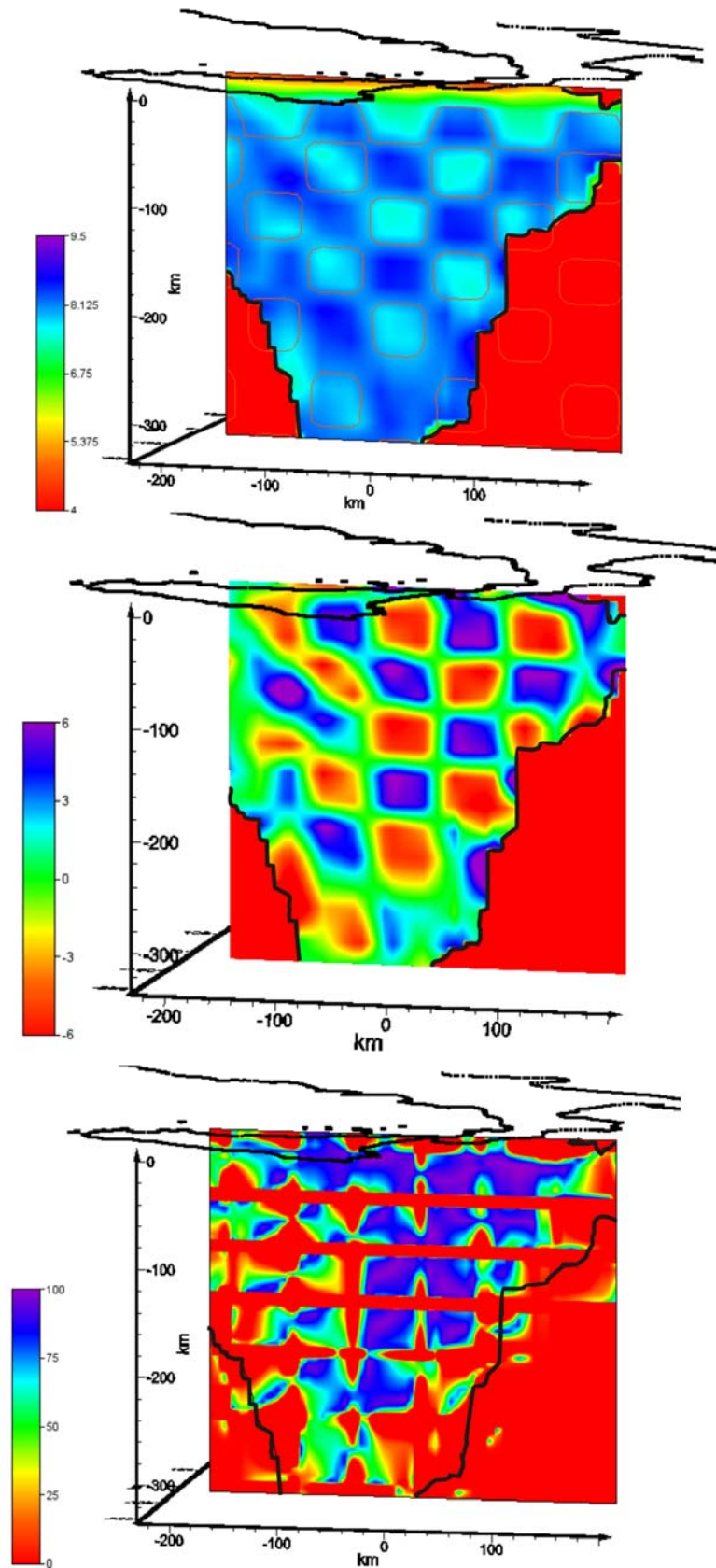


Fig. 4.7.1 – Section of the reconstructed checkerboard V_p model using the exact synthetic travel times (top). On centre it is displayed the same section of the V_p model expressed in percent and bottom the corresponding restoration index distribution. The black lines limit the area of the investigated volume ($DWS > 100$). The patches on the velocity model contour velocity isovalues of the true model represented in the fig. 4.5.1.

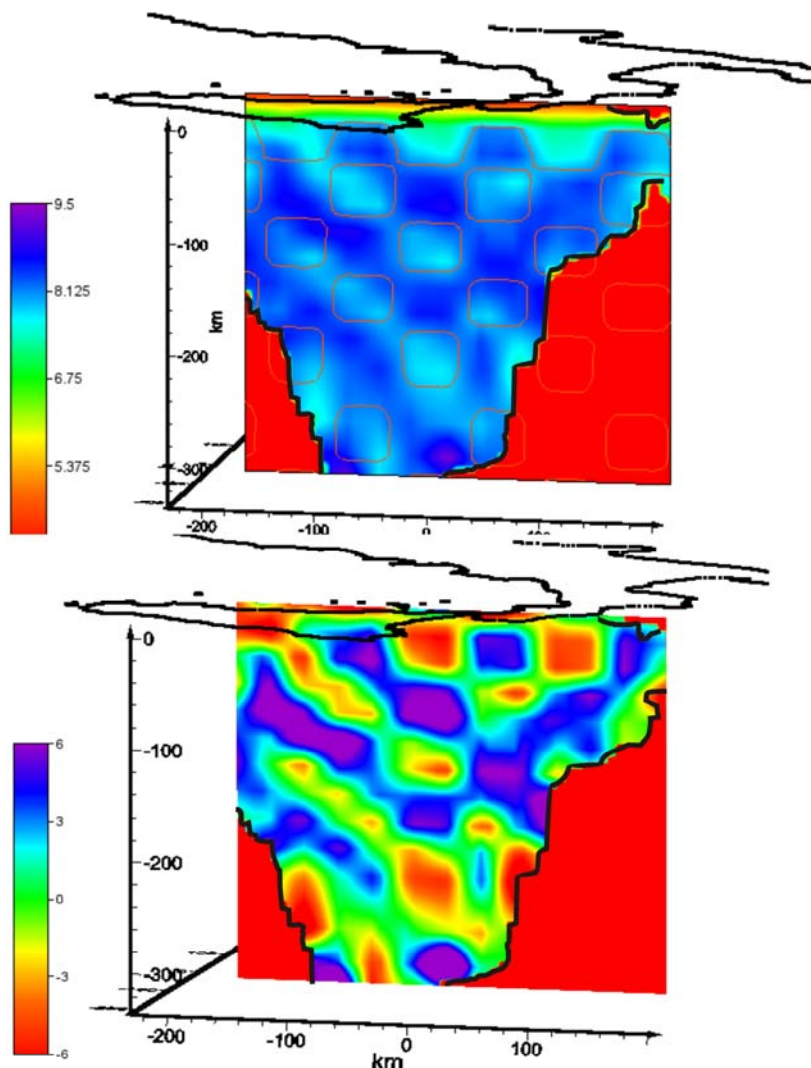
After the optimization of the input inversion parameters (e.g. the damping), the mean percentage restoration inside the *investigated volume* is 71.7% and its variability, in terms of standard deviation, is 26.8%.

The real meaning of this step is that in the best inversion conditions (exact hypocentral positions, exact travel-times calculation and perfect parameterization of the model) we are able to reach a maximum reconstruction possible of the 71.7%, with the selected data and method. Thus, we can never obtain a better reconstruction of the velocity model because there is something - a lack of information and the non-linearity of the inverse problem - that affects our result.

4.7.2 DEPENDENCY OF THE VELOCITY MODEL ON THE HYPOCENTRAL INCERTITUDE

Now we have to consider the effects of the introduction of random errors in the hypocentral coordinates on the velocity model, to better simulate the real conditions of an experimental tomographic study.

In this task the root-mean-square error on the hypocentral locations has been estimated as 2.5 km on the epicentral coordinates and 4.5 km on the depth (see cap 3). Employing a conservative choice, three vectors errors (e_x , e_y , and e_z), having mean 0 and standard deviation 2.5 km, 2.5 km and 4.5 km, respectively, have been added to perturb the hypocentral coordinates.



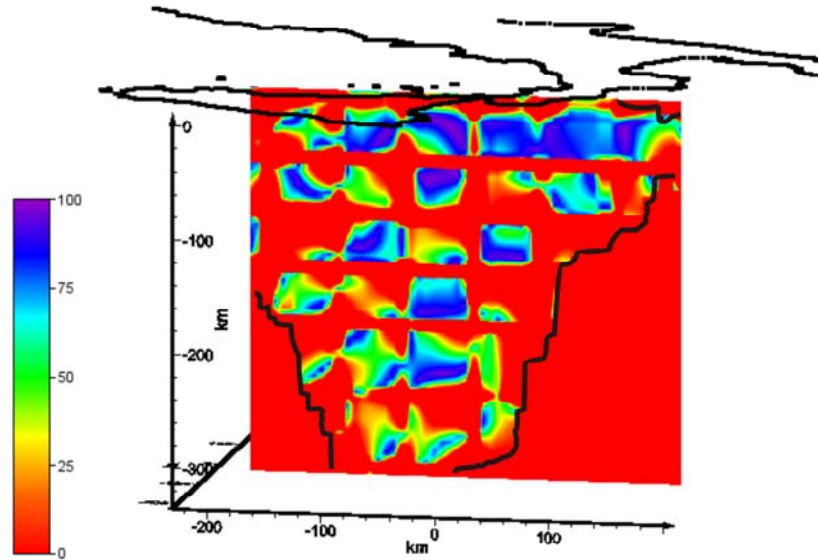


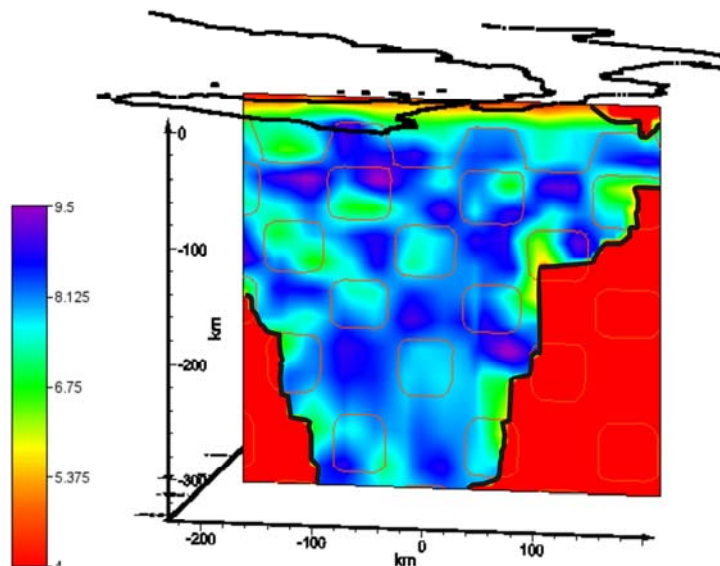
Fig. 4.7.2 – Section of the reconstructed checkerboard Vp model using the exact synthetic travel times and perturbed hypocentral positions (top). On centre it is displayed the same section of the Vp model expressed in percent and bottom the corresponding restoration index distribution. The black lines limit the area of the investigated volume (DWS>100). The lines on the velocity model contour velocity isovalues of the true model represented in the fig. 4.5.1.

The model obtained inverting this data set (hypocentres perturbed, exact travel times and perfect parameterization of the model) clearly shows how the uncertainty of the location events reduced the reconstruction capability and the mean value of R decreased down to 56.7% with standard deviation 30.02%.

At this step we highlight how plausible errors on the hypocentral location can sensibly affect the final velocity model.

4.7.3 DEPENDENCY OF THE FINAL MODEL ON THE PICKING ERRORS

To take into account of the picking errors contained in the experimental data, (mostly conditioned by the signal/noise ratio, by the not perfect regulations of the seismic stations, by the local conditions where are installed the stations, etc.), it is necessary to perturb the travel times. For this task the errors on the picked times (P and S) are simulated adding to the synthetic travel times a vector error having mean 0 s and standard deviation 0.6 s.



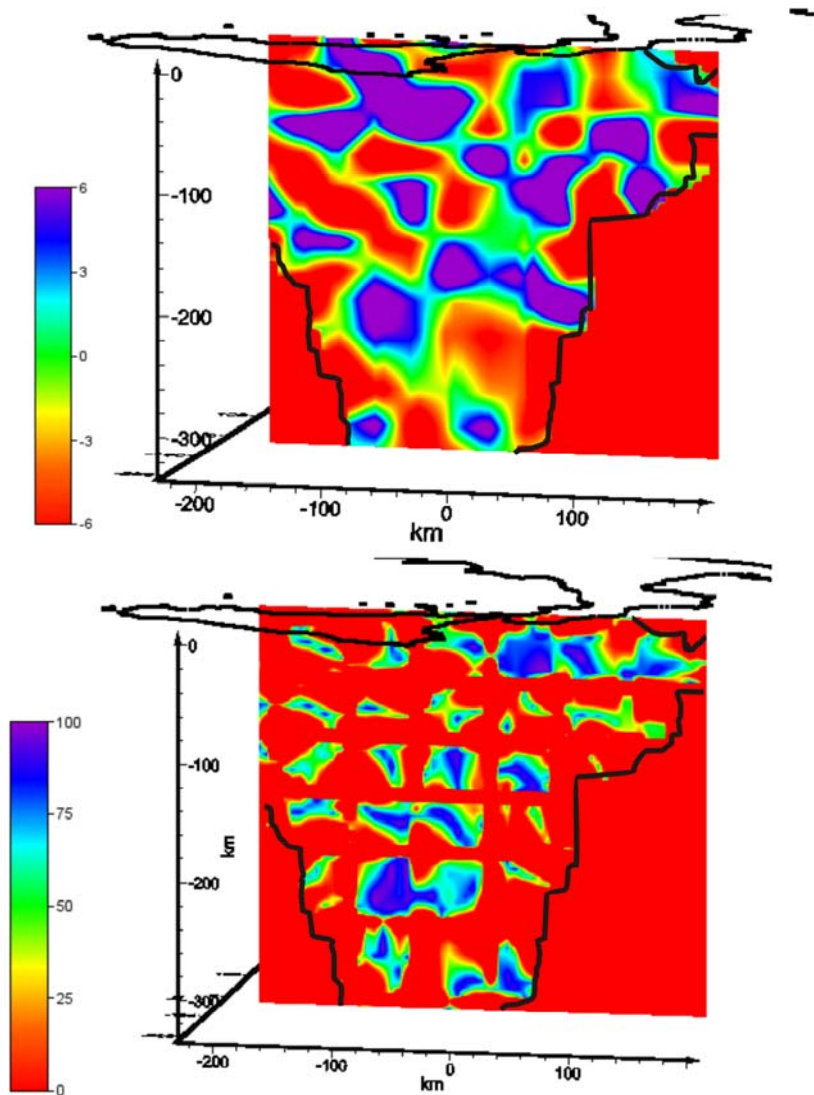


Fig. 4.7.3 – Section of the reconstructed checkerboard V_p model using perturbed travel times and hypocentral positions (top). On centre it is displayed the same section of the V_p model expressed in percent and bottom the corresponding restoration index distribution. The black lines limit the area of the investigated volume ($DWS > 100$). The lines on the velocity model contour velocity isovalues of the true model represented in the fig. 4.5.1

The result of this test shows how the reconstruction capability of the model decreases dramatically when we simultaneously consider both the uncertainty of the hypocentral locations and of the picked arrival-times. The mean R is 51.4% and its standard deviation 30.9%.

The best simulations of the real state of the input data founded in the scientific papers that use the checkerboard test consider only the uncertainty of the hypocentral locations and on the arrival-times.

4.7.4 DEPENDENCY OF THE FINAL MODEL ON THE INVERSION GRID

To really evaluate the reconstruction power in whatever synthetic test it is not sufficient to simulate the real state of the parameters discussed above. In fact, the incapability of perfectly parameterizing the Earth is an aspect that is widely discussed in theoretical papers while it is not sufficiently taken into account during the realization of a synthetic test. Sometimes the optimization of the inversion grid is performed ‘indirectly’ calculating a -

posterior parameters as the spread function that gives an insight into the resolution obtained in the nodes of the grid. To use the same inversion grid for the synthetic test that is used to construct the checkerboard model and then to calculate the travel-times, means to be able to perfectly parameterize the model, and this is not absolutely true in the case of an experimental tomographic study. In that case, then, it is correct to suppose that a synthetic test hoping to fully simulate the real approach of an experimental tomography must consider this impossibility, by performing inversions with grids different from that used to construct the true model.

An example of the results of an inversion that takes into account all the aspects just discussed (i.e. an inversion performed with hypocentres and travel times perturbed and parameterization of the model different from that of the reference model) is shown in figure 4.7.4. In this case, the reconstruction power of the experimental tomography is 46.7% and its standard deviation 31.97%. The velocity model shows patches warped and their absolute velocity values are often over/underestimated. The inversion grid is quite different from the *checkerboard grid* because our aim is to assess the real influence on the model parameterization of the final results.

It is necessary to recall that the first grid has regular dimension of the cells of $28 \times 28 \times 24$ km³, while the second one has average dimension of the cells $17 \times 38 \times 13$ km³.

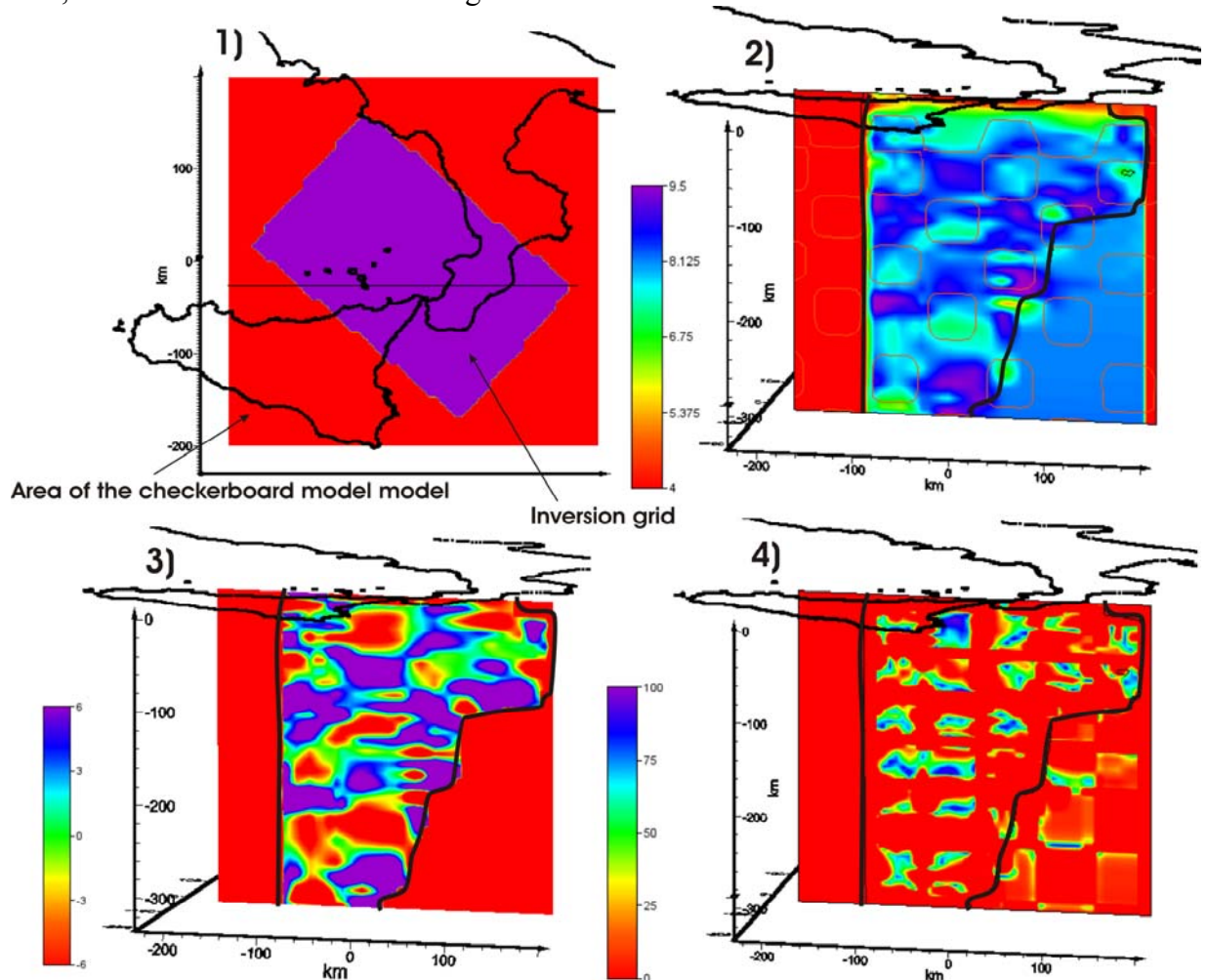


Fig. 4.7.4.1 – Scheme of the inversion grid used to realize the synthetic test with respect the parameterization of the true model (1). Section of the reconstructed checkerboard Vp model using perturbed travel times, perturbed hypocentral positions and inversion grid different (2). The figure 3 displays the same section of the Vp model expressed in percent and the figure 4 the corresponding restoration index distribution. The black lines limit the area of the investigated volume (DWS>100). The lines on the velocity model contour velocity isovalues of the true model represented in the fig. 4.5.1

Another example (figure 4.7.4.2) shows how, a different rotation of the inversion grid allows to recover a model with mean $R = 47.9\%$ and standard deviation 31.49% . The two models obtained are very different and in both cases their reconstruction power unsatisfactory.

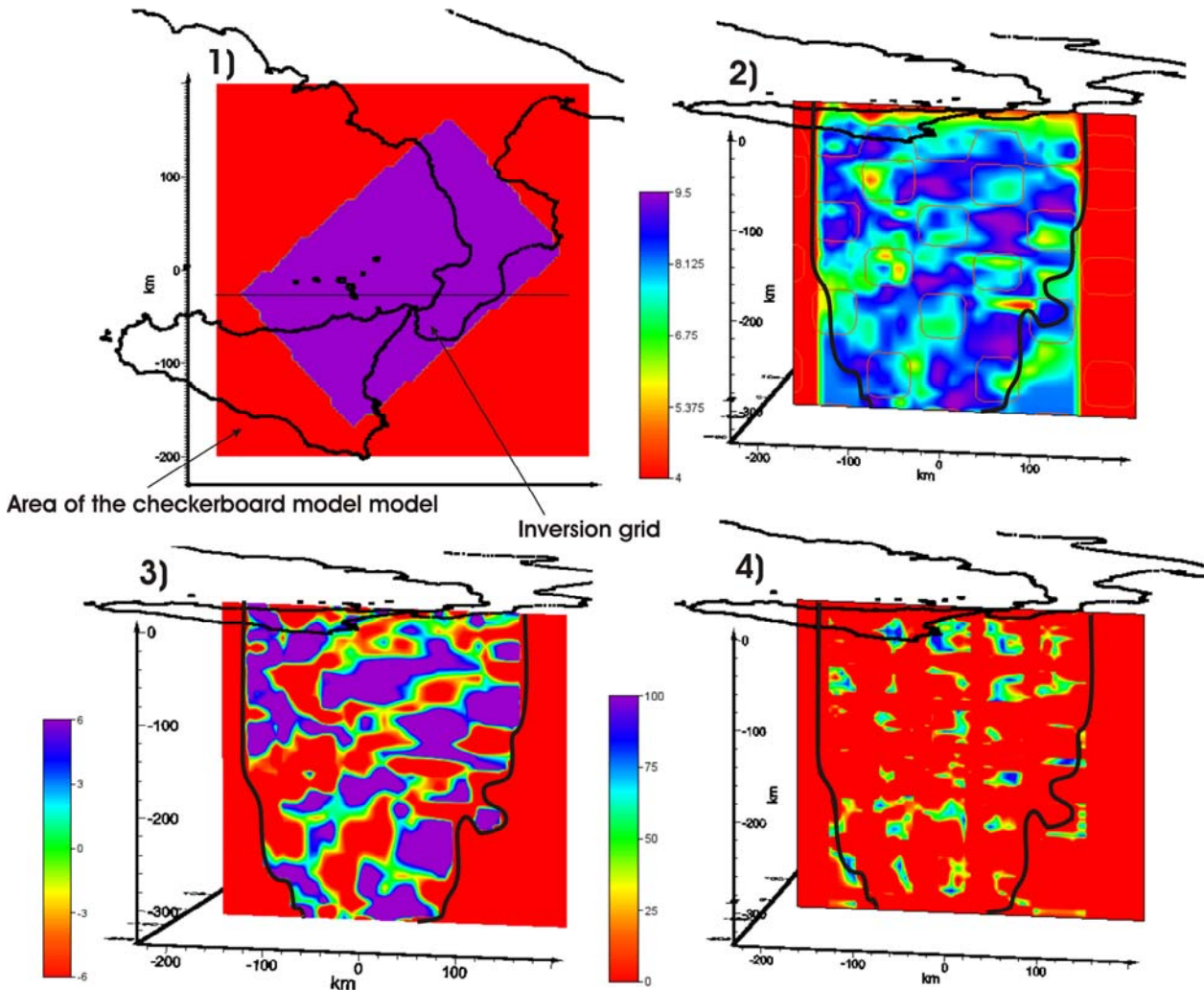


Fig. 4.7.4.2 – Test realized performing an inversion with the grid rotated with respect the test showed in fig. 4.7.4.1 (1). Section of the reconstructed checkerboard Vp model using perturbed travel times, perturbed hypocentral positions and inversion grid different (2). The figure 3 displays the same section of the Vp model expressed in percent and the figure 4 the corresponding restoration index distribution. The black lines limit the area of the investigated volume ($DWS > 100$). The lines on the velocity model contour velocity isovalues of the true model represented in the fig. 4.5.1

The table 4.7.1 synthesizes the results of 21 tests, selected between about 60 inversions, performed by deforming, translating and rotating the inversion grid.

We chose many inversions performed with anisotropic inversion grid and orientations that cover all the azimuths (see paragraph 3.4). Other inversions were performed with different initial models (see paragraph 3.5) and others with different selections of the absolute and differential data (see paragraph 3.6).

Tests with perturbed travel-times (st.d. = 0.6 s), perturbed hypocentral coordinates ($e_x=e_y=2.5$ km, $e_z=4.5$ km), rotated translated and deformed inversion grid					
inversion	Mean(R)	St.d. (R)	inversion	Mean(R)	St.d. (R)
1	46.70	31.97	12	49.71	30.99
2	47.88	31.49	13	50.18	29.48
3	46.09	33.75	14	44.69	34.82
4	46.37	30.26	15	46.76	31.94
5	51.77	29.96	16	45.95	29.57
6	49.71	31.64	17	46.29	31.27
7	44.58	35.7	18	45.84	34.42
8	47.64	29.29	19	47.11	29.77
9	44.53	33.98	20	45.9	34.21
10	46.21	32.71	21	48.83	33.14
11	47.01	32.12	(mean)Total	47.13	32.02

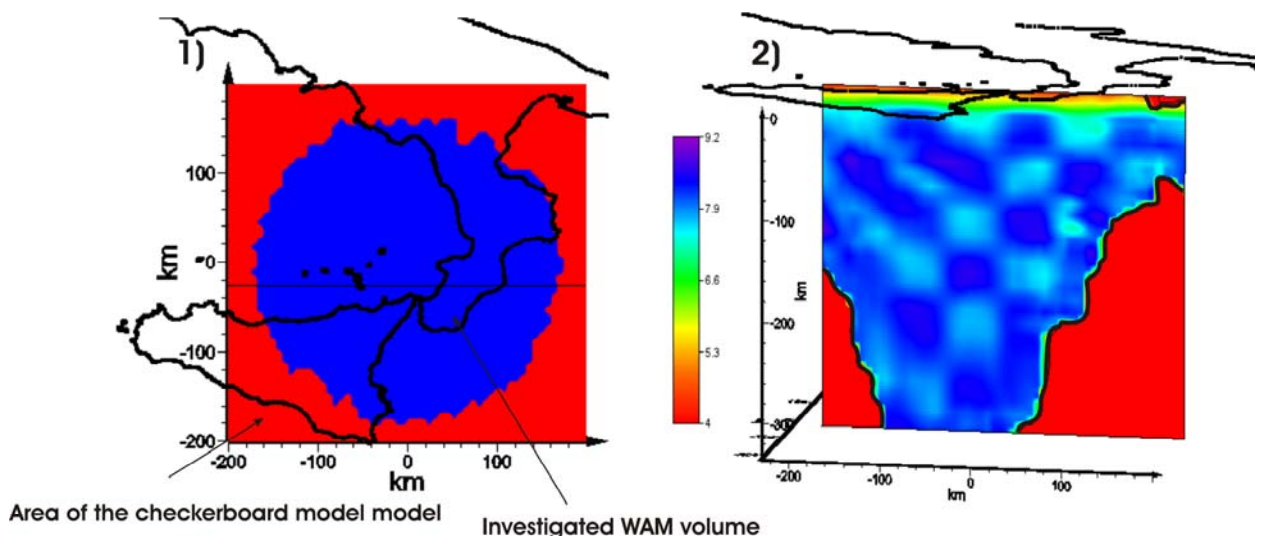
Table. 4.7.1 – Mean restoration and its standard deviation relative to 21 tests performed perturbing the input parameters. The mean restoration of a DD tomography is 47.13% and the standard deviation 32.02%

The mean restoration of the 21 DD ‘classic’ tomographies is about 47 %, showing that the geometric feature of the inversion grid can strongly affect the final results. These results are exact in opposition with the results shown in the previous chapter highlighting how the realization of several tests may not be sufficient to assess the reliability of a tomographic model. One way to overcome the impossibility to optimize the whole set of input parameters could be overcome with a statistical approach as the WAM method.

4.7.5 WAM TEST

Reported in this section are the results of the WAM realized combining the 21 Vp models obtained in the tests above discussed (figure 4.7.5).

In particular, besides some tomographies performed using various selection rules of absolute and differential data, others carried out with 1-D and 3-D starting models and with deformed and translated grids, we picked out several inversions relative to different azimuth of the horizontal edges of the anisotropic grid. The average angular step of the rotations was about 20° and the total azimuth coverage was 180° to recover the spatial isotropy of the tomographic investigation (figure 4.7.5).



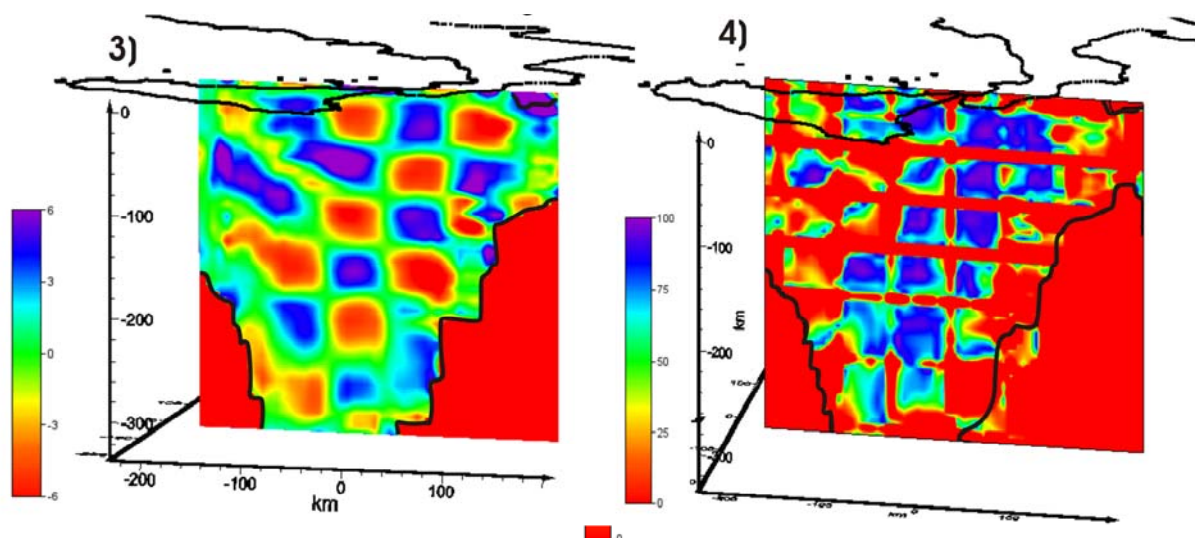


Fig. 4.7.5 – Map of the area covered by the 21 inversions used to construct the WAM (1). Section of the P-velocity WAM model (absolute values (2) and percent values (3)) and relative restoration index distribution (4).

The mean restoration of the WAM was 59.47% and its standard deviation 29.13%. The features of the model are mostly well reconstructed for the *investigated volume* and the absolute velocity values are well recovered as shown in the R distribution that reaches maximum values in the most of the patches. This test shows that a good model can be recovered averaging several models with spatial distributions of weights ‘normalized’ across the whole set of the models employed.

4.8 Effectiveness of the WAM Method

The WAM method generates models having a better reliability and an higher reconstruction index than classic “DD” tomographic models. In the next paragraph some features that support the WAM technique are discussed.

4.8.1 RELATIONSHIPS BETWEEN RESTORATION INDEX AND ORDER OF THE WAM

A WAM is the result of a post processing weighting technique that unifies several models and its reliability strongly depends on the number of the models that are used to build it, i.e. from the *order* of the WAM. In the graph of figure 4.8.1 it is possible to see how increases the restoration index with the WAM order. After a strong rise of R between the order of 4 and 10, we see a gradual decrease of the rate increase of R with the WAM order. This trend gives insight into the maximum mean R that it is possible to reach with the data selected. However, this trend is affected by the sampling technique of the model space and then from the perturbation procedure of the input parameters.

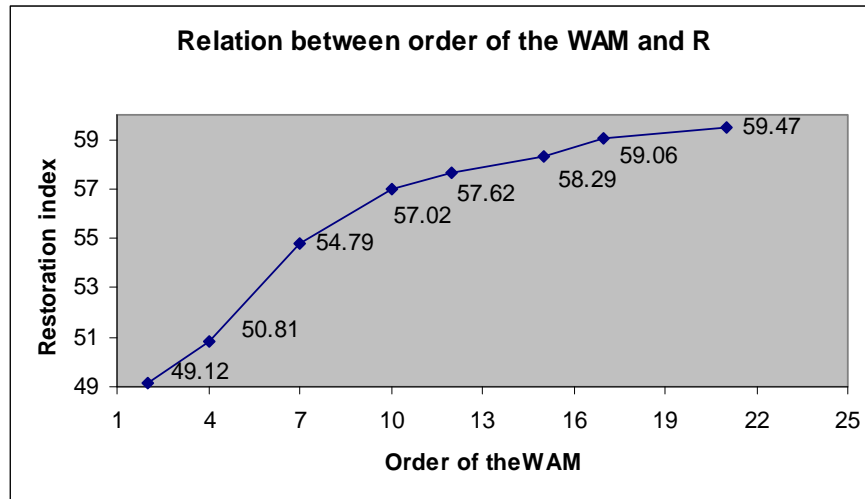


Fig. 4.8.1 – Relation between order of the WAM and restoration index

4.8.2 RELATIONSHIPS BETWEEN RESTORATION INDEX AND STANDARD DEVIATION

An important characteristic of the WAM technique is the link between the restoration index (computable only in synthetic tests) and the velocity standard deviation of the WAM. The standard deviation in the WAM nodes is determined using the same weights adopted to calculate the mean velocity and discussed in the paragraph 4.4. In the figure 4.8.2.1 it is possible to see that, where R is low, there are often high values of standard deviation and vice versa, showing an anti-correlation between these two parameters.

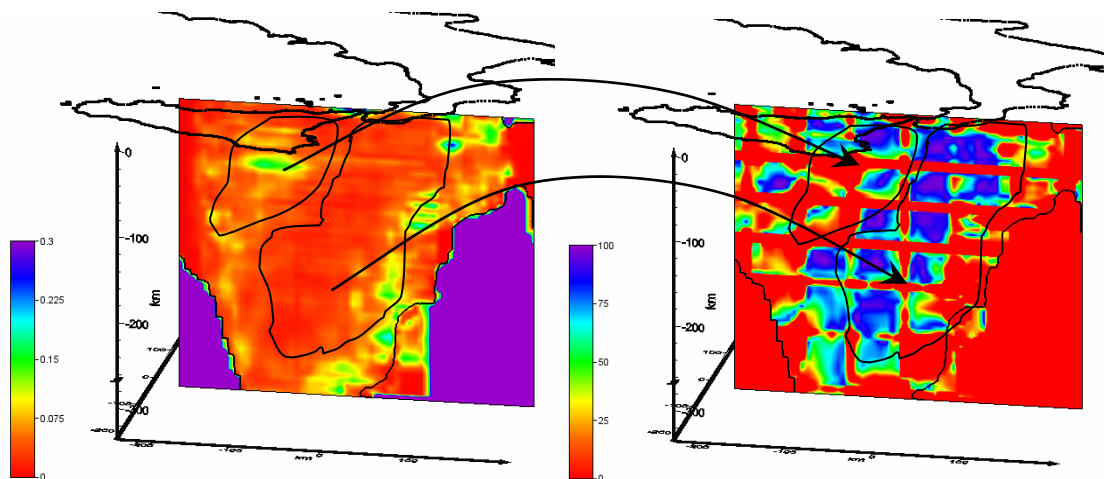


Fig. 4.8.2.1 – Comparison between velocity standard deviation (left) and restoration index (right) of the WAM. It is clearly visible how in the parts of the model where there are high values of the standard deviation correspond low values of R.

To verify this link, we carried out a correlation analysis performing a ‘bin sampling’ on ten classes inside the *investigated volume*. The graph of the figure 4.8.2.2 shows a smoothed anti-correlation trend (blue line).

Its variability in each bin is clearly lower than the average value, so we can assume that the trend is reasonably reliable.

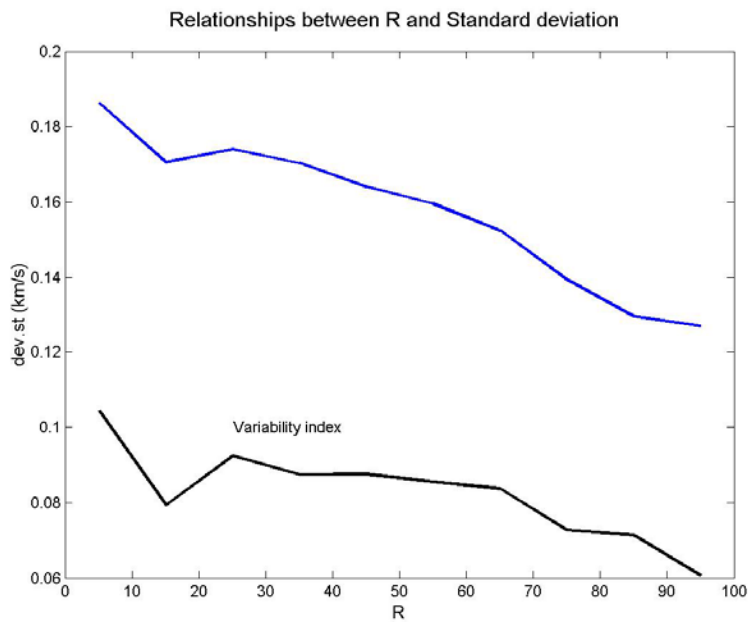


Fig. 4.8.2.2 – Relationships between standard deviation and R. The blue line indicates the trend while the black one its variability.

The same cannot be said for the correlation analysis between R and DWS, because the apparent positive correlation (blue line) is clearly not reliable as indicated by the high values of variability index in each bin (black line).

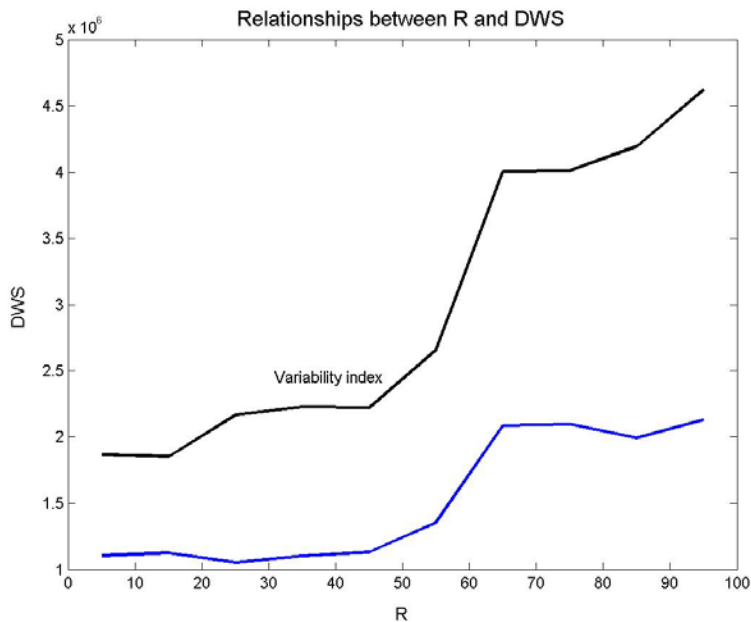


Fig. 4.8.2.3 – Relationships between DWS and R. The blue line indicates the trend while the black one its variability.

The tests above discussed show that it is not possible to determine the reliability of the velocity in a node using only the DWS value as shown in many tomographic studies. Furthermore, the ‘classic’ tomographies are not able to determine parameters connected to

the experimental information correlated to the reconstruction power while the WAM method gives a parameter (the standard deviation) useful to infer the reliability of the velocity in each node of the model.

4.8.3 INFERENCES ON THE WAM GRID AND ITS IMPORTANCE

In this paragraph we will answer the following questions:

- 1) Is it correct to transport the velocity model from the inversion grid into a WAM grid?
- 2) Is it reasonable the resampling into a finest grid?

It is crucial to remember that the resampling of the inversion grid into the WAM grid was performed using the same interpolation algorithm used by the inversion program. This assures the absence of any added error because the velocity model is considered by TomoDD as a continuous velocity field represented by the 8 nodes that define each cell of the inversion grid. We called WAM grid the 3-D grid that we used to construct the WAM.

To answer the second question we performed the following test.

First we resampled each velocity model obtained during the construction of the *extended* checkerboard test into a WAM grid with cell size $28 \times 28 \times 24 \text{ km}^3$. Practically, each resampled model could be considered as WAM of order 1 (we will call WAM_n the WAM of order n).

Subsequently, we calculated the standard deviation between 8 different WAM_1. The variability between these 8 WAM_1 gives insight into the incertitude of the velocities of a “DD” model and its value was estimated on 0.53 km/s (first value of the graph 4.8.3.1).

Finally, we determined the standard deviation with the same method for different orders of WAM. Each standard deviation is calculated using 8 independent models.

The results, displayed in figure 4.8.3.1, show how the standard deviation decreases consistently from 0.563 km/s down to 0.201 km/s, from the WAM_1 to the WAM_10.

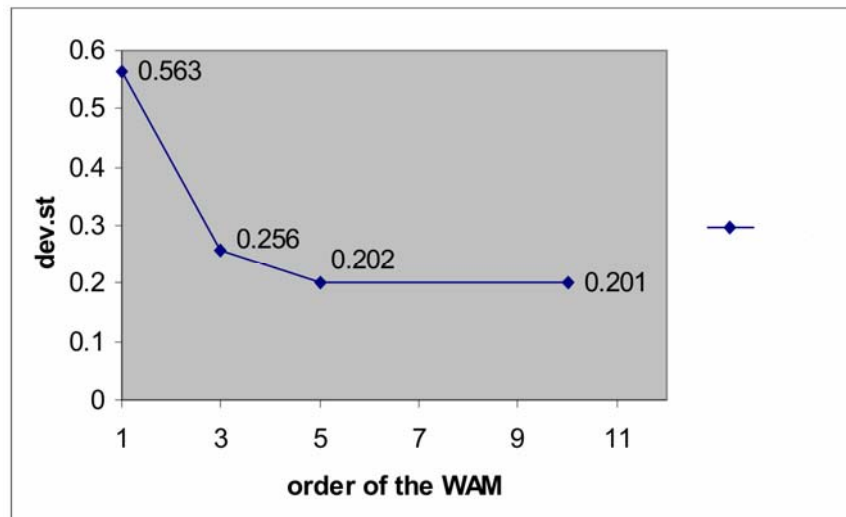


Fig. 4.8.3.1 – Trend of the standard deviation, calculated using 8 independent models, with respect the order of the WAM. The models are resampled into a WAM grid with cells size of $28 \times 28 \times 24 \text{ km}^3$.

This step of the test describes another feature of the WAM method because it shows how the variability of the 8 models decreases when increases the order of the WAM highlighting a convergence in the space of the possible models. A WAM with more models is more reliable than one of minor order as shown in the paragraph 4.8.1.

The same procedure was performed using the same models, but resampling them into a WAM grid with cell size $7 \times 7 \times 6 \text{ km}^3$. The figure 4.8.3.2 displays the results of this test

(yellow line) together with the results of the previous one (blue line). It is possible to see the coherent trend of the two lines but the standard deviations determined during the second test are lower than those of the first one.

We explain the shift toward lower values of the curves as an effect of the nodes that resample the models inside the cells of the inversion grid. In fact, it is probable that the velocity field is more stable inside each cell than the velocity values determined in the nodes. The stability is realized with reciprocal compensations of the velocity variations in the 8 vertices of each cell. Furthermore, we did not observe instabilities in the model still using the finest WAM grid. The test suggests only the validity of the procedure, but did not permit to determine the minimum cell size of the WAM grid permitted by our data set.

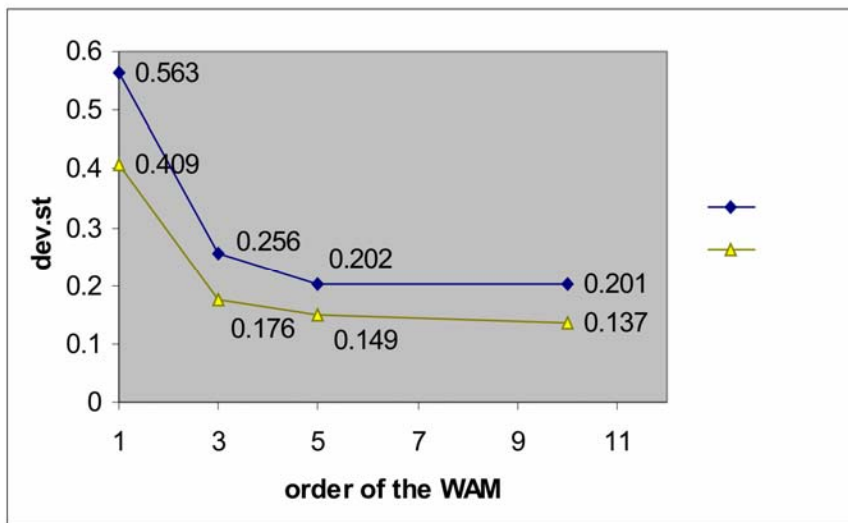


Fig. 4.8.3.2 – Trends of the standard deviation, calculated using 8 independent models, with respect the order of the WAM. The blue line is relative to the test performed with models resampled into a WAM grid with cells size of 28x28x24 km³, while the yellow one for models resampled into a WAM grid with cells size of 7x7x6 km³.

We could potentially resample the models into WAM grids finer than the grid tested without adding biases but the time of computation increases considerably taking into account that in these tests, normally, we resampled inversion grids with 3276 nodes into the WAM grid having 198476 nodes when we used 7x7x6 km³ as dimension of the cell sizes.

The WAM method permitted the acquisition of a model of reliable P- waves, and the synthetic tests gave information on its reliability and on the link existing between the restoration index and a parameter, the WAM standard deviation, that can be calculated in experimental data inversions. Similarly, we may assume that analogous deductions can be formulated for WAM coming from inversions that use S experimental arrival times.

The increased reliability of the velocity models with the WAM method will allow us to use them not only for the geometric description of the underground structures but also for petrographic interpretations and reologic inferences.

5. WAM of the Southern Tyrrhenian Region

5.1 Introduction

To construct the V_p , V_s and V_p/V_s WAMs among all velocity distributions obtained in more than 60 experimental inversions, we selected $n=27$ models. These models are characterized by the largest average L_2 norm of the deviations from the others, to perform a wide and homogeneous sampling of the model space.

We also determined the average hypocentral distributions using the same 27 models. The mean standard deviation of each hypocentral coordinate is $\sigma_x=2.83$ km, $\sigma_y=2.69$ km and $\sigma_z=3.26$ km, the mean RMS is 0.11 s with standard deviation 0.05 s.

5.2 V_p WAM. Deep Structures

We represented three horizontal and three vertical sections of WAM (figure 5.2.1) to enhance some geometric features of the main anomalous bodies of the subducting Ionian slab and southern Tyrrhenian mantle.

We assessed the reliability of these bodies by studying the weighted standard deviation distribution of WAM, determined as the standard deviation of the 27 models divided by the square root of the number of models. The standard deviations were smaller than 0.06 km/s for most of the model and reached 0.12 km/s in some border areas. These values are significantly lower than the observed amplitude of the velocity anomalies that characterize the area, and even taking into account a margin of error of 2σ ($\sim 95\%$ confidence interval), the reliability of the anomalous bodies remains high.

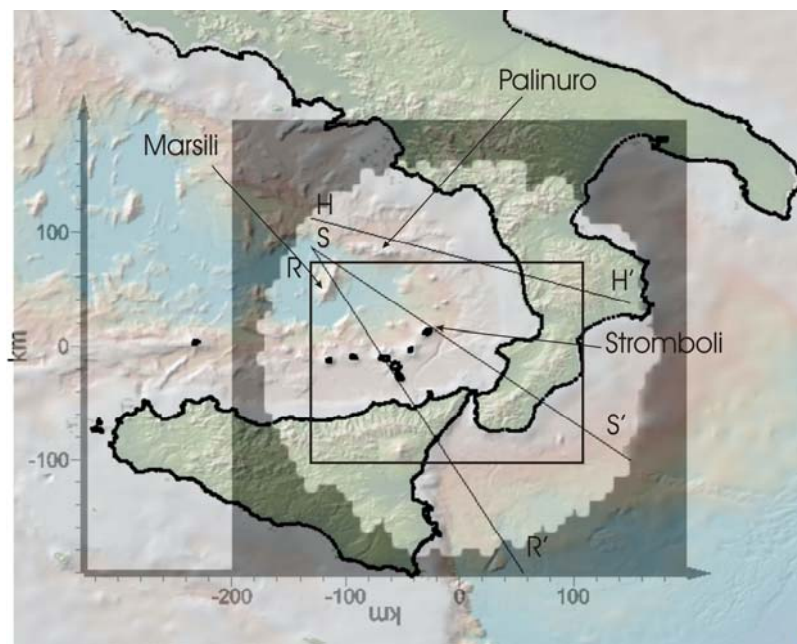


Fig. 5.2.1 – Map showing the covered area of the V_p WAM with $DWS > 100$ (white area inside the grey one), the area target of the horizontal sections (black rectangle) and the three vertical sections (R-R', S-S' and H-H').

The horizontal slice of the V_p model at a depth of 100 km (figure 5.2.2a), shows a low velocity area ($6.6 < V_p < 7.7$ km/s) NW of the Aeolian islands almost beneath the Marsili seamount (3). The hypocentres, within ± 25 km from this section, are located within an SW-NE elongated high velocity body ($V_p > 8.2$ km/s) that images a portion of the Ionian

slab (1). There is a remarkably low- V_p area ($6.6 < V_p < 7.7$ km/s) beside this body, located below the Calabrian arc (2). The low velocity body seems to be sandwiched between two high- V_p bodies (sequence 1-2-4).

The section at a depth of 170 km (figure 5.2.2b) clearly shows the concave shape of the Ionian slab, here characterized by a 50-60 km large high velocity area (1). In this slice the low- V_p area, just beneath the Calabrian arc, is somewhat discontinuous (2). The low velocity region NW of the Aeolian arc is still present (3).

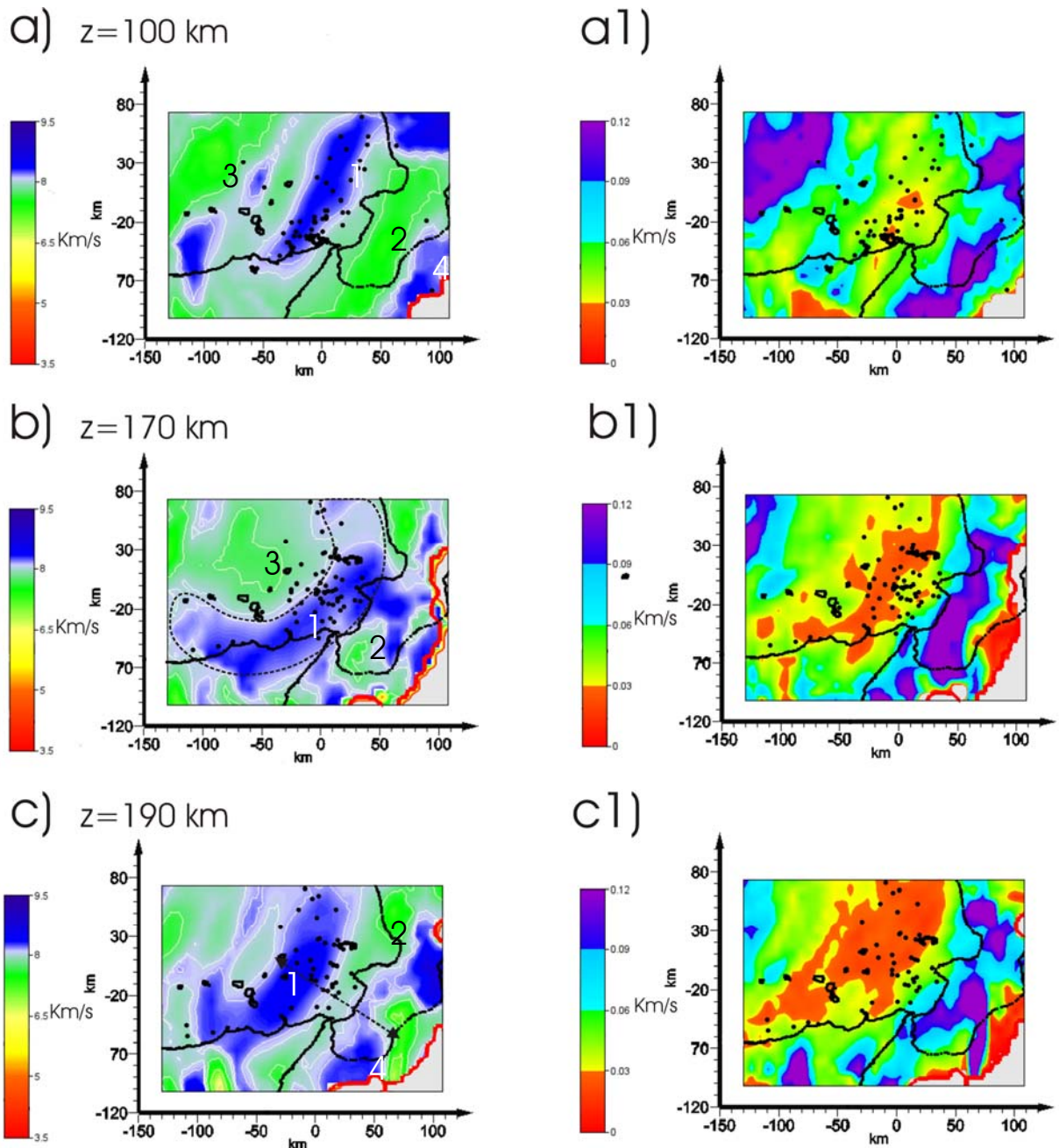


Fig. 5.2.2 – Velocity planes at depths of 100, 170 and 190 km (a, b, c, respectively) and corresponding standard deviation distribution (a1, b1, c1, respectively). The red lines limit the portion of the poorly resolved model ($DWS < 100$). The black points are the projections onto the given plane of the hypocenters within ± 25 km. The dashed black line in the slice at a depth of 170 km highlights the concave shape of the Ionian slab. The dashed double arrow in the slice at a depth of 190 km indicates the sandwich slab structure.

At a depth of 190 km (figure 5.2.2c) the sandwich structure identified at depth of 100 km is even clearer (sequence 1-2-4), and it is characterized by high V_p with a thin (20-25 km) low velocity layer. It is worth noting that at this depth the low velocity anomalies beneath the Marsili area are no longer imaged.

The vertical section S-S' of the V_p model (figure 5.2.3) depicts a portion (50-60 km thick) of the steeply dipping (69° - 72° towards NW) descending Ionian slab, which is characterized by high velocities having values of $V_p > 8.2$ km/s (1).

Recent seismic studies using the Near-Vertical Reflection technique (CROP project; *Finetti*, 2005) have detected a thin, steep reflective layer down to a depth of about 140 km, which has been interpreted as being the top portion of the Ionian slab. It is portrayed in figure 5.2.3 within the high V_p region (with dashed line). Just below the high V_p , there is a 20 - 25 km thick area characterized by discontinuous bodies having values of V_p 6.6 - 7.7 km/s (2). These low velocity bodies dip coherently with the overlying high velocity ones and fade out at a depth of 230-250 km. On the top of the Ionian slab vertically elongated low-velocity areas ($V_p \leq 7.0$ km/s) beneath the Stromboli and Marsili volcanoes reach a maximum depth of 180 km (3).

The standard deviation of the WAM highlights how the border areas are less reliable than the central ones, however the lateral heterogeneity amplitudes are always at least 4 times the corresponding standard deviation; this supports their existence.

The sections H-H' and R-R' (figure 5.2.4 and 5.2.5) have been traced in the southeastern and northwestern part of the subducting slab, respectively. The profiles show how there is not a continuous high velocity body (1) characterizing these portions of the Ionian lithosphere as well as shown in the central section (S-S'). In section H-H' the interruption of the high V_p body is between 120-210 km of depth (2), while in R-R' it is between 80-120 km (2).

In section H-H', the deep low velocity areas beneath the Tyrrhenian sea are still present but confined in its northeastern part of the southern Tyrrhenian basin (3), approximately below the Palinuro seamount, while in the section R-R' are mostly located below the Aeolian Archipelago and the Marsili seamount (3).

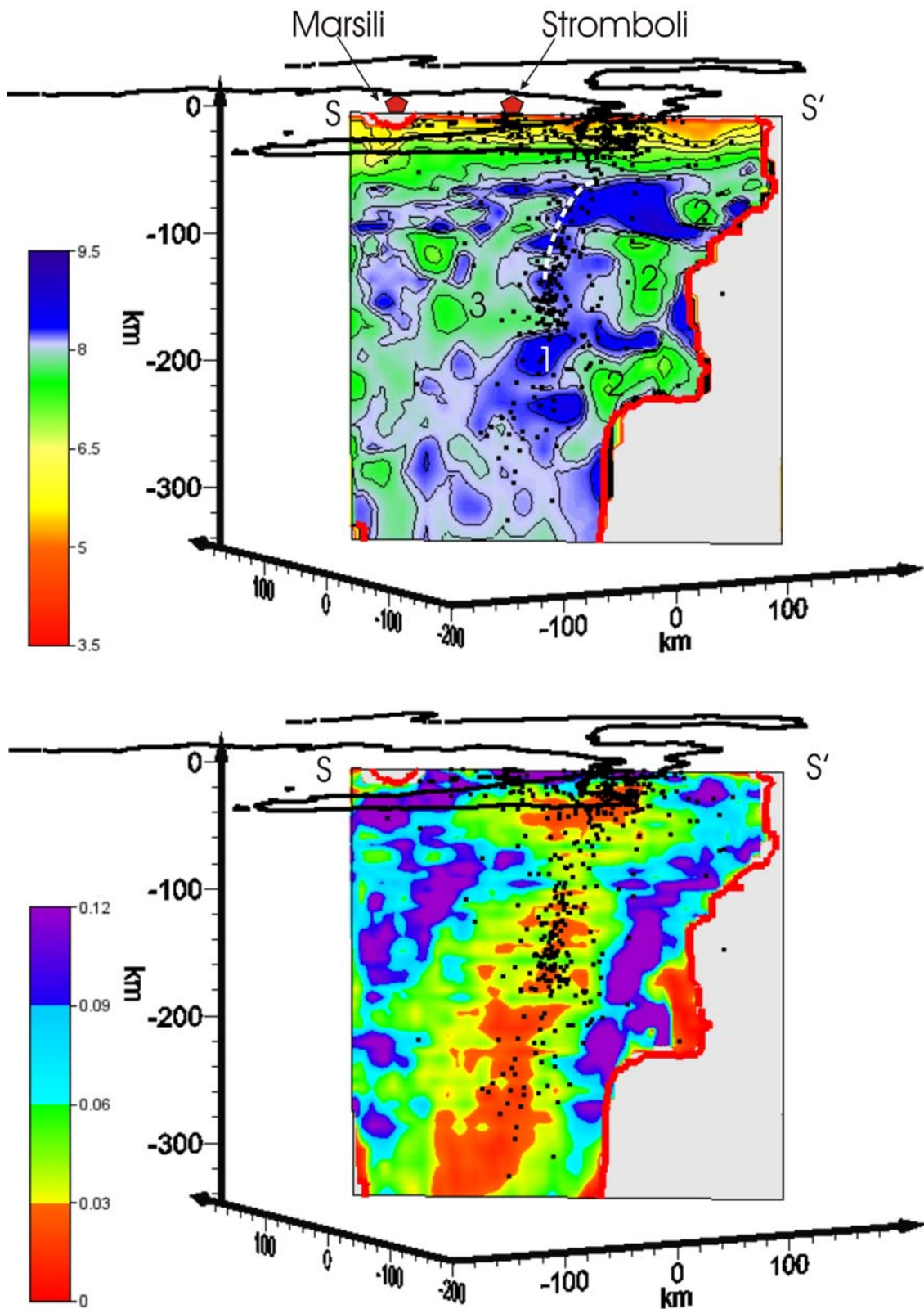


Fig. 5.2.3 –S-S' Vp WAM (top) and corresponding distribution of the standard deviation (bottom). Earthquakes within 15 km of the sections are also plotted. The best resolved area ($DWS > 100$) lies above the red line. The white dashed line in the Vp model is the trace of the NVR interpretative section (Finetti, 2005). The body marked with the number 1 is the high velocity portion of the subducting slab, the bodies with the numbers 2 and 3 are low velocity areas within and outside the Ionian lithosphere, respectively.

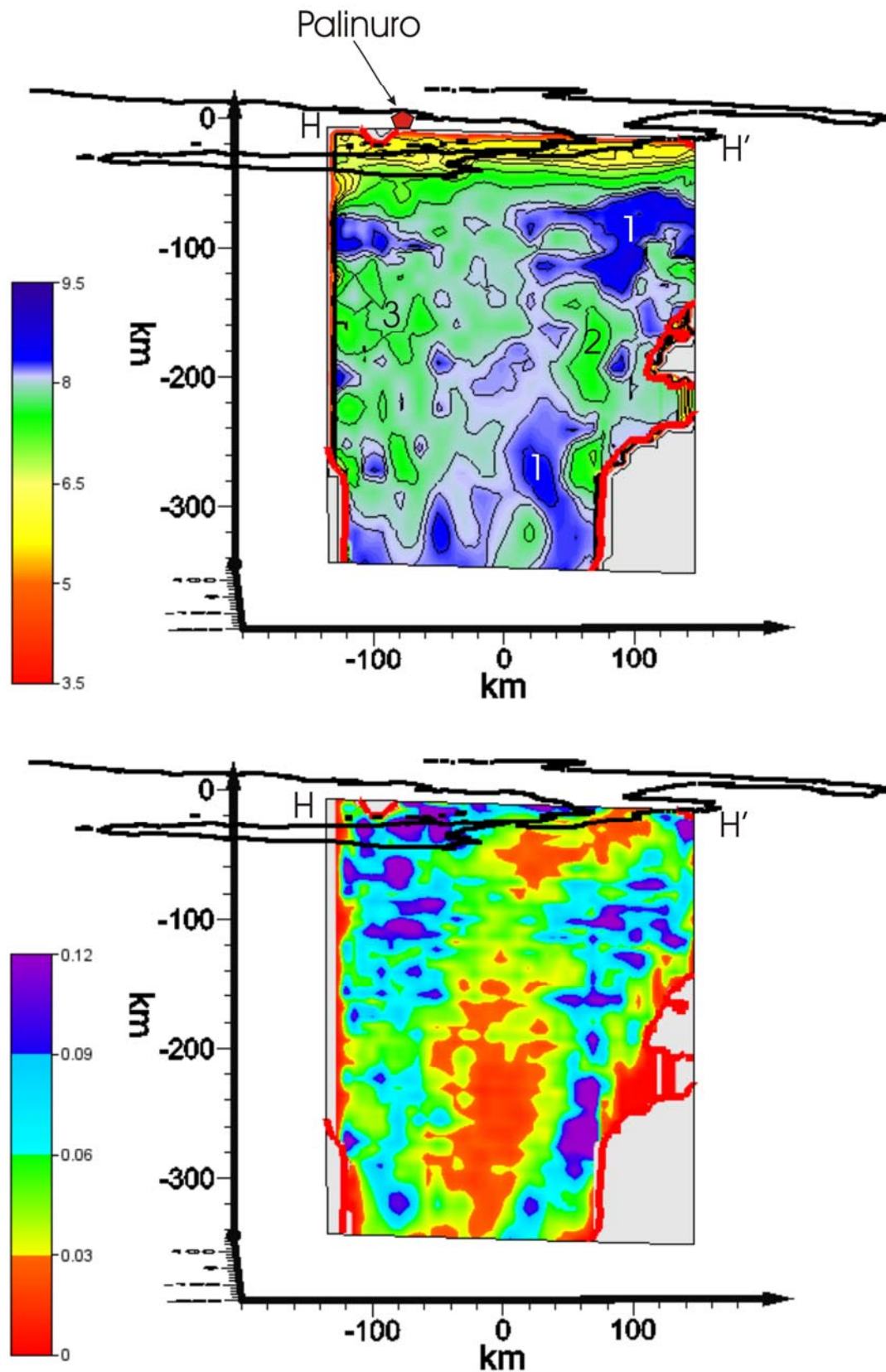


Fig. 5.2.4 –H-H' V_p WAM (top) and corresponding distribution of the standard deviation (bottom). The best resolved area ($DWS > 100$) lies above the red line. The bodies marked with the number 1 represent the high velocity portion of the subducting slab, the bodies with the numbers 2 and 3 are low velocity areas within and outside the Ionian lithosphere, respectively.

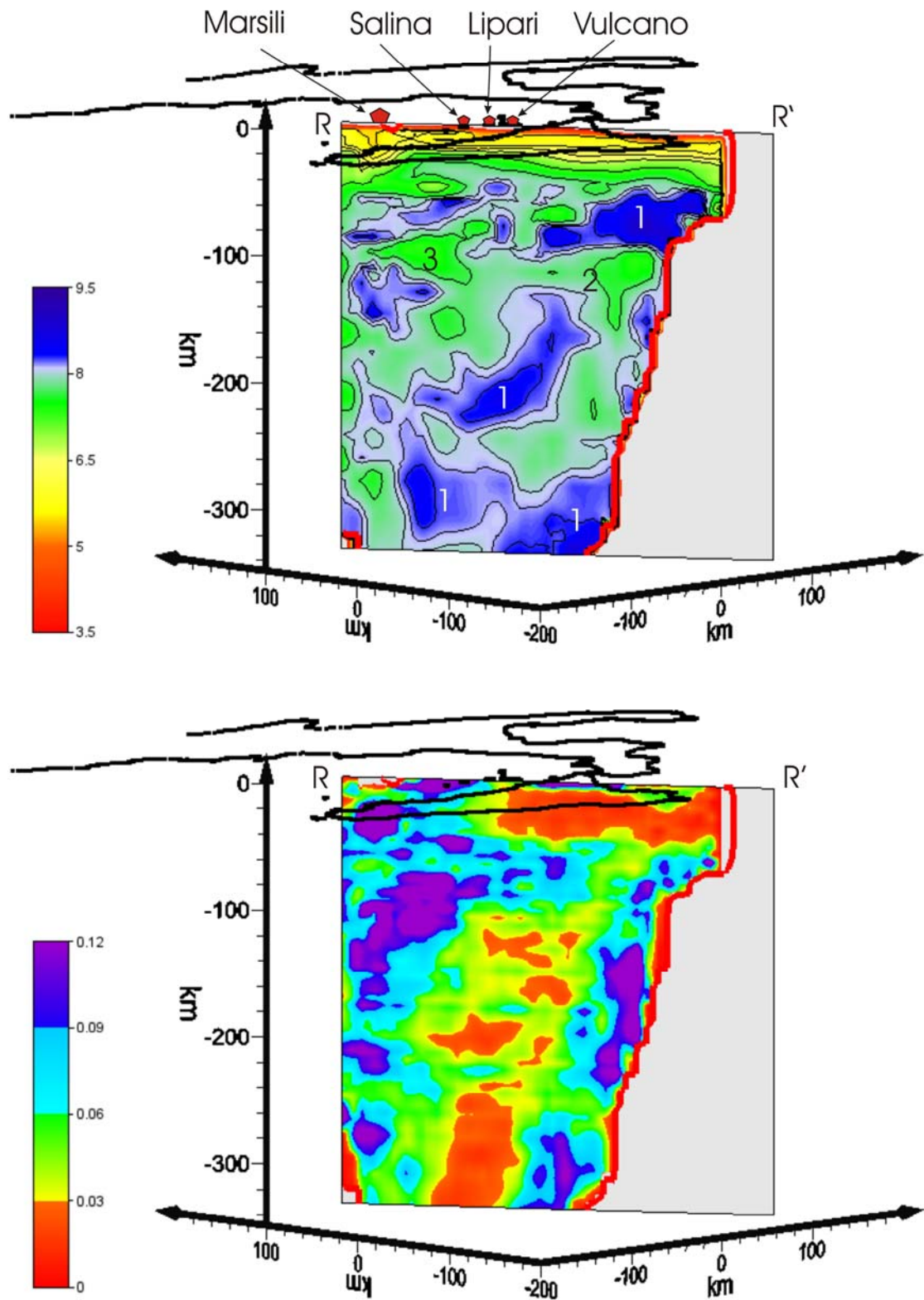


Fig. 5.2.5 -R-R' Vp WAM (top) and corresponding distribution of the standard deviation (bottom). The best resolved area ($DWS > 100$) lies above the red line. The bodies marked with the number 1 represent the high velocity portion of the subducting slab, the bodies with the numbers 2 and 3 are low velocity areas within and outside the Ionian lithosphere, respectively.

The three sections traced above suggest that the Ionian slab has the shape of an *asymmetric hourglass* which is difficult to describe with 2-D sections. A 3-D WAM representation (figure 5.2.5) shows the part of the Ionian lithosphere characterized by velocity greater than 8.15 km/s. Now we can more clearly see the effective shape of the descending slab and how its width, at a depth of 100 km, is less than in the upper and lower parts (yellow dashed lines in figure 5.2.5). Furthermore, it is possible to see how the hypocenters used to realize the velocity model are distributed, with similar geometrical features, within the dipping high Vp slab (figure 5.2.5 bottom and figure 5.2.6).

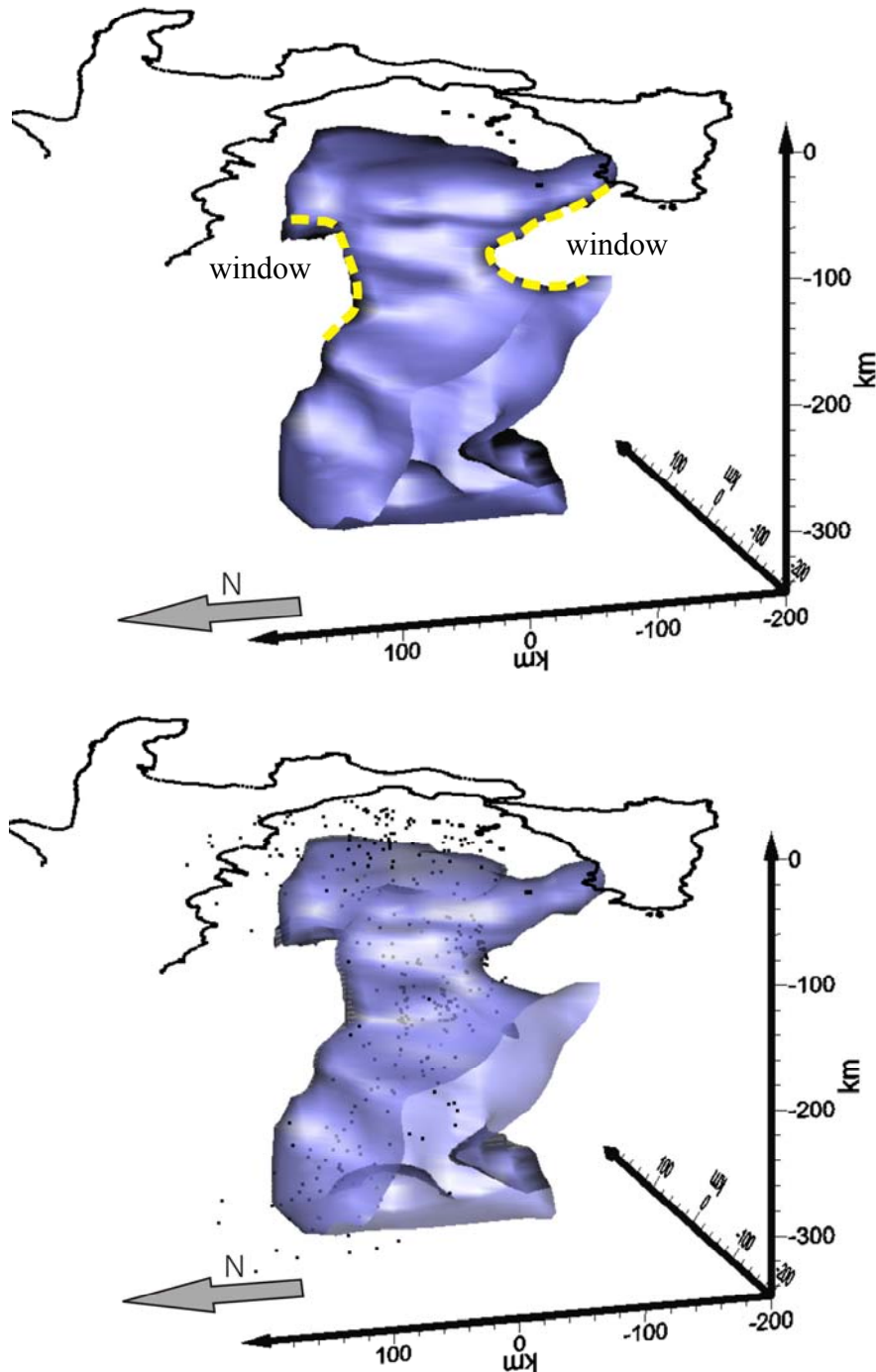


Fig. 5.2.5 –3-D Vp WAM. The isosurface encloses the volume of the Ionian lithosphere with velocity greater than 8.15 km/s (top) the yellow dashed lines highlight the *asymmetric hourglass* shape of the slab. On the bottom the same surface is plotted together the deep hypocenters relative to the events selected to realize the Vp model.

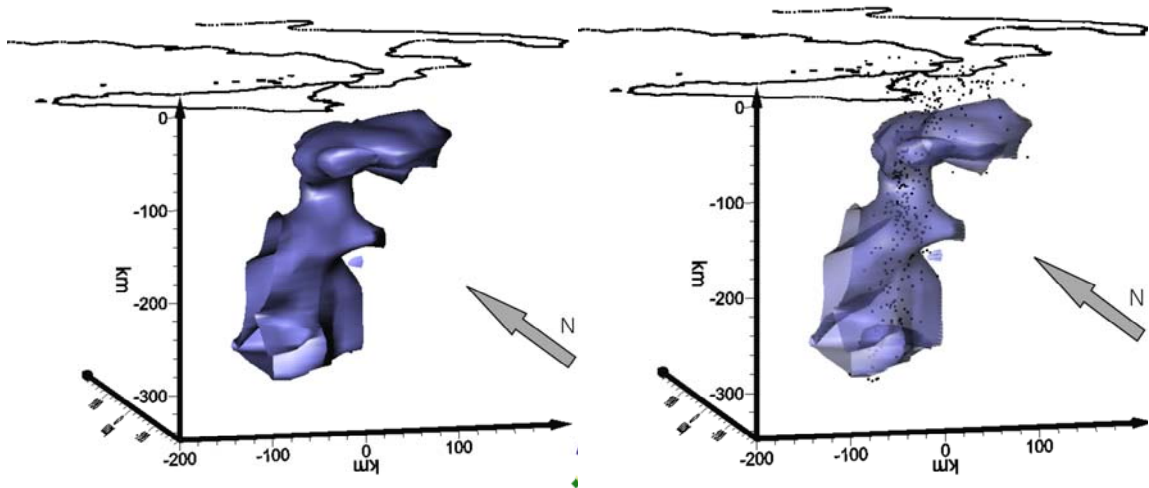


Fig. 5.2.6 – 3-D Vp WAM. The isosurface encloses the volume of the Ionian slab with velocity greater than 8.15 km/s (left). On the right the same surface is plotted together with the hypocenters relative to the deep events selected to realize the Vp model. It is clearly visible how the hypocenters are well contained into the volume delimited by the isosurface at 8.15 km/s.

A view from the south (figure 5.2.7) shows the geometric features of the low velocity bodies (Vp less than 7.7 km/s) just underlying the upper portion of the Ionian lithosphere. These bodies are mostly located at a depth of 100-150 km reaching a maximum depth of 230-250 km.

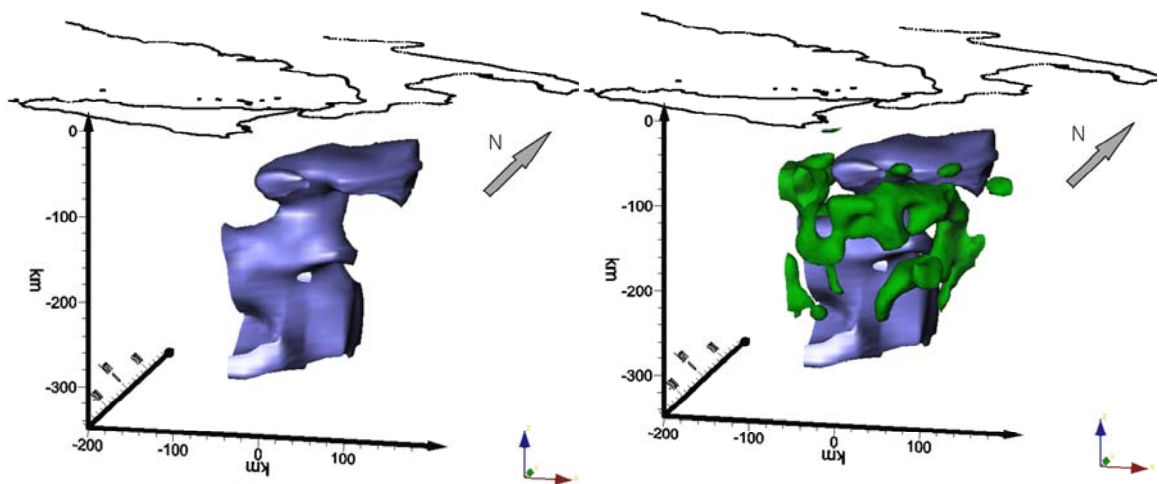


Fig. 5.2.7 – View of the 3-D Vp WAM from the south. The isosurface encloses the volume of the Ionian slab with velocity greater than 8.15 km/s (left). On the right the same surface is plotted together with the isosurface that encloses the bodies underlying the high Vp slab. These bodies have velocities less than 7.7 km/s and have a max thickness of 30-35 km.

Finally, in figure 5.2.8 we show the low velocity bodies beneath the southern Tyrrhenian sea. It is possible to see how at a depth between 100-180 km (figure 5.2.8 bottom) the low Vp volumes are located below the Marsili oceanic basin and beneath the major volcanoes present in this region (Stromboli, Marsili and Palinuro seamounts).

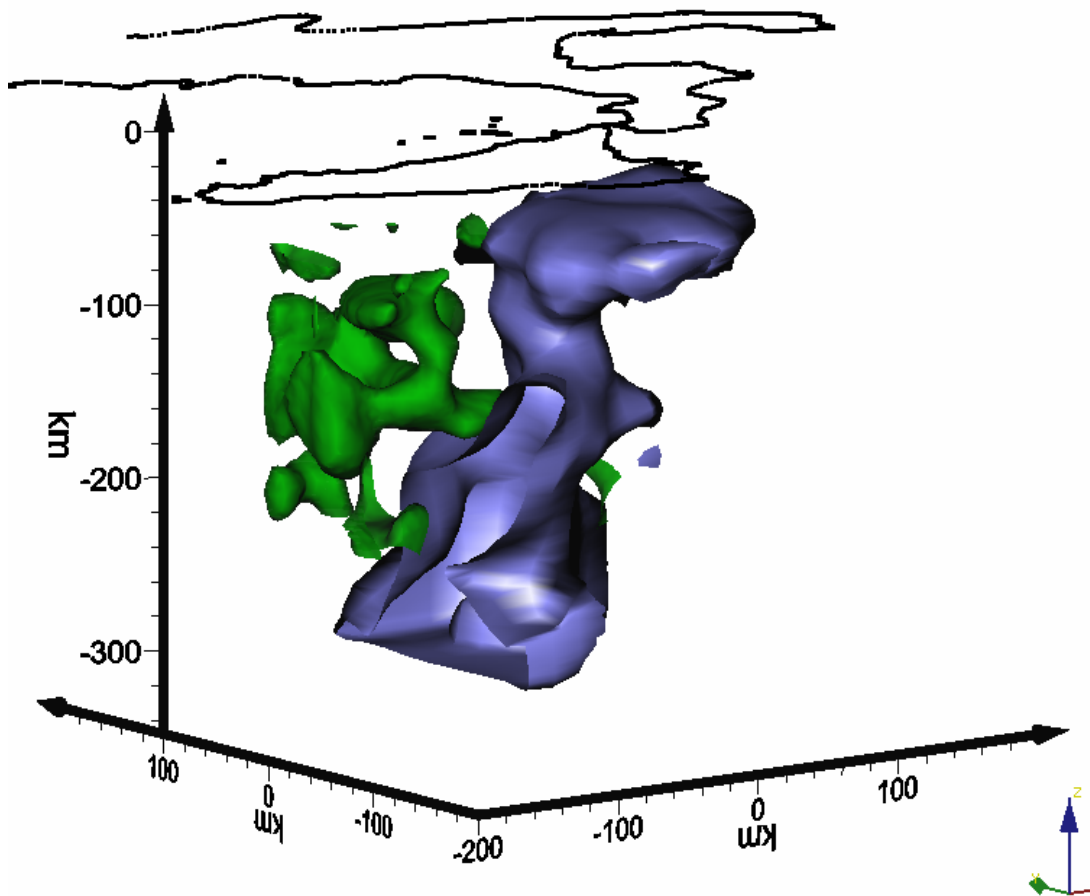
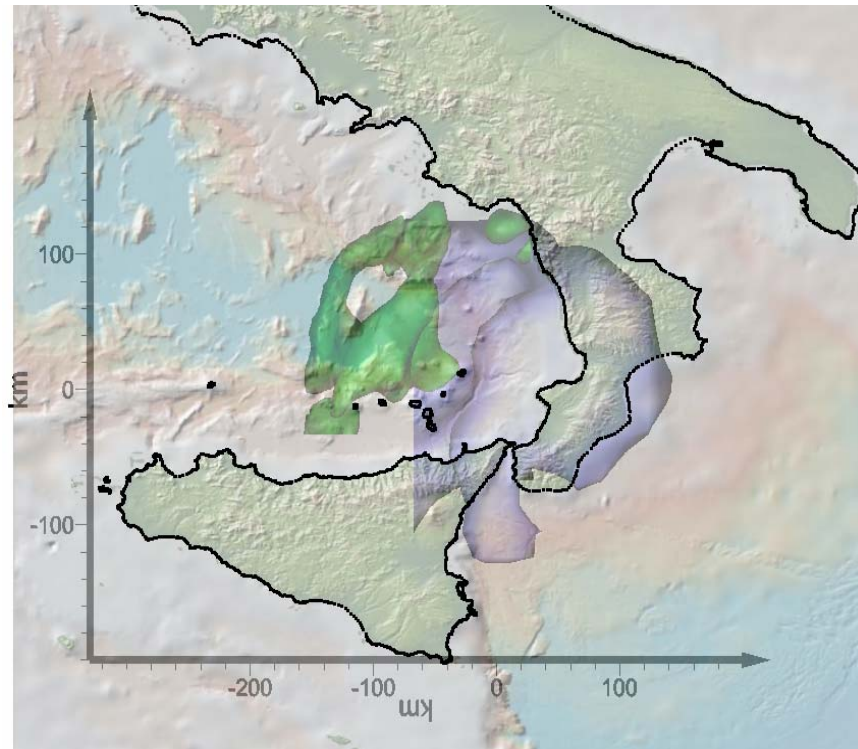


Fig. 5.2.8 – Projection of the low Vp bodies (less than 7.7 km/s) beneath the southern Tyrrhenian basin and with respect the Ionian slab (top) relative to the 3-D view of these bodies (bottom). The displayed low Vp bodies are mostly placed between 100 and 200 km.

5.3 Vs WAM. Deep Structures

We recovered similar features with the WAM method using the S waves even if the lower coverage of the experimental information with respect to the Vp WAM is evident. In fact the *investigated volume* (DWS>100) is smaller than that of the Vp WAM (figure 5.3.1).

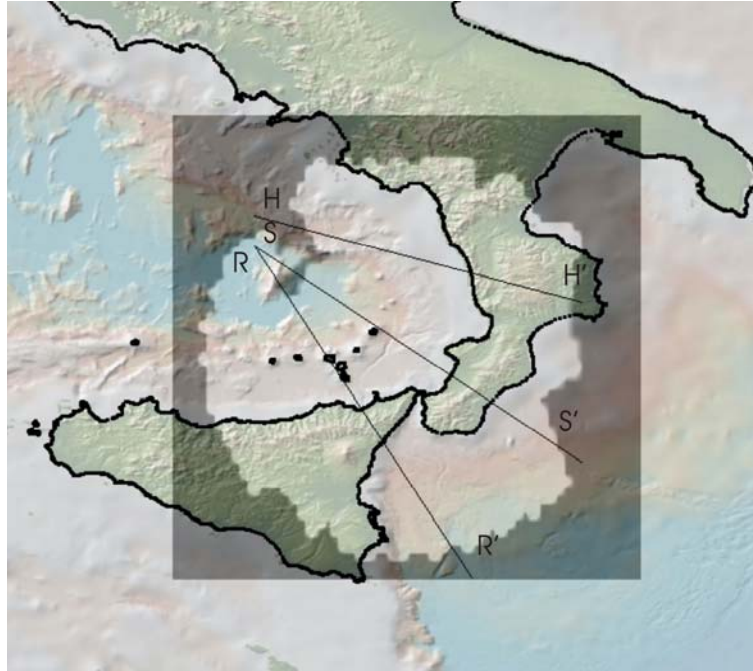


Fig. 5.3.1 – Map showing the covered area of the Vs WAM with DWS >100 (white area inside the grey one), and the three vertical profiles (R-R', S-S' and H-H').

We assessed the reliability of the Vs distribution of WAM again, analyzing its standard deviation distribution. The values of the standard deviations of the Vs WAM does not exceed 0.09 km/s (excluding a border spot on the section S-S' where reaches up to 0.12 km/s), ensuring the absence of strong bias and supporting the existence of the anomalous bodies displayed.

The vertical sections through the WAM (S-S', H-H' and R-R' displayed in the figures 5.3.2, 5.3.3, and 5.3.4, respectively) show a high velocity body ($4.7 < V_s < 5$ km/s, marked with the number 1 in all the sections) that is continuous in the section S-S' and interrupted in the sections H-H' and R-R' (area with number 2 in figure 5.3.3 and 5.3.4) as likewise revealed in the Vp WAM. The interruptions of the slab are, between 110-180 km in section H-H', and between 80-120 km in section R-R', as also highlighted in the Vp WAM.

Section S-S' shows, according to the Vp WAM, low velocity bodies (marked with the numbers 2) having values $3.8 < V_s < 4.2$ km/s just below the high velocity subducting slab (1) and a body beneath the Marsili basin (4). It is worth noting that in this section there are low velocity anomalies present (3) on the top of the Wadati-Benioff plane (depicted by the hypocenters projected on the section) that are not clearly picked up on the Vp WAM. These bodies dip coherently with the Ionian lithosphere but they seem just outside from the subducting slab.

The low Vs bodies just aside the slab are rather visible in the profile of H-H' (3), while in R-R' only a large low Vs area seems noticeable (2) located at a depth of 100 km that crosses the whole section in N-S direction

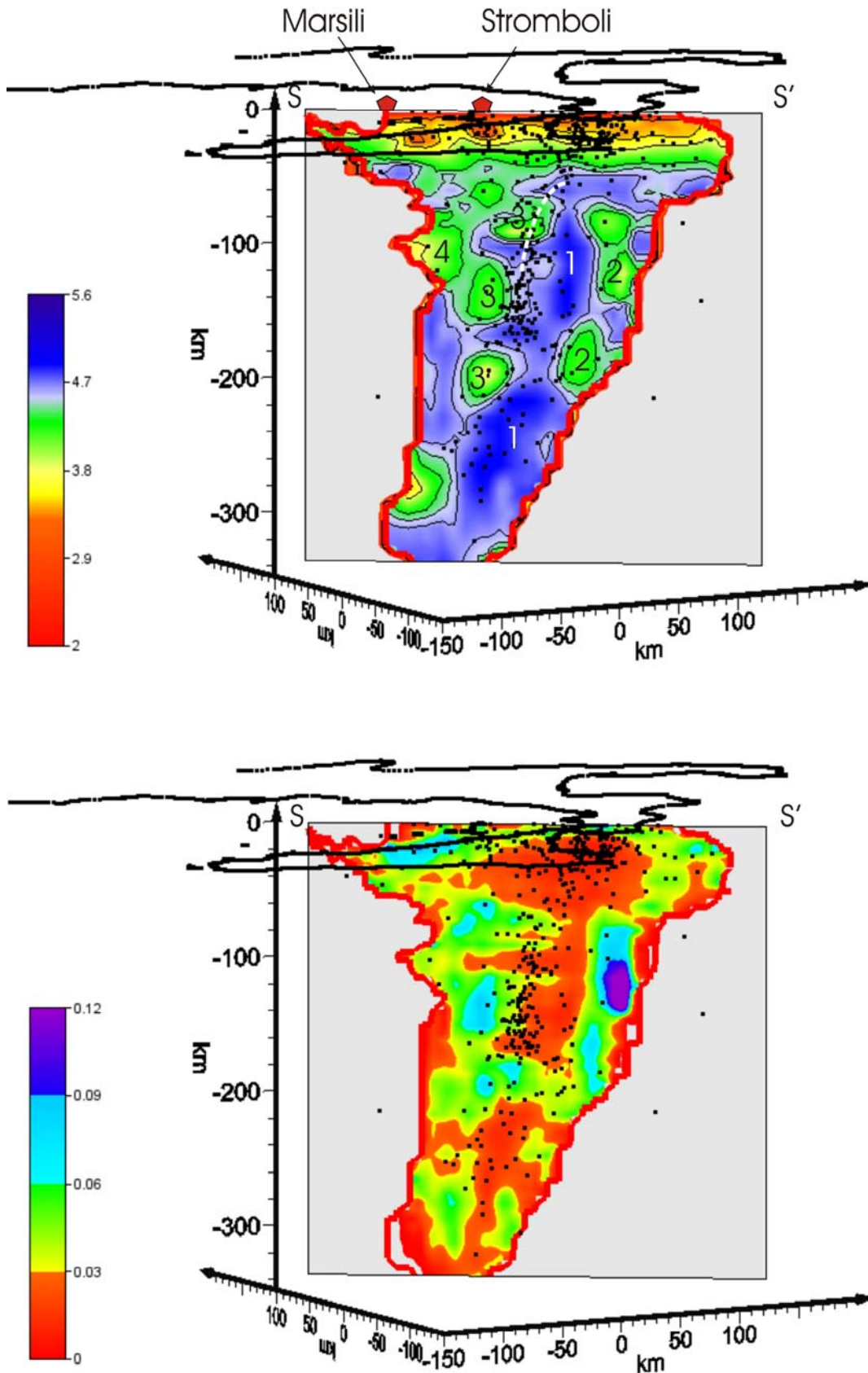


Fig. 5.3.2 -S-S' Vs WAM (top) and corresponding distribution of the standard deviation (bottom). Earthquakes within 15 km of the sections are also plotted. The best resolved area ($DWS > 100$) lies above the red line. The white dashed line in the Vs model is the trace of the NVR interpretative section (Finetti, 2005). The body marked with the number 1 represent the high velocity portion of the subducting slab, the bodies with the numbers 2, 3 and 4 are low areas within and outside the Ionian lithosphere

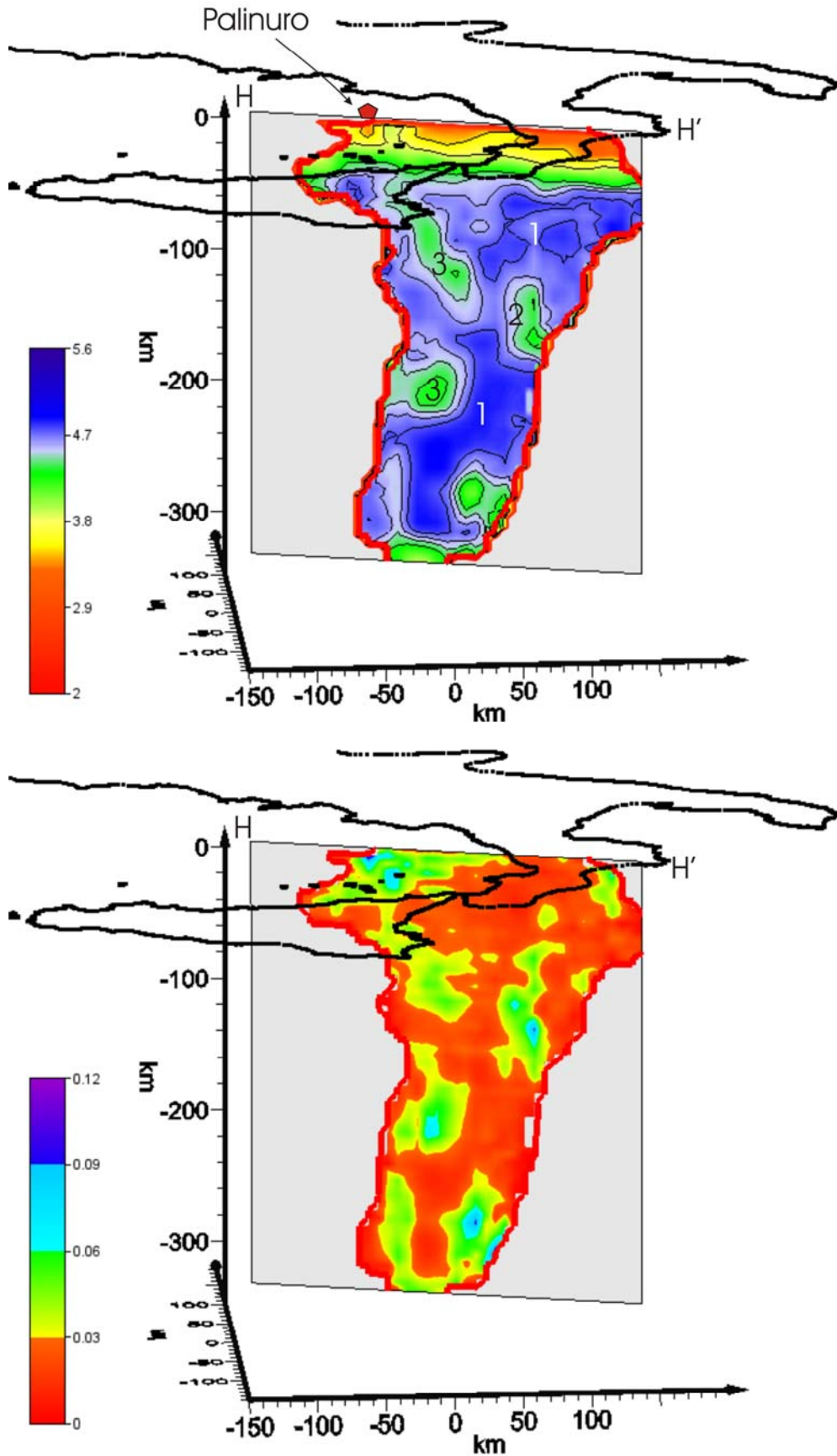


Fig. 5.3.3 –H-H' Vs WAM (top) and corresponding distribution of the standard deviation (bottom). The best resolved area ($DWS > 100$) lies above the red line. The bodies marked with the number 1 represent the high velocity portion of the subducting slab, the bodies with the numbers 2 and 3 are low areas within and outside the Ionian lithosphere.

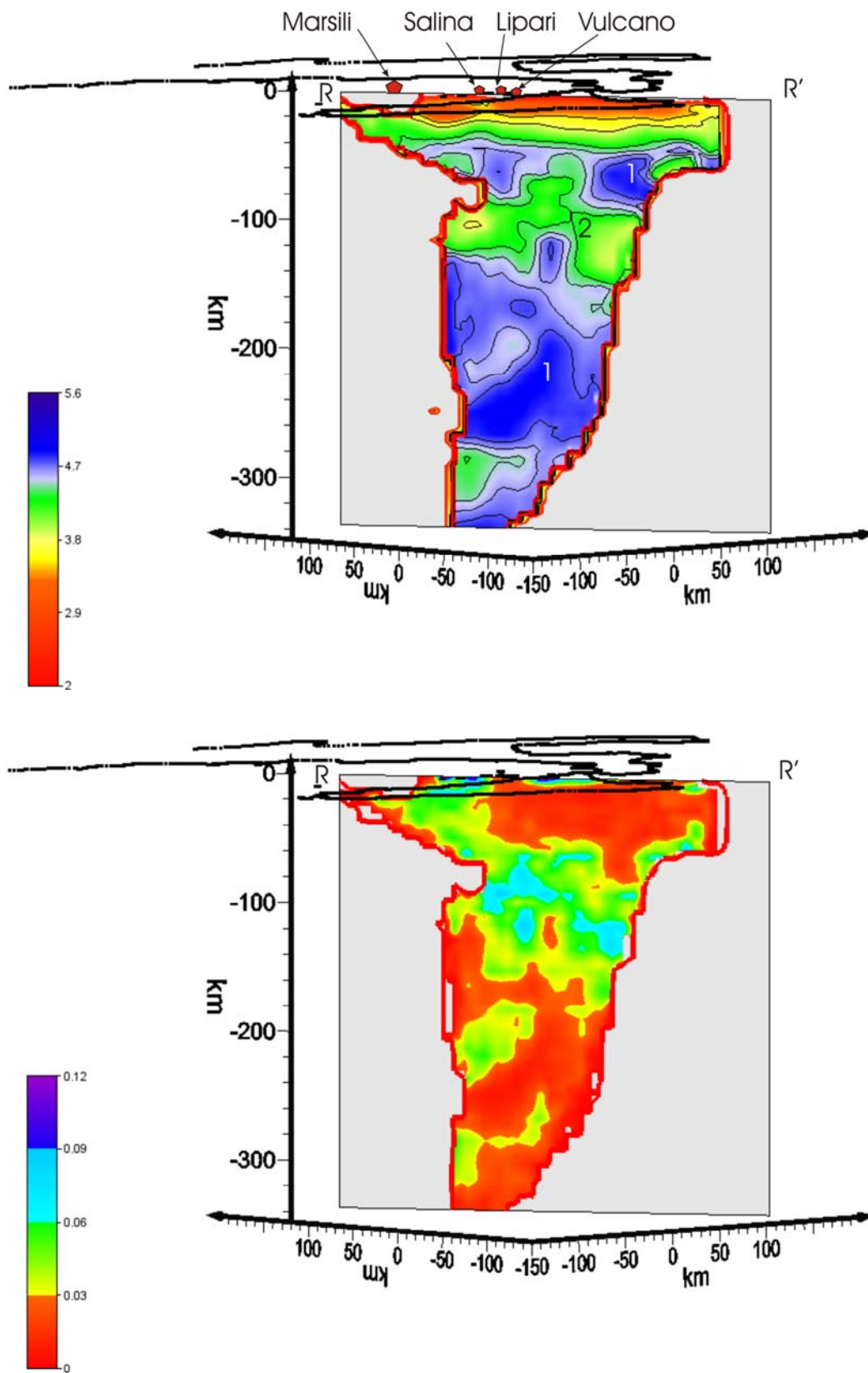


Fig. 5.3.4 $-R-R'$ Vs WAM (top) and corresponding distribution of the standard deviation (bottom). The best resolved area ($DWS > 100$) lies above the red line. The bodies marked with the number 1 represent the high velocity portion of the subducting slab, the body with the number 2 is a low area crossing the section at a depth of 100 km.

The 3-D view of the high velocity portion of the slab redraws similar features to that recovered in the Vp WAM, even if the *hourglass* shape is less evident. Nevertheless, this high Vs body almost completely contains the deep hypocenters, though they are concentrated in its upper portion, following the same direction of immersion, as well as has been depicted by the Vp slab.

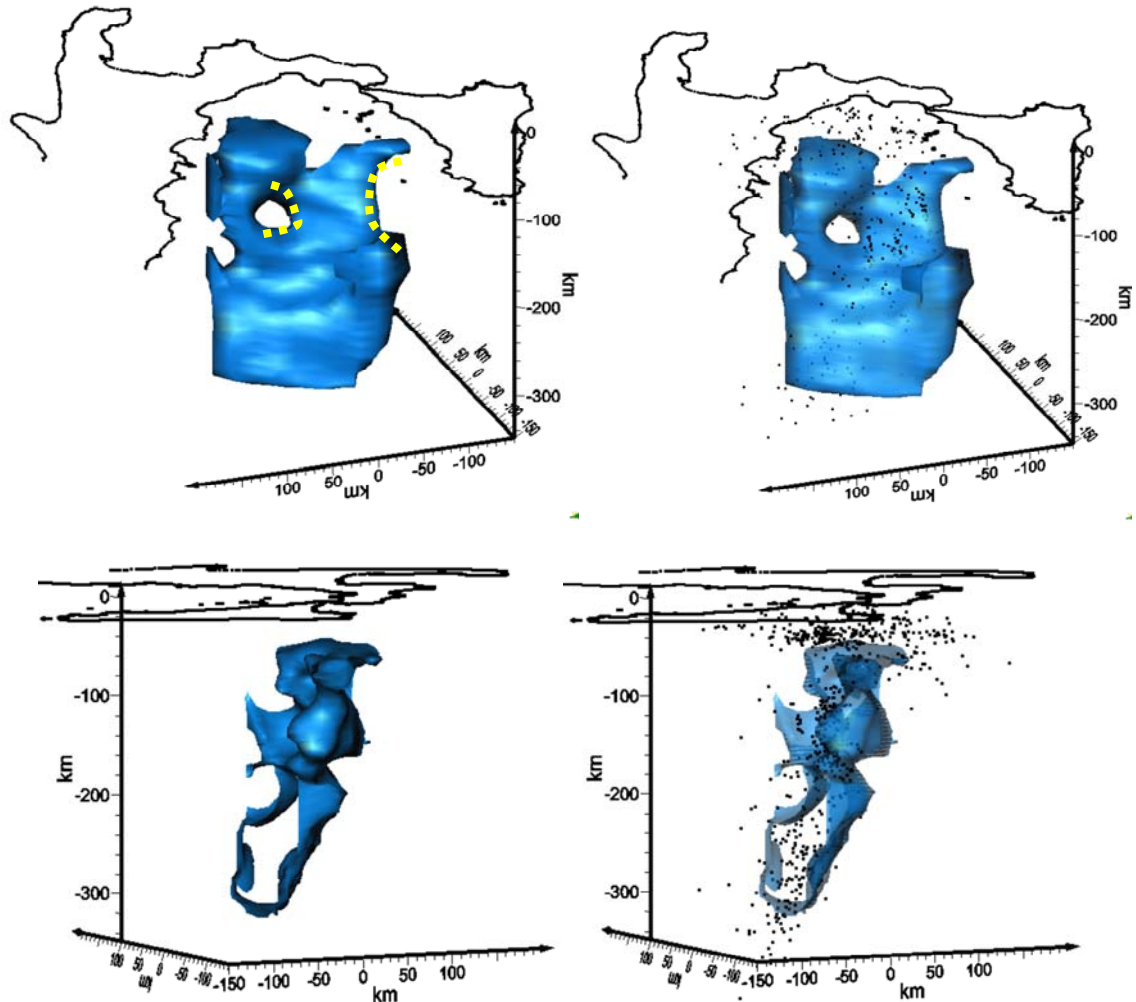


Fig. 5.3.5 – View of the 3-D Vs WAM. The isosurface encloses the volume of the Ionian slab with velocity greater than 4.7 km/s (left top and bottom). On the right the same surface is plotted together with the deep hypocenters relative to the events selected to realize the Vs model. It is clearly visible how the hypocenters are well contained in the volume delimited by the isosurface at 4.7 km/s.

5.4 Vp/Vs WAM. Deep Structures.

To have more information on the deep structures of the southern Tyrrhenian sea, we also carried out the Vp/Vs WAM. We determined the model dividing directly the Vp WAM by the Vs one. This practice increases the errors contained in the model producing, inevitably, a Vp/Vs distribution less reliable than the direct construction of the Vp/Vs model. For this reason we will discuss only some major traits of the Vp/Vs model leaving aside features that could be affected by strong distortions. The section S-S' (figure 5.4.1) shows two large regions, mostly located in the Tyrrhenian mantle, characterized by high Vp/Vs (> 1.85). Section H-H' (figure 5.4.2) does not show peculiarities (only a low Vp/Vs area (< 1.7) located beneath the Tyrrhenian basin), while R-R' highlights the presence of two bodies characterized by high values of the ratio. The first one (1) has an elongated shape in N-S direction at a depth of 100-120 km while, the second one (2) is located below the Marsili basin reaching a depth of 40-50 km (figure 5.4.3).

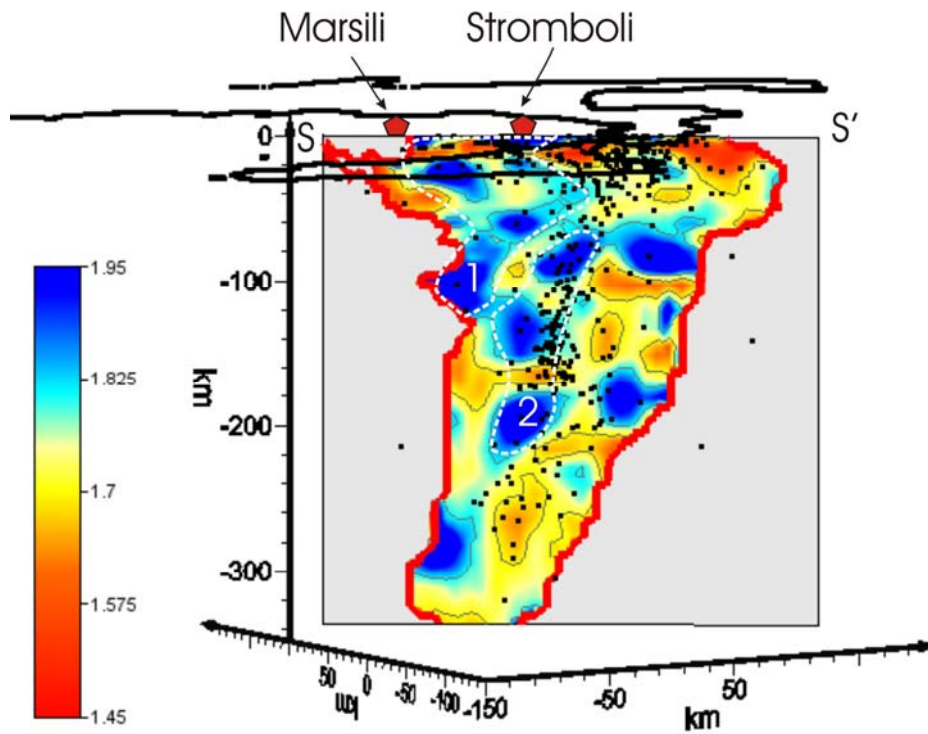


Fig. 5.4.1 – S-S' V_p/V_s WAM. Earthquakes within 15 km of the sections are also plotted. The best resolved area ($DWS > 100$) lies above the red line. The white dashed lines enclose two areas characterized by high values of the ratio.

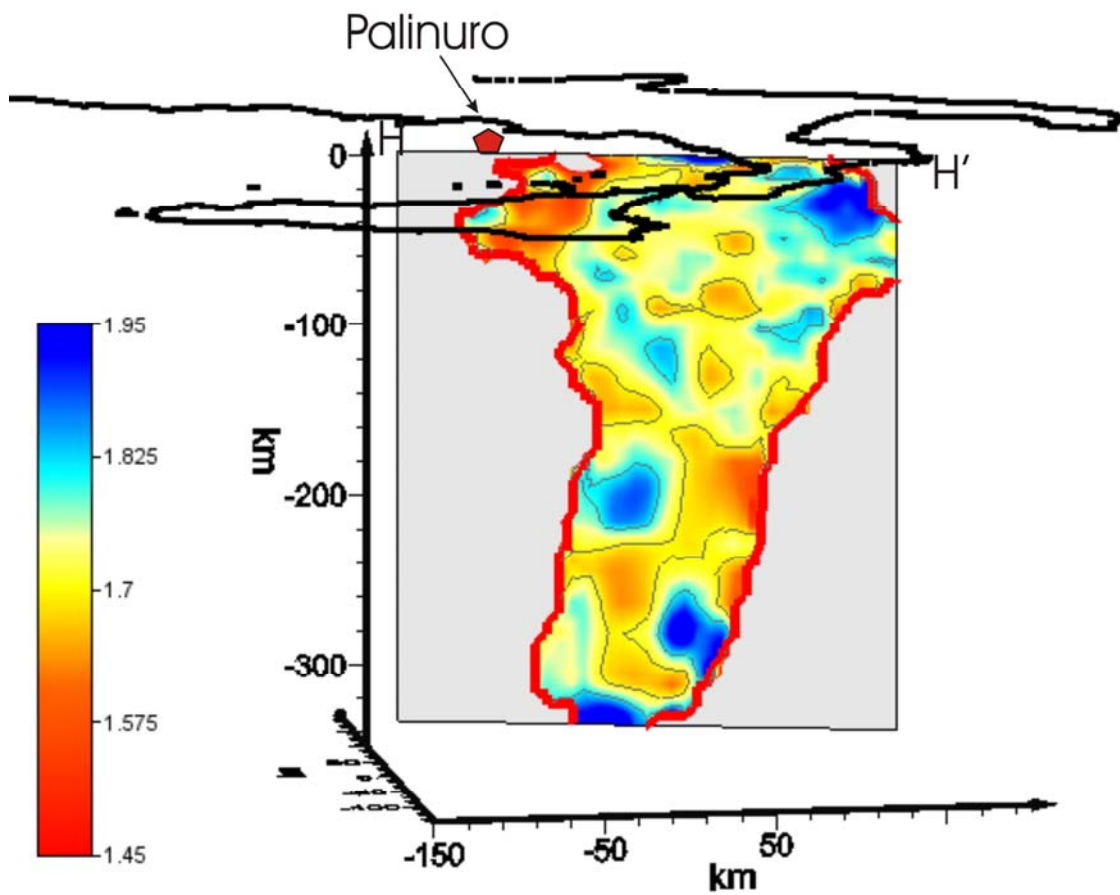


Fig. 5.4.2 – H-H' V_p/V_s WAM. The best resolved area ($DWS > 100$) lies above the red line.

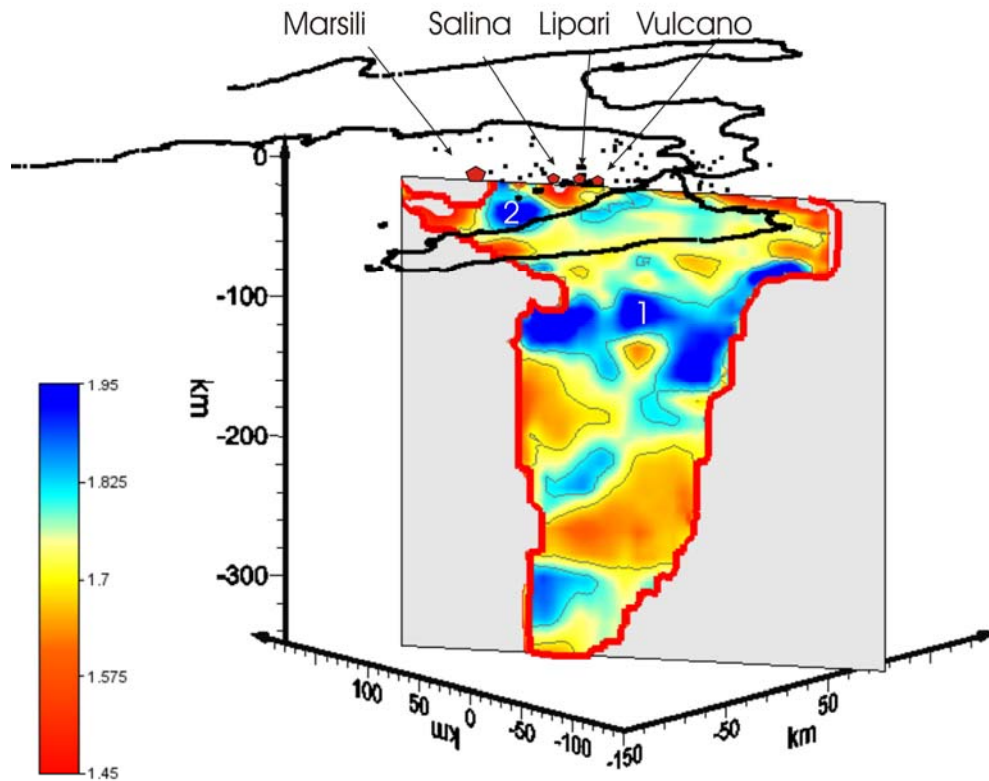


Fig. 5.4.3 – R-R' Vp/Vs WAM. The best resolved area ($DWS > 100$) lies above the red line. The numbers indicate two areas characterized by high values of the ratio.

5.5 Vp and Vs WAM. 'Shallow' Structures.

In this section we will discuss the main features of the shallow structures (less than 80 km of depth) of the southern Tyrrhenian sea region. The high reliability of the Vp and Vs WAM permitted us to obtain velocity distributions having a resolution able to describe both the deep geometric elements and the shallow ones. We chose the same profiles traced for the description of the deep structures because they are representatives of the studied area and to better show some features previously not sufficiently discussed.

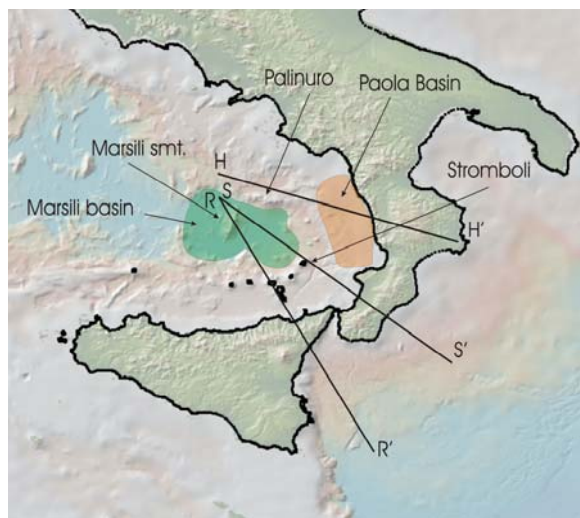


Fig. 5.5.1 – Map showing the three vertical profiles (R-R', S-S' and H-H') carried out to describe the main features of the southern Tyrrhenian region. In the map the Paola sedimentary basin and the Marsili oceanic basin are also reported.

Section H-H' brushing the Palinuro seamount crosses the wide Paola sedimentary basin and the Calabria in its northern part. The Vp and Vs sections along this profile (figure 5.5.2) show coherently low velocities beneath the Calabrian mountains down to 20 km, in the Vp model, and 30-35 km in the Vs one, which is a clear expression of the chain root. Low velocities are also recovered beneath the Paola basin down to 15-18 km that can be assigned to the upper crust and to the thick plio-quaternary sedimentary cover (Pepe et al, 2008). In the Vp section, low velocities beneath the Palinuro seamount give evidence of the anomalously high thermal conditions around this area.

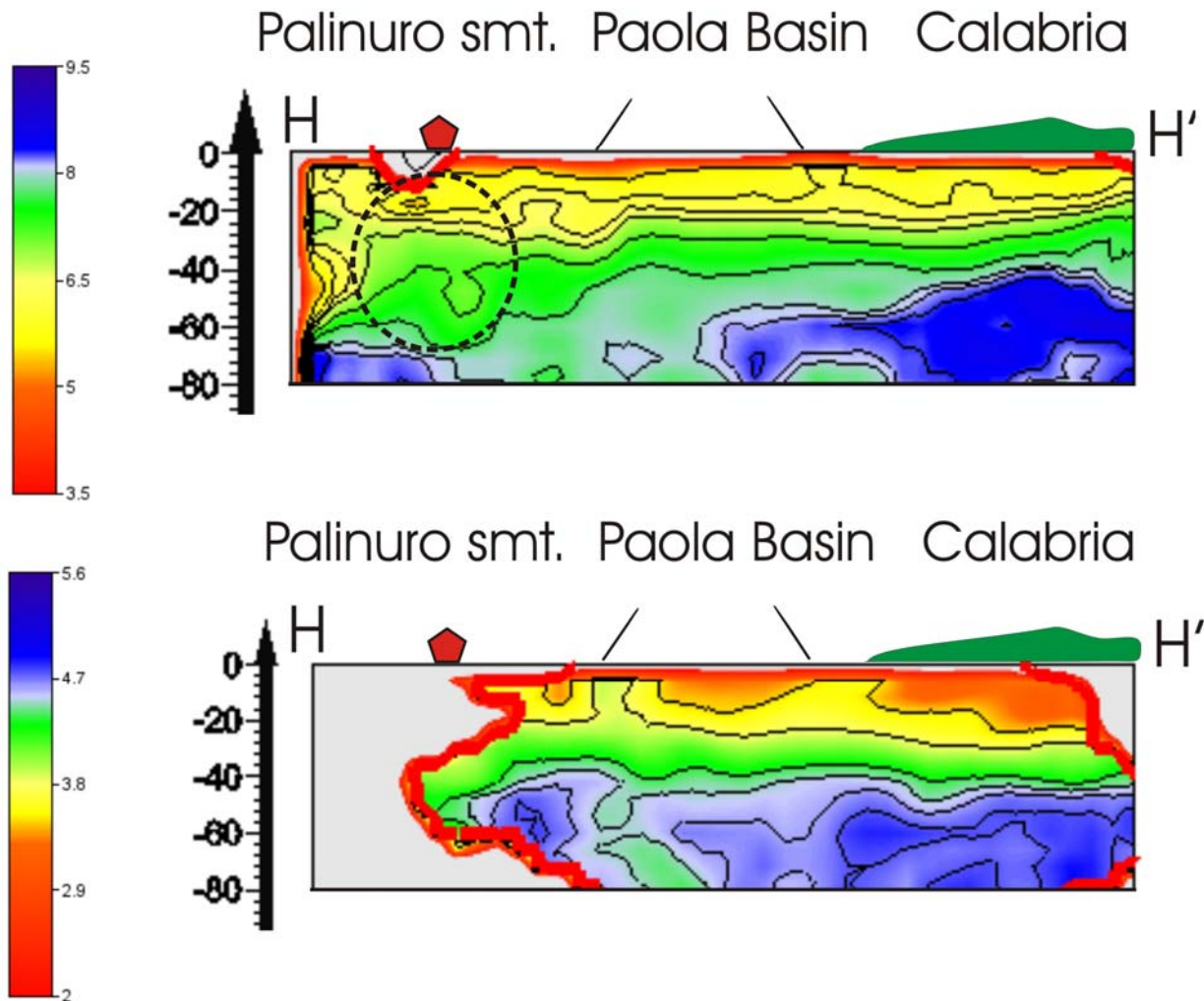


Fig. 5.5.2 – H-H' vertical section of the Vp WAM (top) and of the Vs one (bottom). The black dashed circle contains the low Vp area beneath the Palinuro seamount.

Section S-S' crosses Marsili seamount in its northern part and traversing the Marsili oceanic basin and the Stromboli volcano, intersects the southern part of Calabria. Shallow low velocities below Stromboli are marked in both Vp and Vs models (between 10 and 18 km of depth) showing the probable location of a magma accumulation region beneath the volcano (figure 5.5.3). Low velocities between the Stromboli and Marsili seamount (poorly evidenced in the Vp model while strongly represented in the Vs one) suggest the anomalous thermal state of the oceanic Marsili basin. Finally, a wide lithospheric (down to 40-50 km of depth) low velocity body only resolved in the Vp section is displayed beneath

the Marsili seamount, which suggests a large accumulation of molten magma. Furthermore, beneath the west-margin of Calabria a crustal thinning toward the Marsili basin is clearly visible.

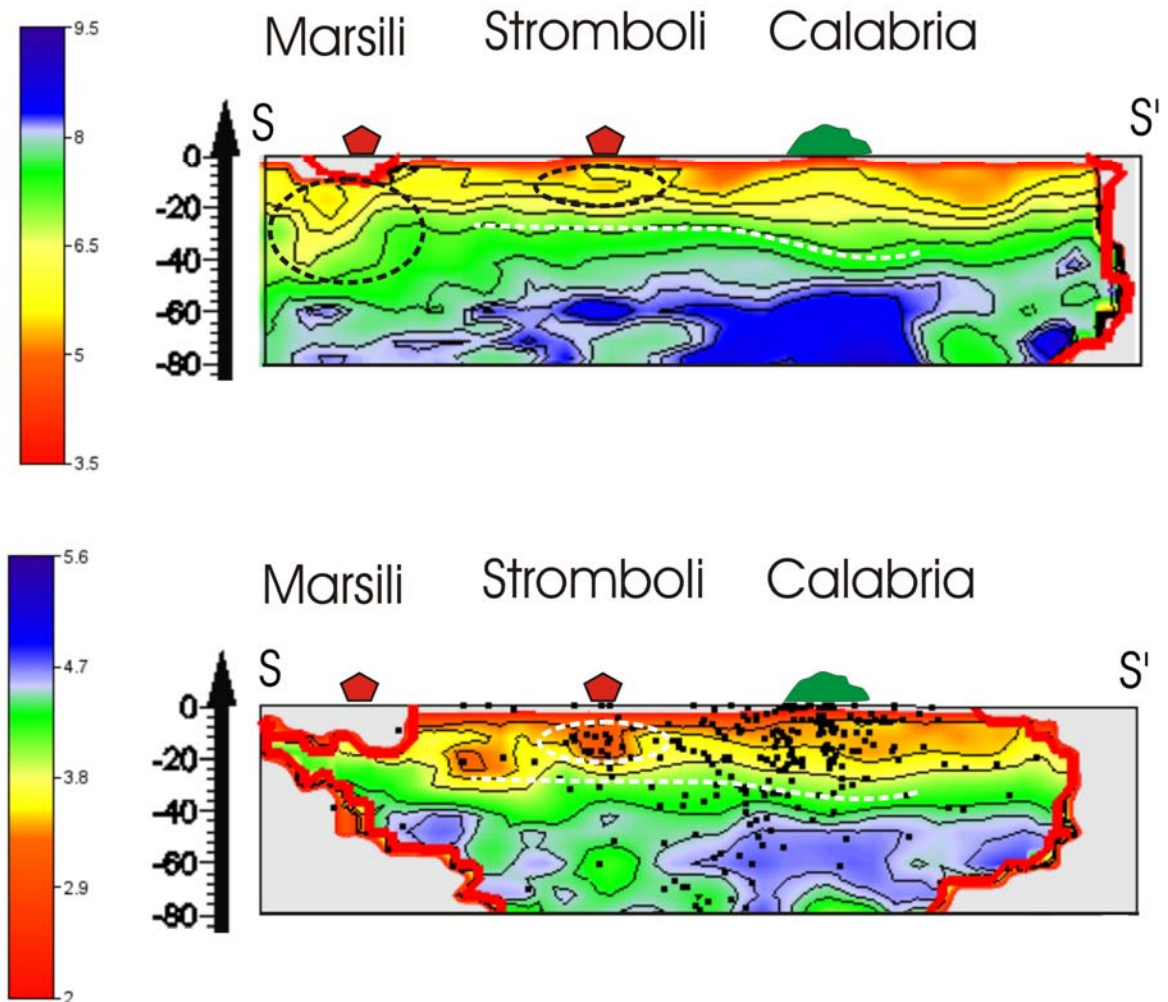


Fig. 5.5.3 – S-S' vertical section of the Vp WAM (top) and of the Vs one (bottom). The black dashed circle contains the low Vp area beneath the Marsili seamount and Stromboli, while in the Vs section the with dashed circle includes only the low Vs body beneath the Stromboli. The white dashed line highlights in both models the crustal thinning of the Tyrrhenian domain.

The profile R-R' starts from the Marsili seamount, crosses three Aeolian islands (Vulcano, Lipari and Salina), the eastern part of the Sicily, and ends on the Ionian sea.

The Vp and Vs sections both show the crustal thinning starting from the Maghrebain chain toward the Tyrrhenian sea (figure 5.5.4). In fact the crustal thickness decreases from 35-38 km below the Sicily to 20-22 km beneath the Marsili basin. In the Vp model it is visible a low velocity zone beneath the Aeolian archipelago (down to 10-12 km), while, the Vs model shows a large low Vs area beneath the Marsili basin reaching a depth of 20 km. Low velocities are again recovered in the Vp section, beneath the Marsili seamount.

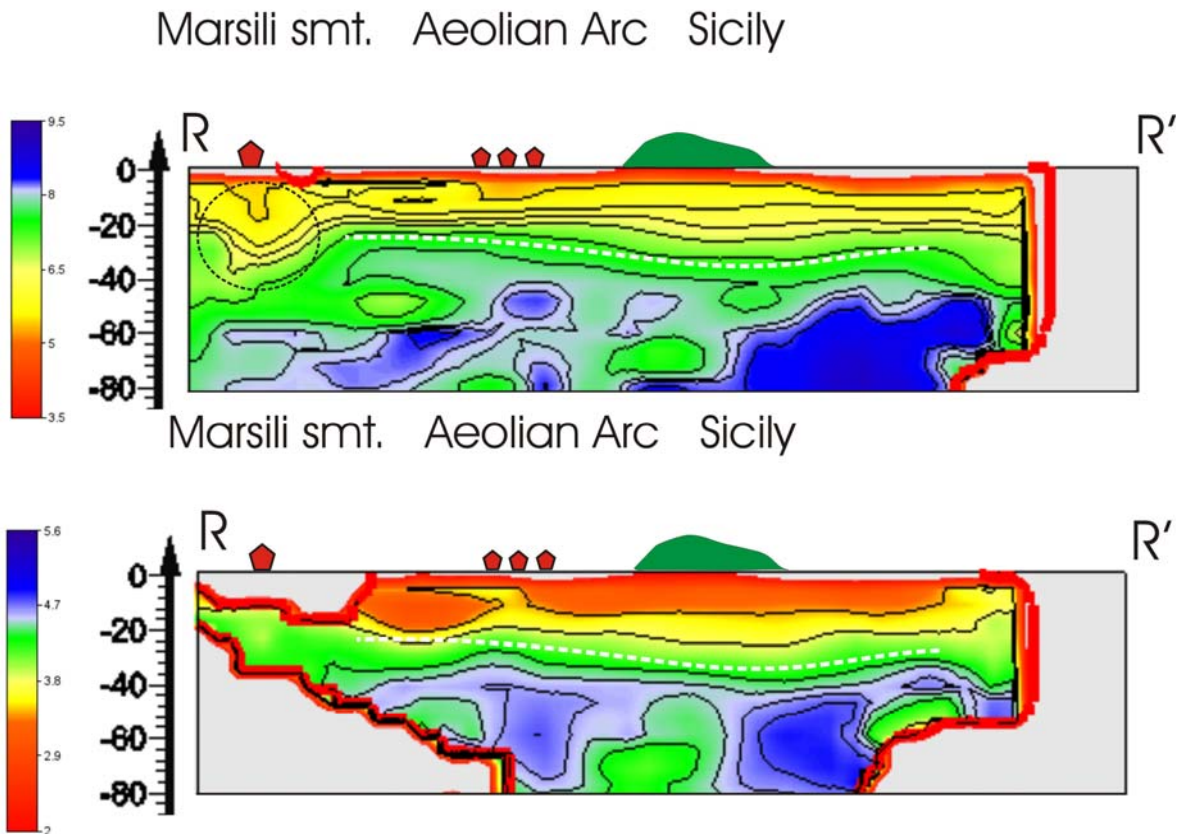


Fig. 5.5.4 – R-R' vertical section of the Vp WAM (top) and of the Vs one (bottom). The black dashed circle contains the low Vp area beneath the Marsili seamount. The white dashed line highlights in the both models the crustal thinning of the Tyrrhenian domain.

5.6 Conclusions

In this chapter we discussed the main geometric features of the deep and shallow velocity structures beneath the southern Tyrrhenian sea. Thanks to the WAM method we were able to assess the reliability of these bodies by giving important insights on their shape, relative position and depth. We showed for the first time the absolute Vp and Vs velocity distributions of the southern Tyrrhenian region down to 350 km depth by producing original models with high resolution and reliability.

The shape of the top of the Ionian slab, for the first 350 km shows, beside its well known concavity in N-W direction, an *asymmetric hourglass* shape and a dip 69° - 72° toward N-W. This geometry is well depicted by both the Vp and Vs WAMs, though less clearly by the latter. Underlying the high velocity portion of the slab are visible low Vp and Vs bodies reaching a maximum depth of 230-250 km. Finally, in the Tyrrhenian mantle we showed several low Vp and Vs bodies down to 180 km of depth.

The shallow structures (less than 80 km), coming from the same Vp and Vs WAMs used to describe the deep structures, depicted low velocity zones beneath the major volcanoes present in the area (Marsili, Stromboli and Palinuro). The models showed the crustal thinning of the Tyrrhenian domain and the influence of wide sedimentary basins (such as the Paola basin) and of the oceanic ones (such as the Marsili oceanic basin).

6. Petrological Inferences on the Ionian Slab Structure and Geodynamical Modelling

6.1 Introduction

Subduction zones transport water into the Earth's interior. The subsequent release of this water through dehydration reactions may trigger intraslab earthquakes and arc volcanism, regulate slip on the plate interface, control plate buoyancy, and regulate the long-term budget of water on the planet's surface (e.g., Peacock, 1990). While the seafloor input and arc output of this system can be sampled directly, at least in principle, the transport and release of fluids at depth are mostly investigated through indirect methods such as geodynamic modelling and experimental petrology (e.g., Schmidt and Poli, 1998; Hacker et al., 2003a/b). These studies show that the contribution of subducted water to the volcanic arc is critically dependent on the thermal structure, distribution of hydration, and phase transitions within the down-going plate, none of which is well known.

The resolution of the tomographic results has allowed us to discuss the petrological implications of phase equilibria in the subducted lithospheric (harzburgitic) mantle with reasonable reliability.

6.2 Petrological Constraints for Subducted Lithospheres

The slab of subducted lithosphere differs in temperature, bulk composition and phase assemblages from the surrounding mantle, each of the above mentioned variables may affect seismic wave velocities within the slab. The series of mineralogical transformations in the slab not only affect velocities but also density, and thus the forces driving subduction. The shallowest of these is the so-called gabbro to eclogite transformation. There is about a 15% density increase during this process.

Two distinct phase changes occur with the increasing of the depth in the two different chemical systems:

- the gabbro → eclogite transition, this transformation affects less than 10 % of the whole slab volume, i.e the basaltic crust (the former MORB) of the top portion of the down going slab;
- and olivine transformations in denser phases in the ultramafic portion (harzburgite/peridotite) of the slab, by far the most abundant by volume

With increasing depth, gabbro (olivine+plagioclase+clinopyroxene) converts into eclogite when increasing pressure destabilizes plagioclase and other Al-bearing phases (spinel and then garnet+clinopyroxene) accommodating this element (Ringwood, 1972; Ahrens and Schubert, 1975).

Harzburgite (olivine+orthopyroxene±clinopyroxene) has little aluminum which is a host in clinopyroxene. With increasing depth, both opx and cpx are incorporated into garnet (majorite) and disappear at about 450 km (Bina and Wood, 1984). Meanwhile, olivine undergoes a succession of isochemical phase transformations from α -olivine through β -modified-spinel to γ -spinel (Akimoto and Fujisawa, 1968). These transformations are both pressure and temperature dependent and occur at shallower depths where the slab is cooler (Turcotte and Schubert, 1971), given the positive Clapeyron slope of these subsolidus reactions.

Hydrous phases most likely dominate the elastic and chemical evolution of the slab as it subducts. Hydration and dehydration reactions in the subducted ultramafics, by far the most abundant rock type, have relevant effects on mechanical properties, whole rock-H₂O budget and consequently on P- and S-waves velocities (Hacker et al., 2003).

Serpentinization is the process by which ultramafic minerals transform to serpentine-group minerals (figure 6.2.1). Dehydration of slabs subducting beneath the forearc and water flowing through fractures in an extended forearc can partially serpentinize the mantle wedge causing serpentinite mud diapirs (Oakley et al., 2007) and layered structures (Abers, 2005).

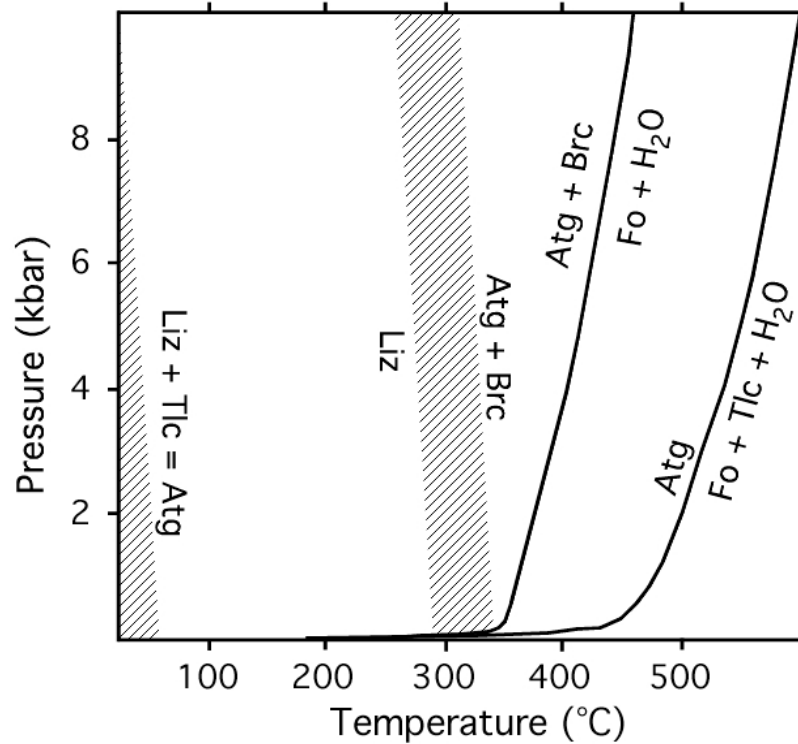


Fig. 6.2.1 – P-T diagram for serpentine-group minerals (modified from Evans, 2004). Shaded areas show uncertainty in location of reactions. Liz = lizardite, Tlc = talc, Atg = antigorite, Brc = Brucite, Fo = Forsterite.

Starting from low-grade blueschist conditions (10–20 km depth) with H₂O contents between 5 and 6 wt% for hydrated oceanic crust, complete dehydration is achieved between 70 and >300 km depth as a function of individual slab geotherms (Schmidt and Poli, 1998). The P-T stability of H₂O- Mg-bearing phases in (hydrous) ultramafic systems is well constrained by experimental phase equilibria (Schmidt and Poli, 1998; Fumagalli and Poli, 2005, Ulmer and Trommsdorff, 1995 and references therein): antigorite (i.e. the high P polymorph of serpentine and also the major H₂O-carrier in the mantle; Ulmer and Trommsdorff, 1995) persists to a maximum pressure of 8 GPa (at 500 °C, figure 6.2.1), while its upper thermal stability is constrained at 600–650 °C (at 5 GPa); chlorite instead breaks down for T > 800 °C. Both phases transform through various reactions to “10 Å-phase” first and, at P > 6 GPa, to “phase-A” (Ulmer and Trommsdorff, 1999; Fumagalli and Poli, 2005), both belonging to the Dense Hydrous Magnesian Silicates (DHMS) group (figure, 6.2.2).

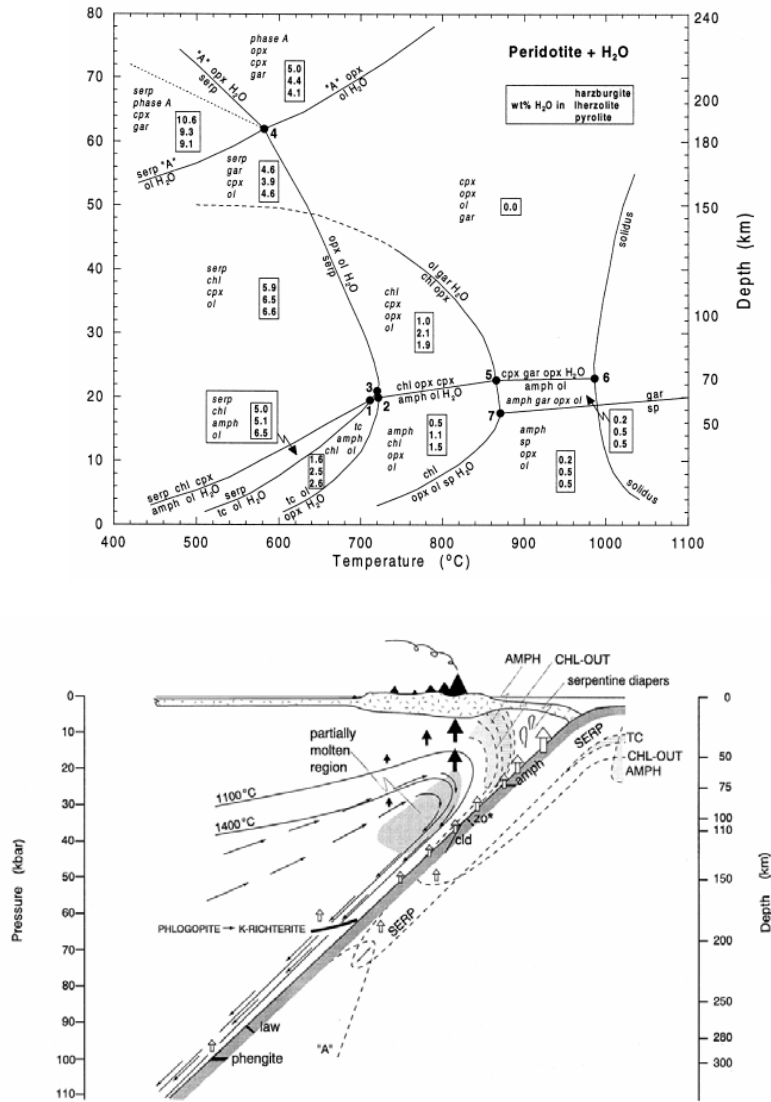


Fig. 6.2.2 – Phase diagram for H₂O-saturated average mantle peridotite and maximum H₂O contents bound in hydrous phases (small boxes) in average peridotites (top) and model for the formation of the volcanic front (bottom). (from Schmidt and Poli, 1998).

The position of the maximum T-P stability limit of serpentine-chlorite at a specific depth into the subducted lithospheric mantle, depends on many variables that affect the thermal regime of the slab (e.g.: slab age, dip angle, rock's thermal conductivity, thermal distribution in the mantle and subduction rate; Iwamori, 2004). As a general rule, the steeper and/or the faster is the slab, the lower is the longitudinal component of the thermal gradient within the slab itself.

As regards to the thermal structure of the subducting Ionian slab (whose estimated age is around 120 Ma, Carminati et al., 2005), thermal and rheological models (Carminati et al., 2005; Pasquale et al., 2005) are in agreement with a rather cold slab (figure 6.2.3). Accordingly, the maximum depth that can be reached by the 600 °C isotherm, which is crucial in the phase equilibria above mentioned, is around 300-350 km, if a conservative value is assumed, where more than 700 km of Mesozoic oceanic Ionian lithosphere have been subducted below the Calabrian arc at rates of about 3 cm/year (Rupke et al., 2004; Carminati et al., 2005).

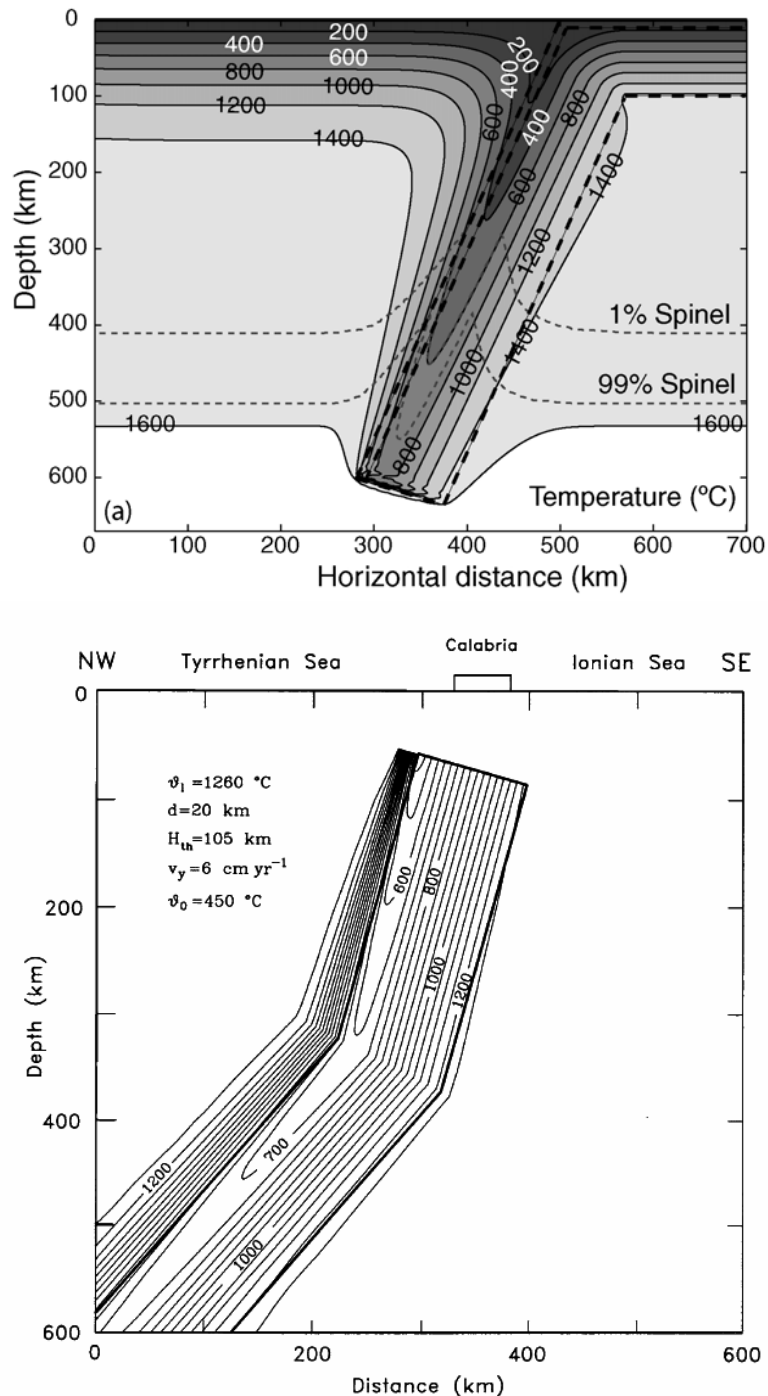


Fig. 6.2.3 – Thermal models for the Ionian slab proposed by Carminati et al. (2005) top, and by Pasquale et al. (2005), bottom.

Furthermore, as shown in figure 6.2.4, the fluids released by dehydration reactions in the ultramafic portion of the slab are not univocally destined to migrate into the overlying mantle wedge (via fault-controlled pathways), but at least for steeply subducting slabs (such as the Ionian) a partial up-dip flow within the subducted slab is to be expected (Abers, 2005).

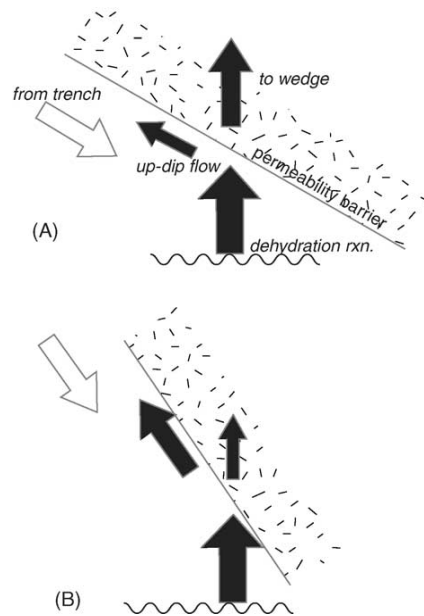


Fig. 6.2.4 – Cartoon illustrating how flow of metamorphic fluids might be affected by slab dip and permeability structure, for: (A) low dips (B) high dips. Greater dips may favor up-dip fluid transport (black arrows), adding fluid beyond that delivered from the trench (open arrow). (from Abers et al., 2005).

If a sufficiently cold and hydrated, the mafic crust is hydrous enough (several wt.% H₂O) to 6 GPa, which would cause seismic velocities to be 5–15% slower than those of the surrounding mantle (e.g., Connolly and Kerrick, 2002; Hacker et al., 2003a). Similarly, serpentinized harzburgite within the descending plate could form a potentially major reservoir for additional fluids (Peacock, 2001; Rupke et al., 2002), and could hydrate the mantle immediately above the downgoing crust (Davies and Stevenson, 1992).

6.3 Discussion

6.3.1 INFERENCES ON THE IONIAN SLAB

The high resolution of the tomography has allowed us to estimate the dimensions of the main velocity structures observed in the Southern Tyrrhenian Sea and, assuming a 125 km total thickness of the Ionian lithosphere (Gvirtzman and Nur, 2001; Pontevivo and Panza, 2006), to propose the following statements along the V_p, V_s and V_p/V_s S-S' section of the WAMs (figures 6.3.1.1, 6.3.1.2 and 6.3.1.3):

- the 50-60 km thick high-velocity body ($8.2 < V_p < 8.8$ km/s and $4.75 < V_s < 5$ km/s) is interpreted as being the upper portion of the descending slab (1), most likely composed of: (i) ~10 km of eclogite, former oceanic crust ($V_p = 8.4 - 8.7$ km/s), and (ii) ~50 km of anhydrous harzburgite ($8.4 < V_p < 8.8$ km/s). The eclogite and the anhydrous harzburgite, having the similar seismic properties at depth, are virtually undistinguishable one from the other (Hacker et al., 2003) in a LET.

- The immediately underlying 20-25 km thick low-velocity bodies ($7.0 < V_p < 7.7$ km/s and $3.8 < V_s < 4.2$ km/s) are instead attributed to a partially hydrated (serpentinized) harzburgite (2). These bodies are coincident with the inner, probably colder, portion of the slab and are separated by faster protrusions, probably corresponding to less hydrous mantle regions. The portion of the slab underlying the low velocity bodies should have a remaining thickness around 40-55 km.

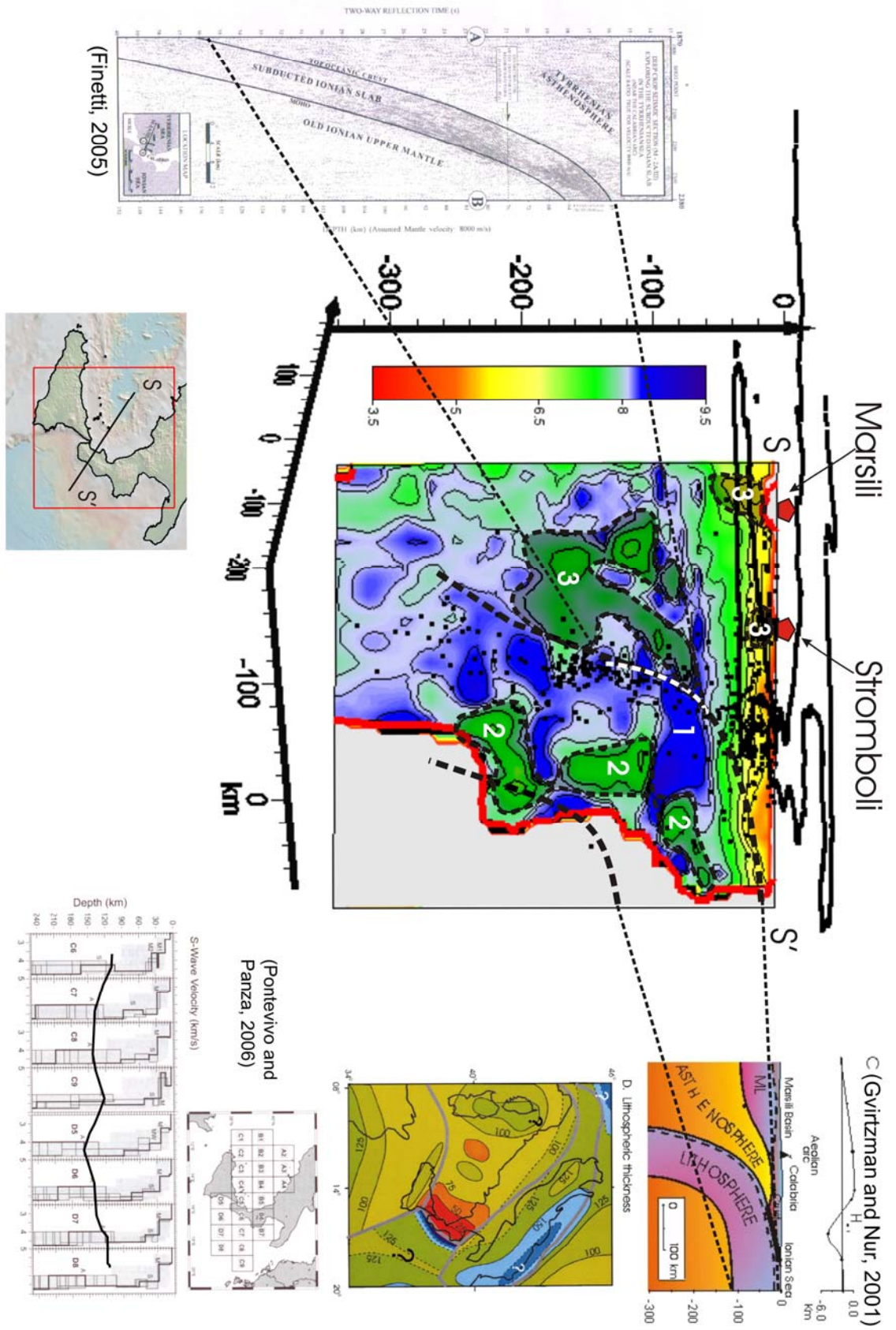


Fig. 6.3.1.1 – S-S' section of Vp WAM constrained with other geophysical studies (Finetti, 2005; Gvirtzman and Nur, 2001; Ponteivivo and Panza, 2006). The spots highlight a low velocity area discussed in the text.

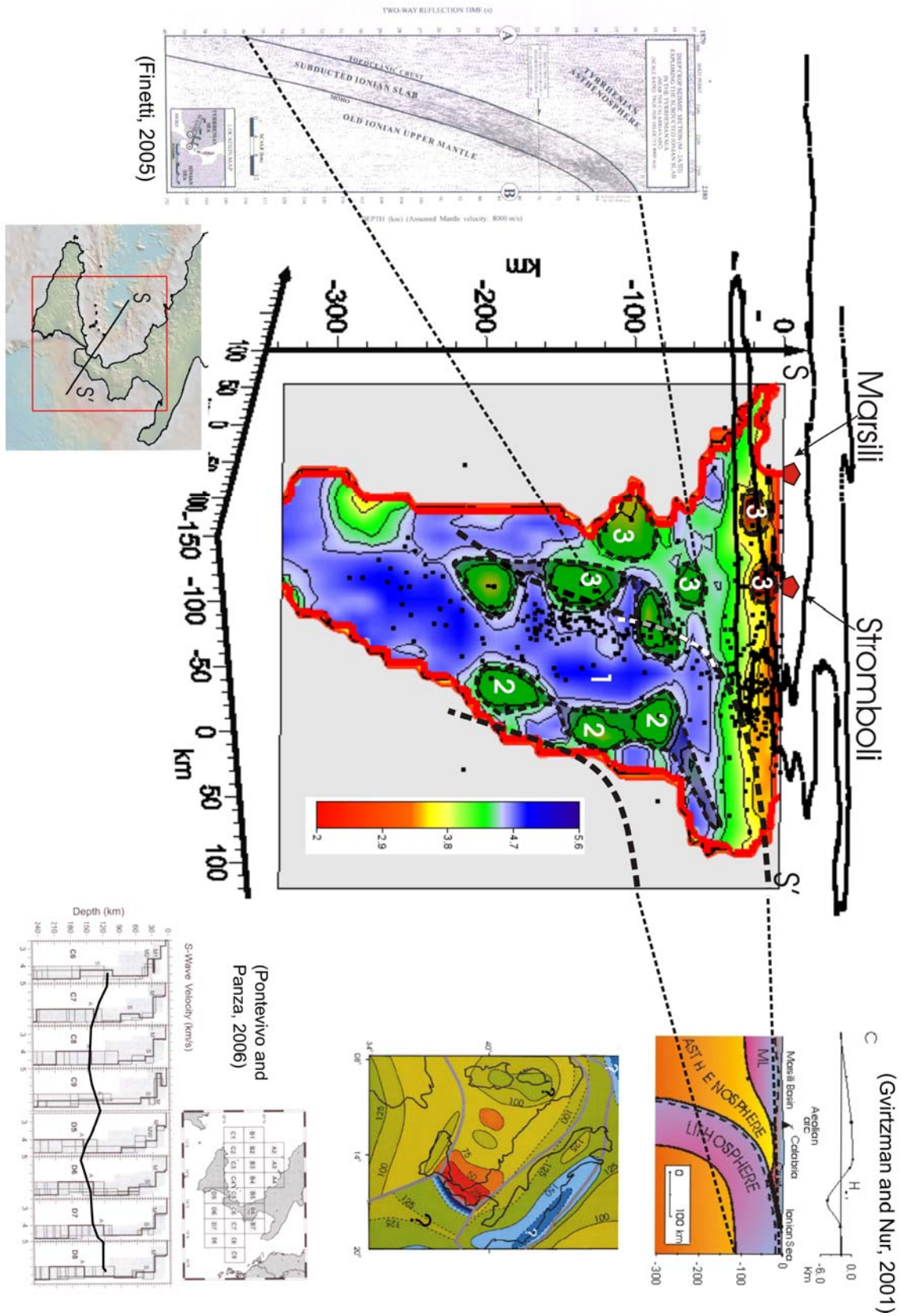


Fig. 6.3.1.2 – S-S' section of Vs WAM constrained with other geophysical studies (Finetti, 2005; Gvrtzman and Nur, 2001; Ponteviso and Panza, 2006). The spots highlight a low velocity area discussed in the text.

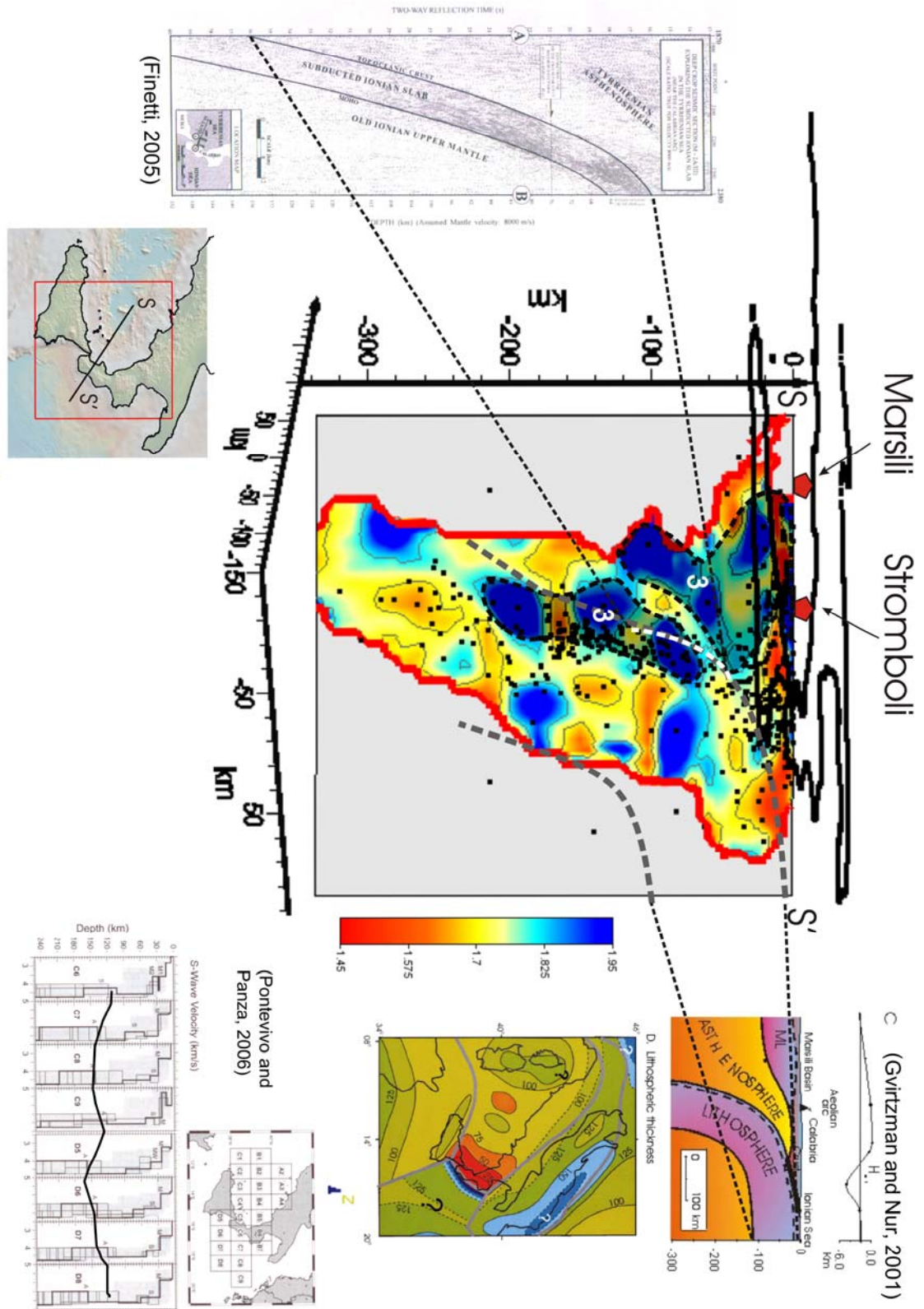


Fig. 6.3.1.3 – S-S' section of Vp/Vs WAM constrained with other geophysical studies (Finetti, 2005; Gvirtzman and Nur, 2001; Ponteivivo and Panza, 2006). The spots highlight a low velocity area discussed in the text.

Serpentinite is in fact characterized by low elastic wave velocities and high Poisson's ratio (Christensen, 2004). The relation between the decrease of V_p with increasing serpentinization in peridotites (Christensen, 2004) suggests that the decrease of V_p down to 7.0 km/s can be achieved with a serpentinization of the peridotite that could reach a 20-30 vol. % . It is worth noting that this low-velocity region is aseismic, in agreement with the ductile rheology of serpentine-bearing rocks (Peacock and Hyndmann, 1999).

Interestingly, the low-velocity bodies disappear at a depth of 230-250 km, that is, close to the experimentally determined maximum pressure stability of antigorite-chlorite assemblages in hydrous peridotites: ca. 6.0 GPa at 600 °C according to Fumagalli and Poli (2005) or even slightly higher P according to Hacker et al (2003).

The vanishing of the low-velocity region at a depth greater than 230 km (figure 6.3.1.4) could thus be ascribed to the dehydration of the serpentine group minerals to H_2O -poor high pressure phases (e.g. the "phase A"). These latter are closely similar to anhydrous lherzolite minerals in their seismic properties (Hacker et al., 2003).

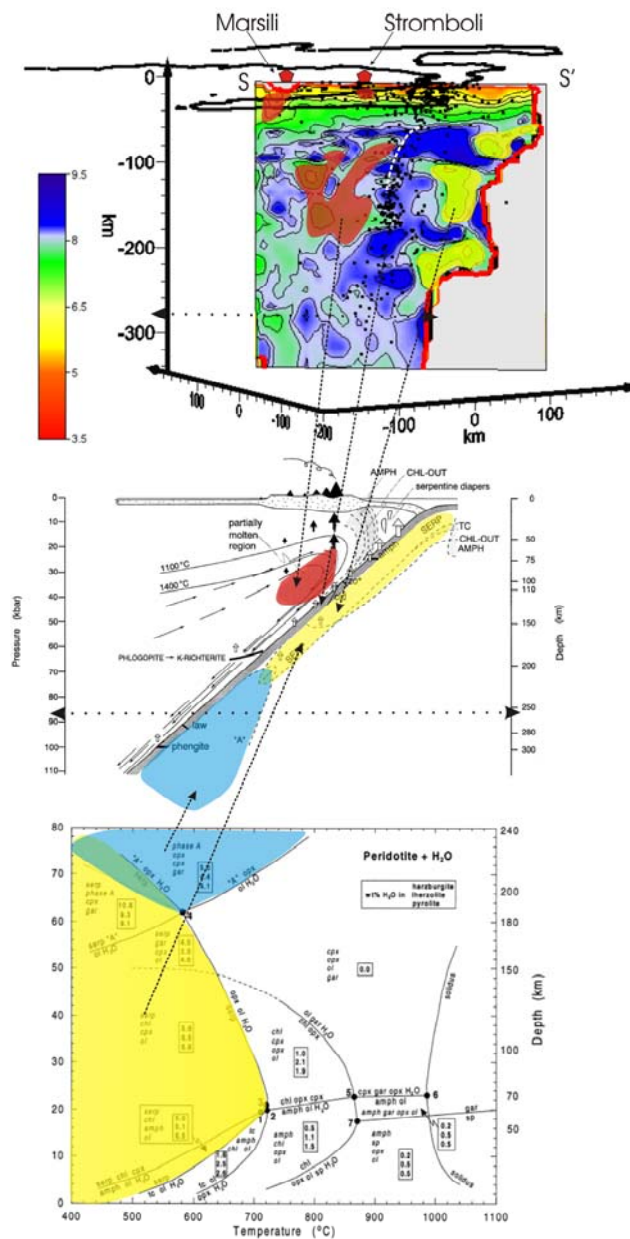


Fig. 6.3.1.4 – S-S' section of V_p WAM on the light of the petrological inferences. (graph and sketch from Schmidt and Poli, 1998).

As regards the structure of the Tyrrhenian mantle wedge (3), our data suggest that partial melting triggered by slab-released fluids is likely to occur at a depth ≤ 180 km, in the large area characterized by low Vp and Vs (figures 6.3.1.1 and 6.3.1.2). This depth is in good agreement with experimental petrology constraints (e.g. Schmidt and Poli, 1998, figure 6.3.1.4) and geochemical/petrological models (Tommasini et al., 2007).

The low-Vp and Vs and high Vp/Vs (3) bodies imaged within the Tyrrhenian lithosphere beneath Stromboli, and less clearly below the Marsili volcanoes (Figures, 6.3.1.1, 6.3.1.2 and 6.3.1.3), argue for the accumulation of significant amounts of mantle partial melts (i.e. some thousands of km³) feeding the present-day volcanic activity.

The sketch in figure 6.3.1.5 summarizes the main features of the velocity models discussed above and illustrates two possible pathways for the fluids released by dehydration of the ultramafic portion of the slab: (i) an up-dip migration (within the subducted ultramafic lithosphere) enhancing hydration of more superficial ultramafics and (ii) through transverse channels, (e.g. bend faults) which deliver fluids to the top of the subducted crust and hence to the overlying mantle wedge.

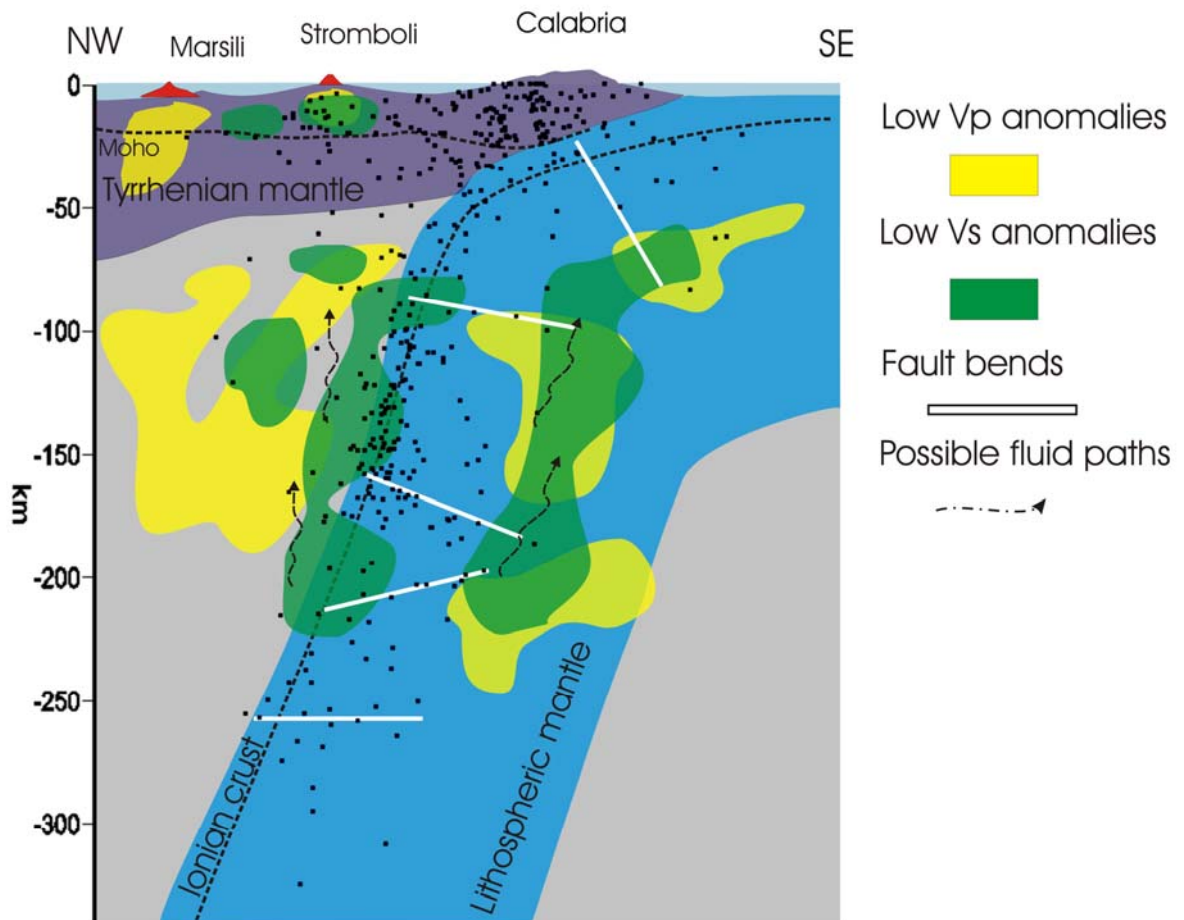


Fig. 6.3.1.5 – Schematic sketch of the Ionian subduction scenario. The yellow and green bodies are relative to the low Vp and low Vs zones, respectively. The possible pathways (black arrows) for fluids released by dehydration of the ultramafic portion of the slab, include an up-dip migration within the subducted ultramafic lithosphere and, through bend faults (white lines), to the top of the subducted and the overlying mantle wedge.

6.3.2 COMPARISON WITH OTHER TOMOGRAPHIC MODELS

Among all the tomographies performed in recent years to study the lithosphere in southern Italy, we prefer to compare our results with three recent models (Piromallo and Morelli, 2003; Montuori et al., 2007; Chiarabba et al., 2008), representatives of the three main techniques used to derive Vp models.

Piromallo (and Morelli, 2003, figure 6.3.2.1a) obtained the tomographic model by using both teleseismic and regional data, Montuori (et al., 2007, figure 6.3.2.1b) inverting only teleseismic data, while the velocity model of Chiarabba (et al., 2008, figure 6.3.2.1c) comes from the inversion of local data.

The models obtained with the first two type of data (Piromallo and Morelli, 2003; Montuori et al., 2007) allowed us to describe the shape of the slab in large scale but with a low resolution (estimated between 0.5° and 1° i.e. 50 - 100 km), not permitting us to discriminate structures within the slab. Furthermore it is commonly accepted that the absolute velocity determined with teleseismic data inversions is not reliable, and to highlight the velocity features it is necessary to display the results in terms of percent anomaly. However, they are very useful to describe the main features of the upper and lower mantle and gives insights into the shape, dip and position of the subducting slab.

Chiarabba (et al., 2008), using only local data and applying the LET technique, is able to recover the absolute velocity distribution and the resolution of its model could be comparable to that of our model. However, the data selected, the parameterization of the volume and the code used (he used Simulps) affect the final results just as we have shown in the previous chapters. Furthermore the model of Chiarabba is resolved only for the upper portion of the Ionian slab not showing its inner structure.

Nevertheless, by comparing the tomographic results of our work with these studies there is a broad agreement regarding the position, the shape and the dimension of the main structures beneath the Southern Tyrrhenian basin, namely, the high velocity portion of the slab (the black ellipses marked with the numbers 1 in figure 6.3.2.1).

The low velocity regions located S-E of the high velocity body in the tomographies of Piromallo and Morelli (2003) and Montuori et al. (2007), being positioned outside the inferred slab volume (2b), are interpreted as lateral flows of hot asthenospheric mantle (Montuori et al., 2007). In the WAM the low velocity regions (2a) occur well within the Ionian lithosphere and consequently must be viewed as being the result of hydration processes affecting the ultramafic portion of the slab.

The low Vp bodies (3) imaged beneath the southern Tyrrhenian basin in all the models have, depth and shape in broad agreement with those depicted in the WAM. Although this part of the Tyrrhenian lithosphere is always recovered as a low velocity zone by all the tomographies, none of them was able to distinguish inner structures to the upper mantle of back arc basin.

However, the WAMs seem clearly more detailed than the models proposed by the recent tomographic studies, allowing a better description of the bodies within the slab and around it.

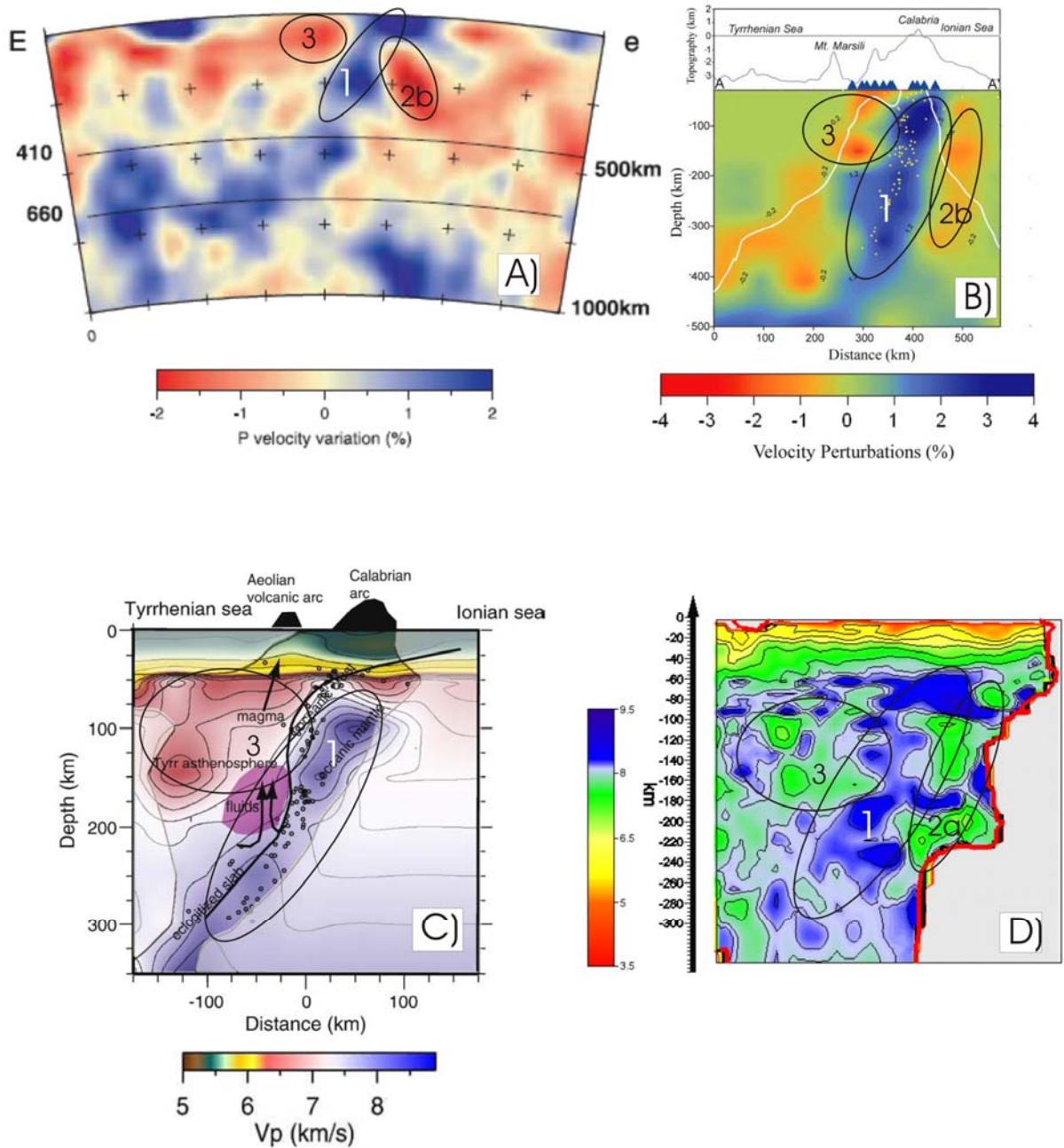


Fig. 6.3.2.1 – S-S' section of Vp WAM (d) compared with others tomographies ; a) Piromallo and Morelli, 2003; b) Montuori et al., 2007; c) Chiarabba et al., 2008).

6.3.3 INFERENCES OF THE WAM TOMOGRAPHY ON THE DYNAMICS OF THE MANTLE FLOW.

The figure 6.3.3.1 shows the probable position of the low Vp bodies throughout the sections H-H', S-S' and R-R when we portrayed the contour of the Ionian lithosphere thus allowing us to realize a 3D sketch of the geodynamic context of the Southern Tyrrhenian region. We must recall that the low velocities that we recovered in the WAMs are interpreted as partially hydrated (serpentinized) harzburgite, while the low velocity regions interpreted by the other works as lateral mantle circulation have to be considered as flows outside the of the Ionian lithosphere.

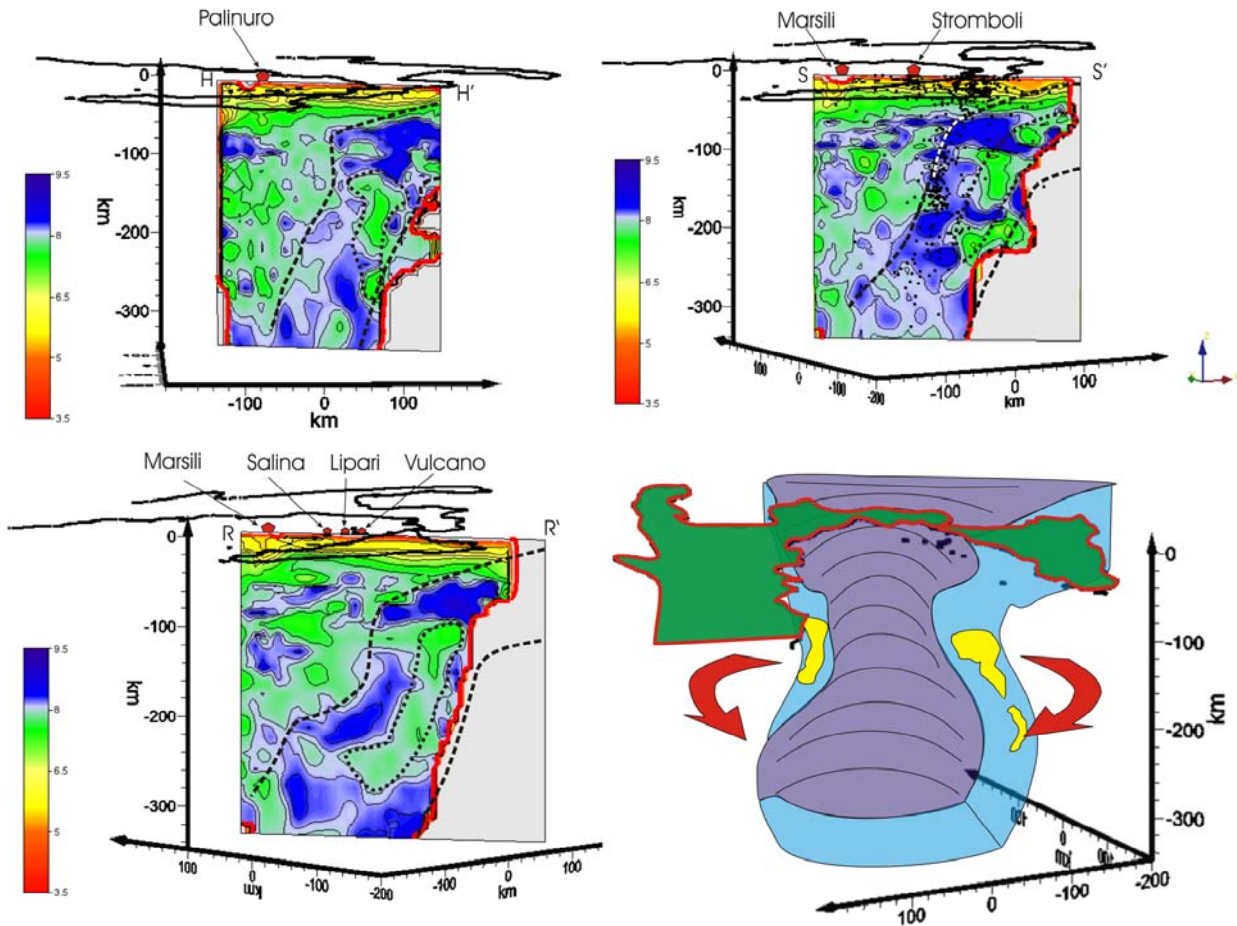


Fig. 6.3.3.1 –Sections H-H', S-S' and R-R' marked the trace of the subducting lithosphere (black dashed lines) and the low Vp bodies within it (black dotted lines). Furthermore it displays the final 3D sketch of the southern Tyrrhenian geodynamic context. The red arrows indicate the possible African mantle flow around the slab (as proposed by Montuori et al., 2007), while the yellow bodies are the low Vp bodies within the Ionian lithosphere.

The very narrow lateral extension of the Ionian slab also has secondary constraints from the geochemistry of recent magmatism of southern Italy. In fact, it is commonly accepted that the 'African' mantle has an isotopic signature enriched in radiogenic lead (HIMU=high- μ , where μ is the $^{238}\text{U}/^{204}\text{Pb}$ ratio) with $^{206}\text{Pb}/^{204}\text{Pb} \geq 19.4$. The HIMU isotopic signature is present in the recent mafic magmatism around Sicily (Ustica, Iblei, Etna, Pantelleria, Sicily Channel, figure 6.3.3.2; Rotolo et al., 2006 and references therein), but disappears in the Alicudi-Vesuvio transect, and appears again at M. Vulture (De Astis et al., 2006). The disappearance of the HIMU isotopic signature in the Aeolian magmatism is thought to be due to the *shield* action of the Ionian slab insulating the mantle source of the Aeolian magmatism from the 'African' mantle (figure 6.3.3.3). Other authors interpreted this feature as a result of a slab window (e.g. Gasperini et al., 2002). The splitting analysis of the SKS phases (Baccheschi et al., 2007) gives insights into a lateral flow of the African mantle around the slab. Doglioni et al. (1999, 2007) suggest that the Tyrrhenian mantle circulation plays a fundamental role on the subduction process and, consequently, on the fore-arc African mantle pushing both the slab and the African mantle toward the east. An intermediate situation where a part of the 'mobilized' mantle migrates

eastward and others mantle flows move around the slab could explain the petrological evidences and the models of the mantle dynamic proposed by Doglioni (figure 6.3.3.3).

However studies on the kinematics of *trenches*, (i.e. of the subduction zones) with respect to both the behaviours of the subducting plate (rheology and kinematics) and the reaction of the mantle, similar to those performed for other subduction zones (Lallemand et al., 2008), could be useful to improve the existing models.

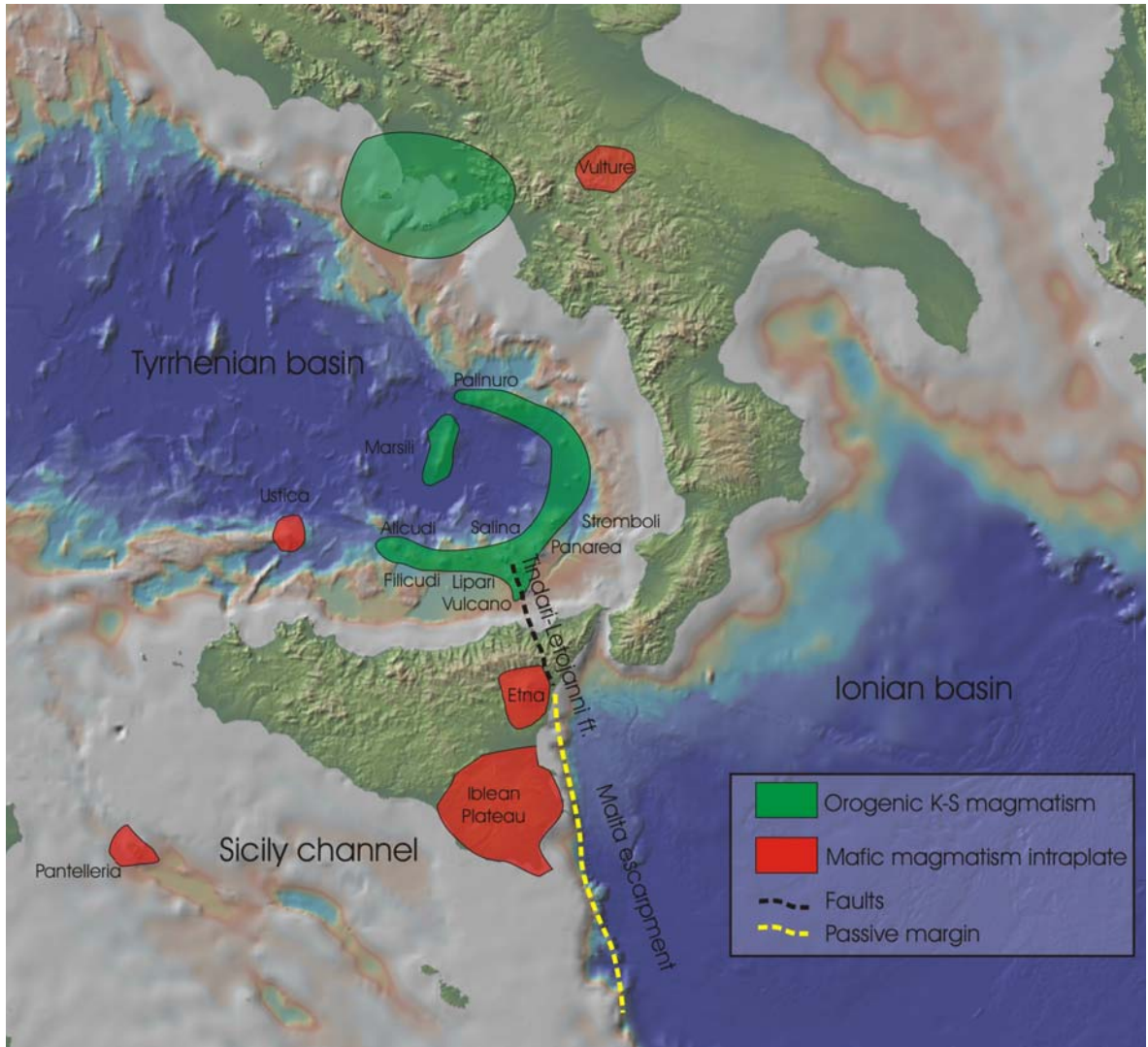


Fig. 6.3.3.2 – Location of the orogenic (green) and the anorogenic (red) magmatism of southern Italy from Oligocene to present. The black dashed line evidences the Tindari-Letojanni fault system and the yellow dashed line the Malta escarpment.

Finally, the spatial coincidence between the west boundary of the Ionian slab and the alignment of the Malta escarpment (topographic expression of the passive margin between the continental part of the African plate and the oceanic Ionian crust), the Etna and the Aeolian volcanoes (Vulcano, Lipari and Salina) suggests that the slab plays a important role, aside the influence on the magmatism of the southern Italy, on the recent lithospheric deformation of the eastern Sicily as the strike slip system Tindari-Letojanni (figures 6.3.3.2 and 6.3.3.4).

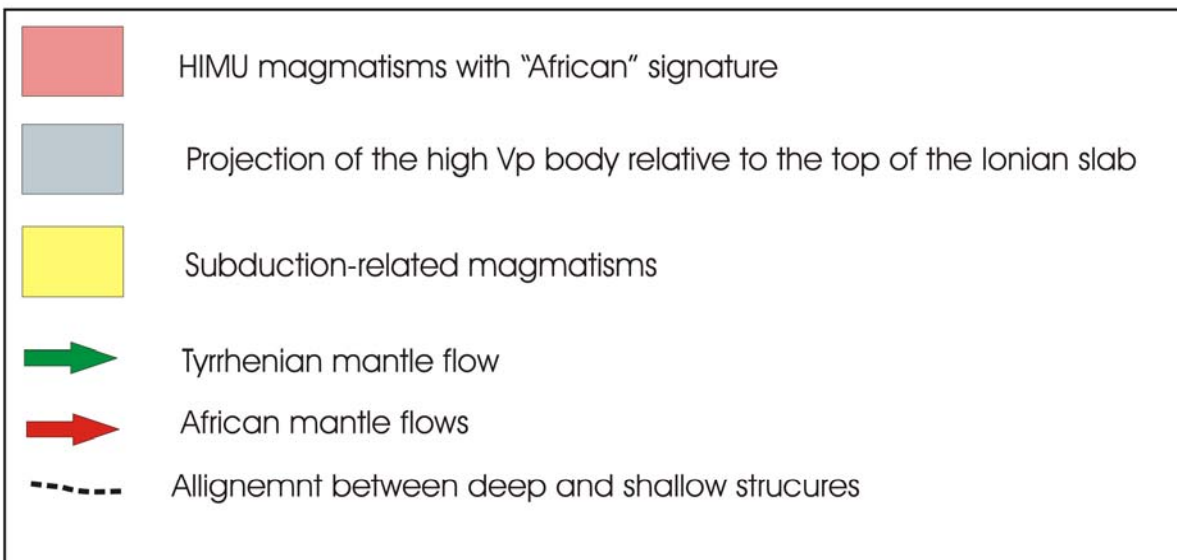
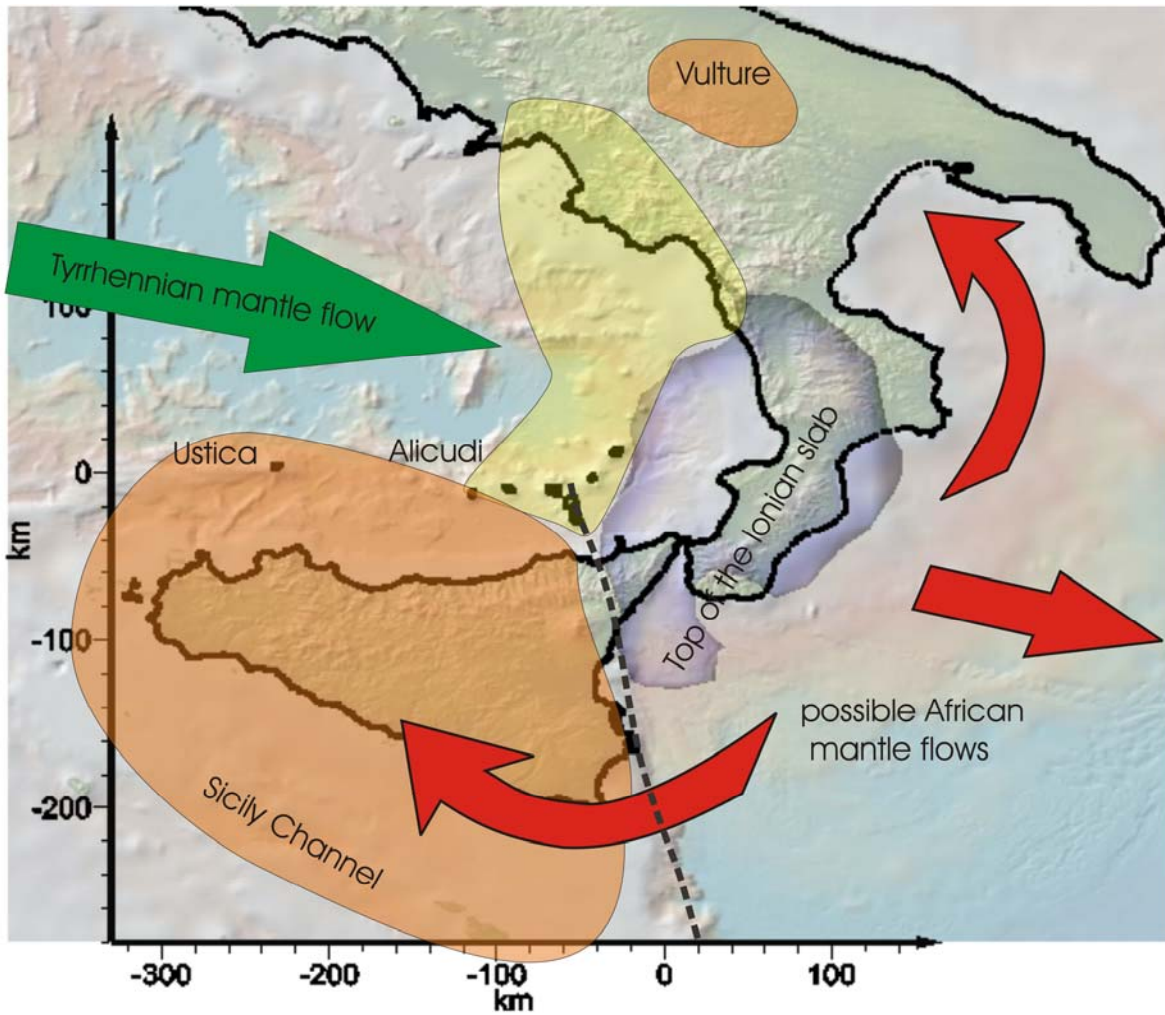


Fig. 6.3.3.3 – Map showing the dynamic of the mantle flows and the spatial coincidence between deep (west boundary of the Ionian slab) and shallow structures (Malta escarpment, Etna, Tindari-letojanni fault and Aeolian archipelago). Some amounts of African mantle can migrate around the slab giving its geochemical fingerprint to the Sicilian region and Vulture magmamentism, while the Aeolian archipelago is shielded from this signature by the Ionian Slab.

7. Prospective

The deep analysis discussed above, however, did not sufficiently describe some important structures of the southern Tyrrhenian Sea. In fact the lack of experimental information does not allow us to clearly illuminate the subducting Ionian lithosphere in its southern part (beneath the Ionian basin, figure 6.3.1.3).

Furthermore, the border areas of the model are characterized by several structures, in particular by some shallow tectonic features that could explain the contact between Europe and Africa with more detail in the Sicilian region. In fact, in the literature there are no seismic velocity models sufficiently reliable and detailed of the hinge zone between the Sicily channel and the Tyrrhenian offshore that are able to describe the complex tectonic structures existing as a result of the pushing of the African plate. These structures are buried for the most part and seismically active, thus playing a fundamental role on the seismicity distribution of the region.

The developed methodology, the WAM method, may be useful to obtain detailed velocity models of volumes adjacent to that already investigated, allowing us to construct a large scale model of the central Mediterranean sea.

In this chapter we will show an example of the ability of the method to realize a large scale WAM. Our first step will be to carry out a high resolution lithospheric WAM of the Sicilian region to better understand the structures characterizing the hinge zone between the African and European.

With this aim we selected a partially overlying area to that of the WAM of the Ionian slab. The earthquakes that have occurred in this region are mostly located at a lithospheric depth. A selection of 1951 events located at a depth between 0 and 80 km is used to perform the tomographic inversions and then the WAM (figure 7.1). The selected earthquakes are recorded by at least 10 stations and marked by weighted RMS less than 0.50 s after the relocation and optimization of the starting 1D model (as shown in the chap. 3).

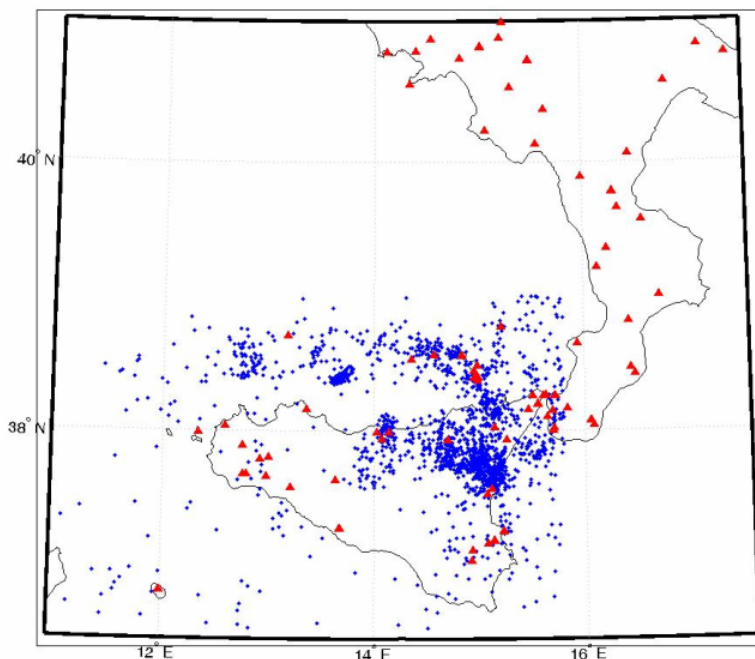


Fig. 7.1 – Map of the 1951 selected epicentres and stations to realize the Sicilian tomography

The *Sicily WAM* is obtained using about 700 lithospheric events that were already used for the construction of the *slab WAM*. This is due, inevitably, to the partial overlying of the area between the *slab WAM* and the *Sicily WAM*. The common area is used as an empirical test to assess the homogeneity of the spatial resolution of the two models.

We performed the “classic” DD tomographies using inversion grids having horizontal regular inter-node distance of 30 km while the vertical one was on average 7 km. The parameterized volume has dimension of 390x270x100 km³ (figure 7.2).

The WAM grid used has an horizontal spacing of 3 km and the vertical one of 2 km. Others tomographies with anisotropic inversion grids and with finer spacing are planned.

We applied the WAM method and the *extended checkerboard* test to evaluate the reliability of the first results (figure 7.3). Thus far we have constructed an experimental V_p WAM of order 9 (figure 7.4). The performed inversions were mainly carried out with different azimuth of the inversion grids. Though the order of the WAM is low, its reconstruction capability is estimated on 58.83% in terms of Restoration index (figure 7.4).

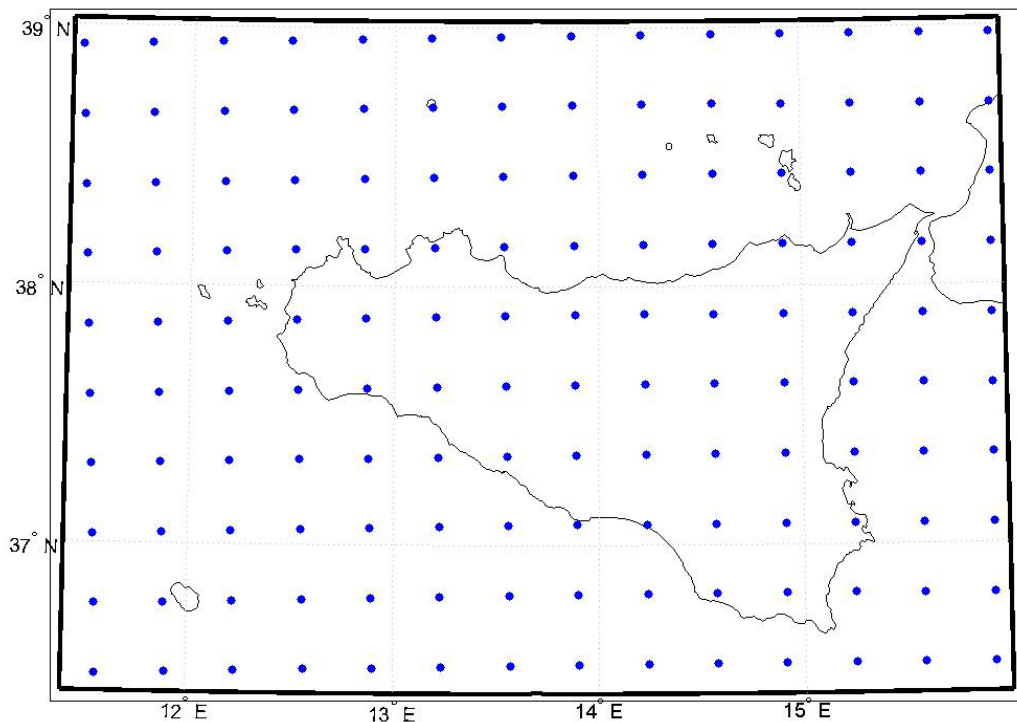


Fig. 7.2 – Grid points used to perform the preliminary inversions and to realize the extended checkerboard test.

To try the matching of the two WAM (the Ionian WAM and Sicilian one) we resampled them into a common WAM grid having size of 450 x 550 x 350 km³ and inter-node spacing of 3x3x2 km³. The velocity values relative to the common volume to the two WAM were determined as the average velocity weighted with the respective DWS (figure 7.5).

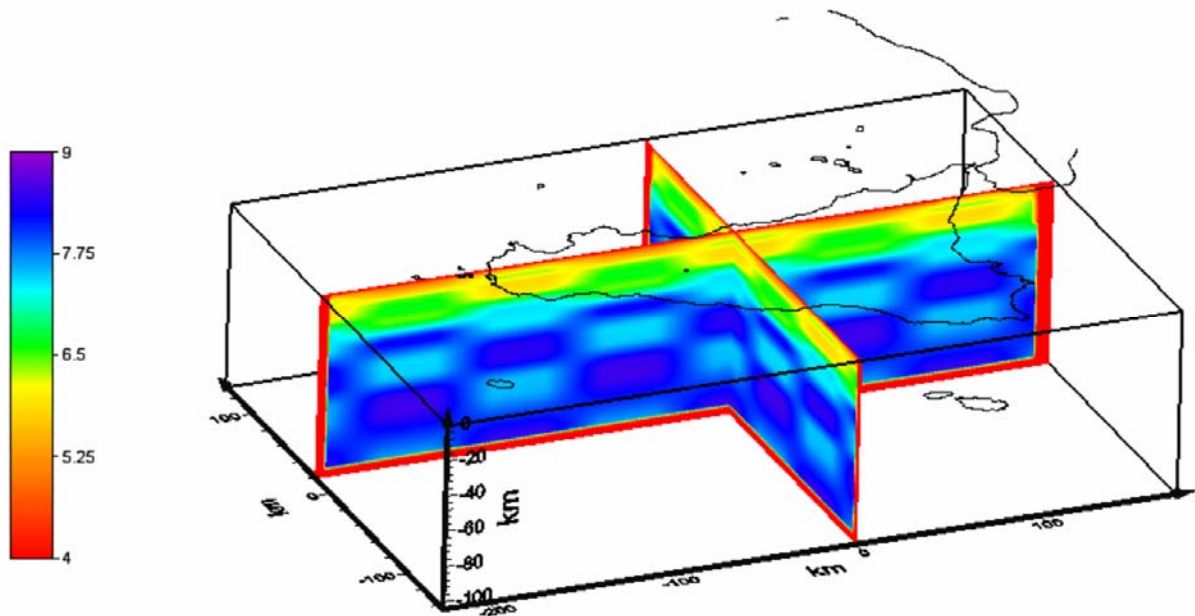


Fig. 7.3 – V_p checkerboard model used to calculate the Synthetic travel times.

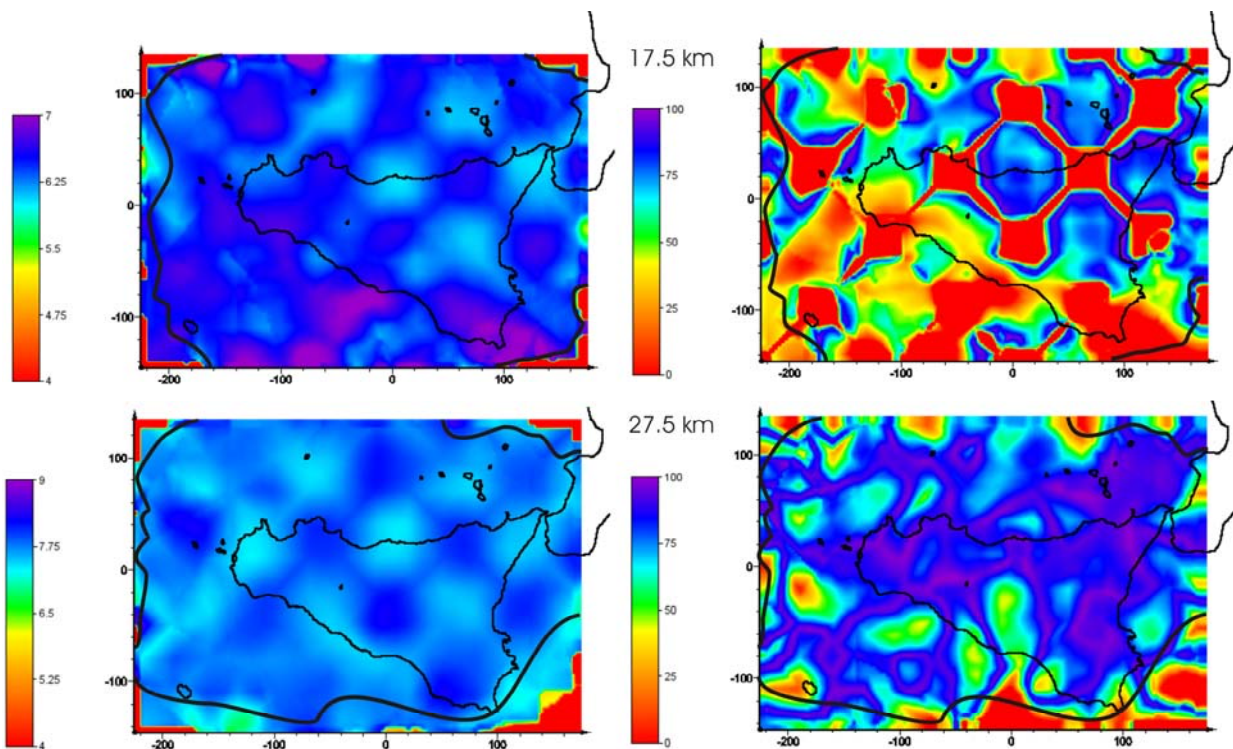


Fig. 7.4 – V_p reconstructed WAM (left) and corresponding restoration index (right) relative to horizontal slices at a depth of 17.5 km (top) and 27.5 km (bottom). The black lines limit the area with $DWS > 100$.

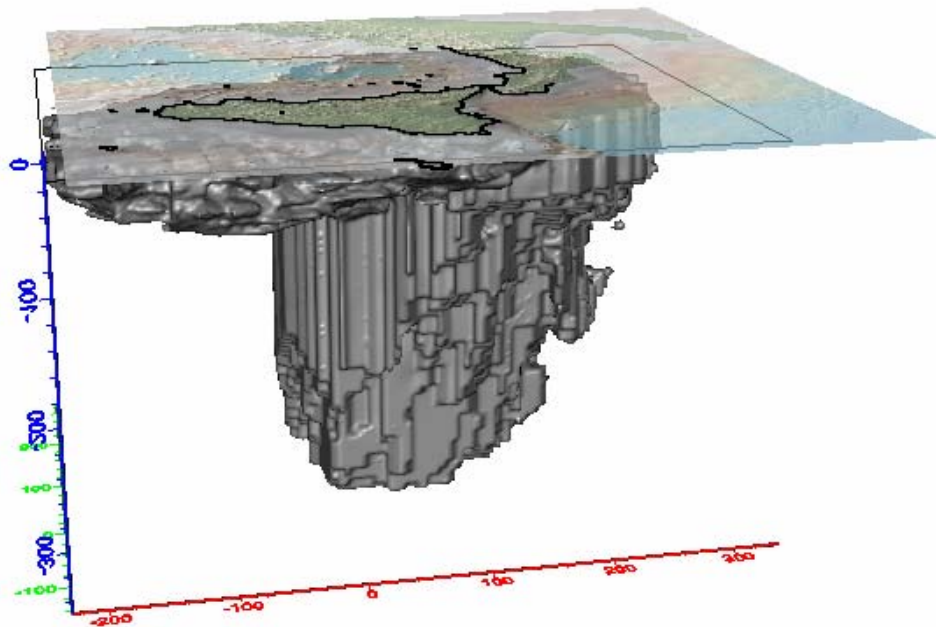
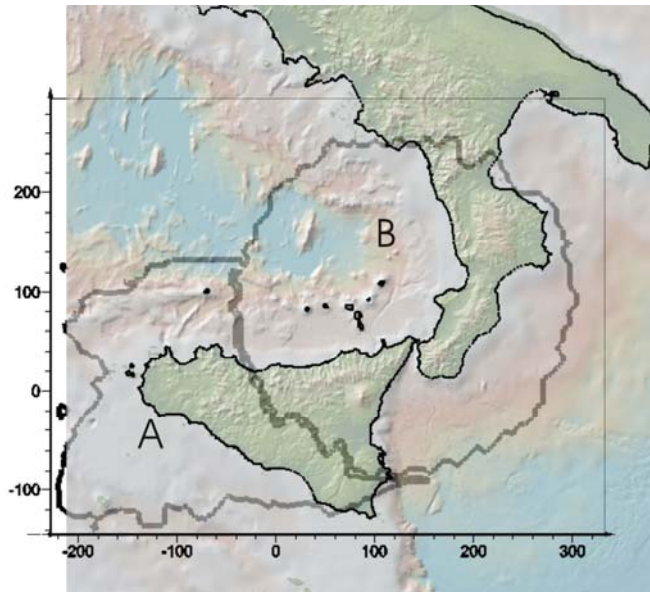


Fig. 7.5 – Map of the unified WAM (top) and its investigated volume (bottom) with DWS greater than 100.

The preliminary unified WAM already gives prominence to interesting features of the Sicilian and Tyrrhenian crust and upper mantle. We show a horizontal slice at a depth of 30 km (figure 7.6) as an example of these preliminary results. The low velocities, (black dashed line in fig 7.6) clearly depicts the root of the Appenine-Maghrebe chain characterizing giving insights on the depth reached by the same chain. Low velocities are recovered again beneath Marsili Palinuro and Stromboli (recovered in in the unified WAM as well as in both tomographies). At this depth the sharp lateral heterogeneity through the Malta escarpment (which is the passive margin between the oceanic Ionian crust and the continental Hyblean Plateau) in E-O direction is also visible showing typical mantle velocities ($V_p > 7.7$ km/s) beneath the Ionian sea and lower velocities beneath the continental *Hyblean Plateau* ($V_p \approx 6.9$ km/s) as highlighted by the two dashed ellipses .

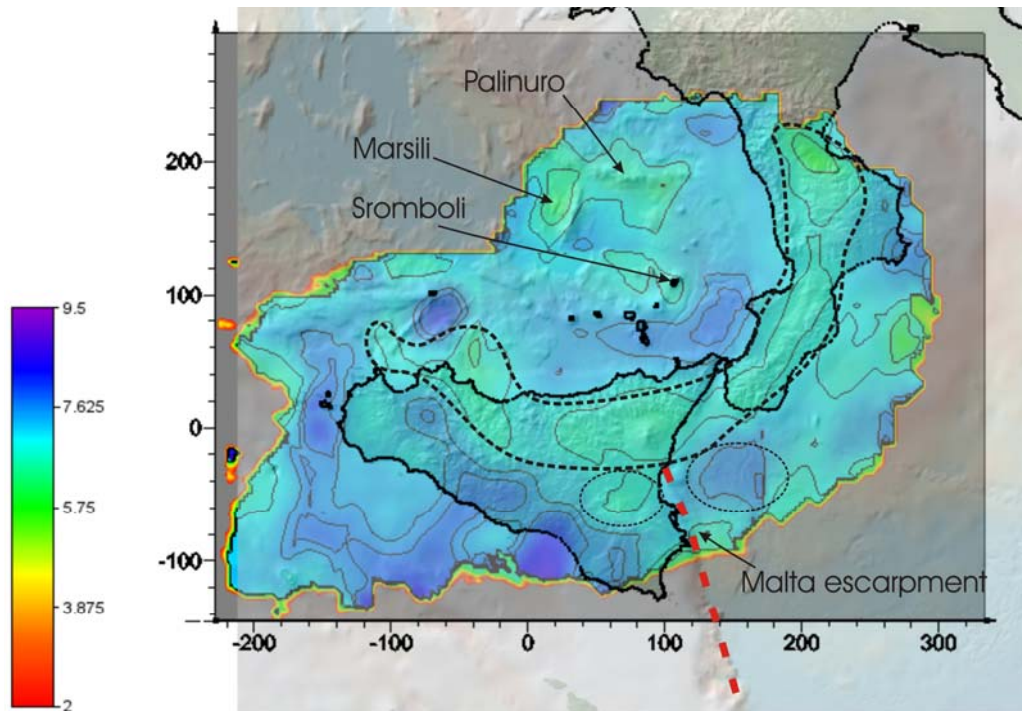


Fig. 7.6 – Map of the unified V_p WAM at a depth of 30 km. The dashed black line encloses the low velocities relative to the Calabrian-Sicilian-Maghrebian-chain root and the red dashed line marks the passive margin of Malta escarpment.

Beside the increase of the WAM order by several other inversions we plan to integrate the data provided by natural seismicity with data provided by several active experiments that are the first-arrivals times picked on the W.A.R.R. (Wide Angle Reflection/Refraction) and D.S.S. (Deep Seismic Soundings) seismic sections recorded in Italy since 1968 (figure 7.7).

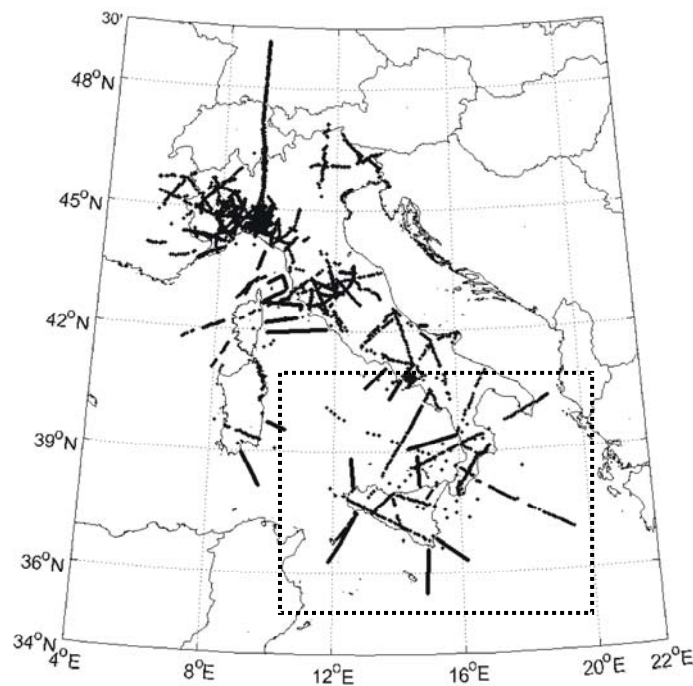


Fig. 7.7 – Map of D.S.S. and W.A.R.R. seismic sections recorded in Italy since 1968. The black dashed rectangle encloses the profiles that we would use of the *integrated active-passive* tomographies.

The unified WAM will be constrained by other seismological data relative to the earthquakes recorded recently and accurately verified, by converting the velocity model in a density one and by comparing its gravimetric response with the Bouguer anomaly field.

Furthermore we plan to perform inversions by using both seismological and gravimetric data to obtain the velocity-density model. Lines *et al.* (1988) propose two main kinds of cooperative inversions of geophysical data. The first one is the joint inversion where all data are inverted simultaneously. This strategy is often used for data sets combining gravity and seismic (Oppenheimer and Herkenhoff 1981; Lees and VanDecar 1991; Kaufmann and Long 1996; Zeyen and Achauer, 1997; Tondi and de Franco, 2006). The respective weight of the two data sets is the main difficulty of the method (Lines *et al.* 1988). The second one is the sequential inversion where each data set is inverted successively. The *a posteriori* information resulting from the previous inversion of the first data set is transformed into *a priori* information to invert the second data set (Vernant *et al.*, 2002).

Finally, the last step of this major project will be the construction of several WAMs to cover a larger area, perhaps the whole Mediterranean, and unify all the models into a very large scale WAM to completely describe the Africa-Europe contact from the western part (Morocco- Algeria) up to its eastern one (Greece-Turkey) by preserving the reliability and the detail that are characteristics of a WAM.

However, these first results already offer an interesting contribution to the description and geodynamic interpretation of the buried structures of the central Mediterranean Sea.

APPENDIX 1: LSQR

Let us have a system of linear equations

$$A\mathbf{x} = \mathbf{d}, \tag{1}$$

in which A is a $m \times n$ matrix, that is, there are m model parameters and n observed data.

Assuming Gaussian a priori probability density functions for the data and the model, with covariance matrices C_d and C_x , respectively, we obtain the maximum-likelihood estimate of the tomographic solution by minimising (Tarantola and Nercessian, 1984; Tarantola, 1987),

$$S(\mathbf{x}) = \frac{1}{2} \left[(A\mathbf{x} - \mathbf{d})^T C_d^{-1} (A\mathbf{x} - \mathbf{d}) + (\mathbf{x} - \mathbf{x}_0)^T C_x^{-1} (\mathbf{x} - \mathbf{x}_0) \right]. \tag{2}$$

Eq. 2 implies that a weighted mean of the misfit $\|A\mathbf{x} - \mathbf{d}\|$ and the distance of the solution \mathbf{x} to some preferred model \mathbf{x}_0 is minimised. The latter condition implies that \mathbf{x} does not yield the least possible value for the misfit, except in the unlikely case that it is given by \mathbf{x}_0 itself. Thus, the solution is biased towards \mathbf{x}_0 . The seriousness of this bias depends on the weighting matrices C_d and C_x , which act as a metric in data and model space, respectively.

Differentiating S with respect to the component x_i , we obtain

$$A^T C_d^{-1} (A\mathbf{x} - \mathbf{d}) + C_x^{-1} (\mathbf{x} - \mathbf{x}_0) = \mathbf{0}, \tag{3}$$

so

$$\mathbf{x} = \mathbf{x}_0 + (A^T C_d^{-1} A + C_x^{-1})^{-1} A^T C_d^{-1} (\mathbf{d} - A\mathbf{x}_0). \tag{4}$$

This, with a little of algebraic manipulation, can also be written as

$$\mathbf{x} = \mathbf{x}_0 + C_x A^T (A C_x A^T + C_d)^{-1} (\mathbf{d} - A\mathbf{x}_0). \tag{5}$$

The same equations are often obtained with a purely numerical frame, when it is recognised that the simple least-squares solution of 1 must be scaled for different data errors (C_d diagonal) and damped to keep the propagation of errors under control when $A^T A$ is singular or ill-conditioned (Nolet, 1993a). Scaling the model components one then adds constraints in the form $C_x^{-1/2} \mathbf{x} = \mathbf{0}$ to the original equations to obtain a damped system, of the form

$$\begin{bmatrix} C_d^{-1/2} A \\ C_x^{-1/2} \end{bmatrix} \mathbf{x} = \begin{bmatrix} C_d^{-1/2} \mathbf{d} \\ \mathbf{0} \end{bmatrix}, \tag{6}$$

and one easily establishes that the least-squares solution of this conforms to 2 for a zero preferred model \mathbf{x}_0 . Thus, a properly scaled regularisation of the system is equivalent to selecting the maximum-likelihood estimate. In the linear approximation, the assumption $\mathbf{x}_0 = \mathbf{0}$ does not affect the general validity of the analysis.

The inversion method of Tarantola and Nercessian (1984), which is based on the Bayesian premise 2 and the subsequently derived solution (eqs. 4-6) is usually referred to as ‘inversion without blocks’. The term refers to one peculiar aspect of their formalism: it is carried through for continuous (un-parameterised) models to the very end. This is not, however, what makes their method fundamentally different from tomographic inversions using ART (Algebraic Reconstruction Technique; Gordon et al., 1970; Tanabe, 1971; Herman et al., 1973; Natterer, 1986) or SIRT (Simultaneous Iterative Reconstruction Technique; Gilbert, 1972; Dines and Lytle, 1979; Ivansson, 1983). Even the ‘inversion without blocks’ must be implemented on a computer, which will inevitably lead to model discretisation. What distinguishes the method from the ad hoc iterative methods is that the

problem of under-determination is handled not arbitrarily, but using principles well grounded in probability theory (see Tarantola, 1987). In other words, the regularisation of the solution is carried out with an a priori covariance C_x , not by an arbitrary metric decided by the ray coverage of the medium. Here the question of efficient methods will be addressed, which yield the minimum-norm solution of least-squares systems with arbitrary weighting. It is important to distinguish between biased and unbiased regularisation. In unbiased regularisation, we select, among all models that minimise $\|Ax - \mathbf{d}\|$, the one that is smallest in a weighted norm, $\min \|C_x^{-1/2} \mathbf{x}\|^2$. This can easily be found by any method that minimises the un-weighted Euclidean norm of the vector of unknowns, by defining $\mathbf{x}' = C_x^{-1/2} \mathbf{x}$ and solving $\|A' \mathbf{x}' - \mathbf{d}\|$ where $A' = AC_x^{-1/2}$. After solving, the original solution \mathbf{x} can be recovered by multiplication with $C_x^{-1/2}$. If $C_x^{-1/2}$ is a matrix which operates as an averaging window, this will yield a smooth solution. Note that this inverse is then a matrix that magnifies the roughness, so that we expect the oscillating features of the model already to be damped by minimising \mathbf{x}' .

In biased regularisation we allow $\|Ax - \mathbf{d}\|$ to be larger than the absolute minimum, in order to obtain a smaller a posteriori variance of the solutions (Wiggins, 1972). Since tomographic data invariably contain errors, and often very large ones, some form of damping to reduce the a posteriori variance is always necessary. So it may be expedient to invert 6 rather than 1.

The LSQR method, due to Paige and Saunders (1982), is the most efficient method so far available to solve linear tomographic systems, whether over-determined, under-constrained or both (Nolet, 1983; 1985; Scales, 1987; Van der Sluis and Van der Vorst, 1987; 1990). Moreover, it retains full flexibility in the sense that it does not introduce any hidden scaling in the solution. Since it is able to solve the Bayesian estimation problem 3.10.87, it is a method favoured by a number of authors (e.g. Nolet, 1993a). A brief derivation of this method shall be given in this section. For an extension of this method to continuous models and complex variables, see e.g. Nolet and Snieder (1990).

Let us solve the linear problem 1, where now A may have a structure including the a priori covariance matrices, as in 6 (in which case \mathbf{d} is extended with m zeros). LSQR employs a process called Lanczos iteration to construct an orthonormal basis $\boldsymbol{\mu}_1, \boldsymbol{\mu}_2, \dots, \boldsymbol{\mu}_k$ in the m -dimensional space of models. At the same time, a similar orthonormal basis $\boldsymbol{\rho}_1, \boldsymbol{\rho}_2, \dots, \boldsymbol{\rho}_k$ grows in the n -dimensional space of data vectors. The first $\boldsymbol{\rho}_1$ is found by normalising \mathbf{d} , as in $\beta_1 \boldsymbol{\rho}_1 = \mathbf{d}$, and the first $\boldsymbol{\mu}_1$ by back projection of $\boldsymbol{\rho}_1$, as in $\alpha_1 \boldsymbol{\mu}_1 = A^T \boldsymbol{\rho}_1$. Factors β_i and α_i normalise $\|\boldsymbol{\rho}_i\|$ and $\|\boldsymbol{\mu}_i\|$, respectively. We find the second basis vector in data space by projecting $\boldsymbol{\mu}_1$, orthogonalising this to $\boldsymbol{\rho}_1$ and normalising,

$$\beta_2 \boldsymbol{\rho}_2 = A \boldsymbol{\mu}_1 - \alpha_1 \boldsymbol{\rho}_1. \quad 7$$

We may now use $\boldsymbol{\rho}_2$ to construct the second basis vector in model space. Using back projection and subsequent orthogonalisation to $\boldsymbol{\mu}_1$, we find

$$\alpha_2 \boldsymbol{\mu}_2 = A^T \boldsymbol{\rho}_2 - \beta_2 \boldsymbol{\mu}_1. \quad 8$$

This suggests a sequence of projections and back projections of the form

$$\beta_{k+1} \boldsymbol{\rho}_{k+1} = A \boldsymbol{\mu}_k - \alpha_k \boldsymbol{\rho}_k, \quad 9$$

$$\alpha_{k+1} \boldsymbol{\mu}_{k+1} = A^T \boldsymbol{\rho}_{k+1} - \beta_{k+1} \boldsymbol{\mu}_k. \quad 10$$

The orthogonality of the bases $\{\boldsymbol{\mu}_i\}$ and $\{\boldsymbol{\rho}_i\}$ is easily established by induction. Suppose

$\boldsymbol{\rho}_1, \boldsymbol{\rho}_2, \dots, \boldsymbol{\rho}_k$ and $\boldsymbol{\mu}_1, \boldsymbol{\mu}_2, \dots, \boldsymbol{\mu}_k$ are orthonormal. We then take the inner product of 10 with $\boldsymbol{\mu}_j$,

$$\alpha_{k+1} \boldsymbol{\mu}_{k+1}^T \boldsymbol{\mu}_j = \boldsymbol{\rho}_{k+1}^T A \boldsymbol{\mu}_j - \beta_{k+1} \boldsymbol{\mu}_k^T \boldsymbol{\mu}_j = (\beta_{j+1} \boldsymbol{\rho}_{j+1} + \alpha_j \boldsymbol{\rho}_j)^T \boldsymbol{\rho}_{k+1} - \beta_{k+1} \delta_{kj}. \quad 11$$

For $j < k$ all terms are 0, whereas the expression sums to 0 for $j = k$. Similarly, for $j \leq k$,

$$\beta_{k+1} \boldsymbol{\rho}_{k+1}^T \boldsymbol{\rho}_j = \boldsymbol{\mu}_k^T A^T \boldsymbol{\rho}_j - \alpha_k \boldsymbol{\rho}_k^T \boldsymbol{\rho}_j = \alpha_j \boldsymbol{\mu}_k^T \boldsymbol{\mu}_j + \beta_j \boldsymbol{\mu}_k^T \boldsymbol{\mu}_{j-1} - \alpha_k \delta_{kj} = 0. \quad 12$$

After k iterations the $\boldsymbol{\mu}_1, \boldsymbol{\mu}_2, \dots, \boldsymbol{\mu}_k$ span a subspace of the model space. The precise extent of this space depends on \mathbf{d} , but it is important to notice that regions in model space that are very sensitive to the data are part of this subspace, even if \mathbf{d} has only a small component in its direction. To see this, notice that the sequence of projections and back projections involves repeated multiplications with $A^T A$. If $\boldsymbol{\eta}$ is an eigenvector of this system with eigenvalue λ , the component of $\boldsymbol{\mu}_1$ in the direction of $\boldsymbol{\eta}$ will increase in magnitude by a factor λ^k after k iterations, until it becomes so large that the corrective action and the orthogonalisation becomes noticeable.

If we now expand the solution \mathbf{x} in terms of the new basis,

$$\mathbf{x} = \sum_{j=1}^k m_j \boldsymbol{\mu}_j, \quad 13$$

the original system becomes

$$\sum_{j=1}^k m_j A \boldsymbol{\mu}_j = \mathbf{d} = \beta_1 \boldsymbol{\rho}_1, \quad 14$$

or, using 3.10.94,

$$\sum_{j=1}^k m_j (\beta_{j+1} \boldsymbol{\rho}_{j+1} + \alpha_j \boldsymbol{\rho}_j) = \beta_1 \boldsymbol{\rho}_1. \quad 15$$

Taking the inner product of this with $\boldsymbol{\rho}_1$ yields $m_1 = \beta_1 / \alpha_1$, while with $\boldsymbol{\rho}_p$ it gives the subsequent factors as $m_p = -\beta_p m_{p-1} / \alpha_p$. Thus, we build the solution while iterating. Paige and Saunders (1982) improve on the numerical stability of this by explicitly minimising $\mathbf{d} - A\mathbf{x}$ in every step while retaining computational efficiency. A simple subroutine of their algorithm is also given in Nolet (1987).

The LSQR allows for full specification of $C_x^{-1/2}$, which need not be diagonal. A practical and useful form of this matrix can be determined when we realise that the correlation matrix C_x acts as a smoothing operator (Tarantola, 1987). The same must be then true for $C_x^{-1/2}$, and its inverse is essentially a roughening operator. The simplest roughening operator takes a difference of a cell with all its neighbours. If we impose the condition

$$\min \sum_i \frac{1}{2n_i} \sum_{\text{neighb}} (\mathbf{x}_i - \mathbf{x}_j)^2, \quad 16$$

where n_i is the number of neighbours of cell i , this results in m extra equations,

$$n_k \mathbf{x}_k - \sum_{\text{neighb}} \mathbf{x}_i = \mathbf{0}, \quad 17$$

which define the added equations in 6. Convergence of the smoothing part of the linear system may be slow and more iterations are generally needed than with simple damping using a diagonal C_x (Nolet, 1993a). It is also possible to constrain the magnitude of $\nabla^2 \mathbf{v}(\mathbf{r})$ (Tarantola, 1987; Park, 1989).

References

- Abers G.A., and Roecker S. (1991): *Deep structure of an arc:continent collision: earthquake relocation and inversion for upper mantle P and S wave velocities beneath Papua New Guinea*, J. Geophys. Res., 96, 6379-6401.
- Abers G.A. (2005): *Seismic low-velocity layer at the top of subducting slabs: observations, predictions, and systematic*. Phys. Earth Planet. Inter., 149, 7-29.
- Akbar F.E., Calderon Macias C., Sen V., Sen M.K., Stoffa P.L. (1998): *A comparative study of first arrival time computation for 3:D inhomogeneous isotropic velocity models*. SEG Expanded Abstracts, 1728-1731.
- Akbar F.E. (1997): *Three-dimensional prestack plane-wave Kirchhoff depth migration in laterally varying media*. PhD Thesis, The University of Texas at Austin.
- Aki K., Christoffersson A., Husebye E.S. et al. (1974): *Three-dimensional seismic:velocity anomalies in the crust and upper:mantle under the U.S.G.S. California seismic array (abstract)*. Eos, Trans. Am. Geophys. Union, 56, 1145.
- Aki K. and Lee W.H.K. (1976): *Determination of three:dimensional velocity anomalies under a seismic array using first P:arrival times from local earthquakes. 1. A homogeneous initial model*. J. Geophys. Res., 81, 4381-4399.
- Aki K. and Richards P.G. (1980): *Quantitative seismology: theory and methods*. W.H. Freeman & Co., New York, 932.
- Aki K., Christoffersson A. and Husebye E.S. (1977): *Determination of the three:dimensional seismic structure of the lithosphere*. J. Geophys. Res., 82, 277-296.
- Aki K. (1982): *Three:dimensional inhomogeneities in the lithosphere and asthenosphere: Evidence for decoupling in the lithosphere and flow in the asthenosphere*. Rev. Geophys. Space Phys., 20, 161-170.
- Akimoto, S. and Fujisawa H. (1968): *Olivine-spinel solid solution equilibrium in the system magnesium orthosilicate-iron(II) orthosilicate*. J. Geophys. Res. 73, 1467-1479.
- Amato, A., B. Alessandrini, and Cimini G.B. (1993a): *Teleseism wave tomography of Italy, in Seismic tomography: Theory and Practise*, edited by H. M. Iyer and K. Hirahara, , CRC Press, Boca Raton, Fla. 361-397.
- Amato A., Alessandrini B., Cimini G.B., Frepoli A., and Selvaggi G. (1993b): *Active and remnant subducted slabs beneath Italy: Evidence from seismic tomography and seismicity*, Annali di Geofisica, 36, 201-214.
- Anderson, H. and J. Jackson (1987): *The deep seismicity of the Tyrrhenian Sea*, Geophys. J. R. Astron. Soc., 91, 613-637.
- Argnani, A. (2000): *The southern Tyrrhenian subduction system: Recent evolution and neotectonic implications*, Ann. Geophys., 43, 585-607.
- Ashiya K., Asano S., Yoshii T., Ishida M. and Nishiki T. (1987): *Simultaneous determination of the three:dimensional crustal structure and hypocenters beneath the Kanto:Tokai District, Japan*. Tectonophysics, 140, 13-27.
- Baccheschi, P., Margheriti, L., Steckler, M. S., (2007): *Seismic anisotropy reveals focused mantle flow around the Calabrian slab (Southern Italy)*. Geophys. Res. Lett., 34. doi: 10.1029/2006GL028899.
- Backus G.E. (1964): *Geographical interpretation of measurements of average phase velocities of surface waves over great circular and great semi:circular paths*. Bull. Seism. Soc. Am., 54, 571-610.
- Backus G.E. (1989): *Confidence set inference with a priori quadratic bound*. Geophys. J., 97, 119-150.
- Barberi, F., Gasparini P., Innocenti F., and Villari L. (1973): *Volcanism of the southern Tyrrhenian Sea and its geodynamic implications*, J. Geophys. Res., 78, 5221-5232.
- Berryman J.G. (1991): *Lecture notes on nonlinear inversion and tomography*. Lawrence Livermore National Laboratory, Livermore, California (USA).
- Beydoun W. and Mendes M. (1989): *Elastic ray Born l_2 :migration/inversion*. Geophys. J., 97, 151-160.
- Bijwaard H., Spakman W. and Engdahl E.R. (1998): *Closing the gap between regional and global travel time tomography*. J. Geophys. Res., 103, 30055-30078.
- Bohm, G., Galuppo P., and Vesnaver A., (2000): *3D adaptive tomography using Delaunay triangles and Voronoi polygons*, Geophys. Prospect. 48, 723-744.
- Bois P., La Porte M., Lavergne M. and Thomas G. (1972): *Well:to:well seismic measurements*. Geophysics, 37, 471-480.
- Born M. (1926): *Quantenmechanik der Stressvorgänge (Quantum mechanics of impact processes)*. Z. Phys., 38, 803-827.
- Born M. and Wolf E. (1980): *Principles of optics : Electromagnetic theory of propagation, interference, and diffraction of light*. Pergamon Press, Oxford, 1-453.
- Caputo, M., Panza G. F., and Postpischil D. (1970): *Deep structure of the Mediterranean Basin*, J. Geophys. Res., 75, 4919-4923.

- Carminati S., Negredo A.M., Valera J.L., and Doglioni C. (2005): *Subduction-related intermediate-depth and deep seismicity in Italy: insights from thermal and rheological modelling*. Phys. Earth Planet. Inter. 149, 65-79.
- Catalano R., Doglioni C., Merlini S., (2001): *On the Mesozoic Ionian basin*. Geophys. J. Int. 144, 49-64.
- Chiarabba C., De Gori P., and Speranza F., (2008): *The southern Tyrrhenian subduction zone: Deep geometry, magmatism and Plio-Pleistocene evolution*, Earth Planet. Sci. Lett., 268 408-423
- Christensen N. I. (1996): *Poisson's ratio and crustal seismology*, J. Geophys. Res. 101, 3139-3156.
- Cimini G.B., and Amato A. (1993): *P-wave teleseismic tomography contribution to the delineation of the upper mantle structure of Italy, in Recent Evolution and Seismicity of the Mediterranean Region*, edited by E. Boschi, E. Mantovani, and A. Morelli, Springer, New York, 313-331.
- Cimini G.B. (1999): *P-wave deep velocity structure of the southern Tyrrhenian subduction zone from nonlinear teleseismic traveltimes tomography*, Geophys. Res. Lett., 26(24), 3709-3712.
- Cimini G.B., and Marchetti A. (2006): *Deep structure of peninsular Italy from seismic tomography and subcrustal seismicity*, Ann. Geophys., 49(1), 331-345.
- Clayton R.W. and Comer R.P. (1983): *A tomographic analysis of mantle heterogeneities from body wave travel times*. Eos, Trans. Am. Geophys. Union, 64, 776.
- Clayton R.W. and McMechan G.A. (1981): *Inversion of refraction data by wave field continuation*. Geophysics, 46, 860-868.
- Cleary J. and Hales A.L. (1966): *An analysis of the travel times of P waves to North American stations, in the distance range 32° to 100°*. Bull. Seism. Soc. Am., 56, 467-489.
- Connolly, J.A.D., Kerrick, D.M., (2002): *Metamorphic controls on seismic velocity of subducted oceanic crust at 100–250 km depth*. Earth Planet. Sci. Lett. 204, 61–74.
- Cormack A.M. (1963): *Representation of a function by its line integrals, with some radiological applications*. J. Appl. Phys., 34, 2722-2727.
- Crase E., Wideman C., Noble M. and Tarantola A. (1992): *Nonlinear elastic waveform inversion of land seismic reflection data*. J. Geophys. Res., 97:B4, 4685-4704.
- Crosson R.S. (1976): *Crustal structure modeling of earthquake data. Part I. Simultaneous least squares estimation of hypocenter and velocity parameters*. J. Geophys. Res., 81, 3036-3046.
- Chou C.W. and Booker J.R. (1979): *A Backus-Gilbert approach to the inversion of travel time data for three dimensional velocity structure*. Geophys. J. R. Astron. Soc., 59, 325-344.
- Cuenot N., Dorbath C., Dorbath L. (2008): *Analysis of the Microseismicity Induced by Fluid Injections at the EGS Site of Soultz-sous-Forêts (Alsace, France): Implications for the Characterization of the Geothermal Reservoir Properties* Pure & Applied Geophysics PAGEOPH, Vol. 165, N 5 2008 , 797-828(32)
- Davies J.H., Stevenson D.J., (1992): *Physical model of source region of subduction zone volcanics*. J. Geophys. Res. 97, 2037-2070.
- Della Vedova B., Pellis G., Foucher J.P., and Rehault P. (1984): *Geothermal structure of the Tyrrhenian Sea*, Mar. Geol., 55, 271-289.
- Dercourt J., et al. (1986): *Geological evolution of the Tethys Belt from the Atlantic to the Pamirs since the Lias*, Tectonophysics, 123, 241-315.
- Devaney A.J. (1984): *Geophysical diffraction tomography*. IEEE Trans. Geosci. Remote Sens., GE:22, 3-13.
- De Voogd B., Truffert C., Chamot-Rooke N., Huchon P., Lallemand S., and Le Pichon X. (1992): *Two-ship deep seismic soundings in the basin of the eastern Mediterranean Sea (Pasiphae cruise)*, Geophys. J. Int., 109, 536-552.
- Dewey J. F., Helman M.L., Turco E., Hutton D.W.H., and Knott S.D. (1989): *Kinematics of the western Mediterranean, in Alpine Tectonics, edited by M. P. Coward, D. Dietrich, and R. G. Park*, Spec. Publ. Geol. Soc. London, 45, 265-283.
- De Astis G., Kempton P.D., Peccerillo A., Wu T.W. (2006): *Trace element and isotopic variations from Mt. Vulture to Campanian volcanoes: constraints for slab detachment and mantle inflow beneath southern Italy*. Contrib. Mineral. Petrol., 151, 331-351, doi: 10.1007/s00410-006-0062-y.
- De Mets C., Gordon R.G., Argus D.F. Stein S. (1990): *Current plate motion*. Geophys. J. Int., 101, 425
- Dines K.A. and Lytle R.J. (1979): *Computerized geophysical tomography*. Proc. IEEE, 67, 1065-1073.
- Dyer B. and Worthington M.H. (1988): *Some sources of distortion in tomographic velocity images*. Geophys. Prospect., 36, 209-222.
- Di Stefano R., C. Chiarabba, F. Lucente, and Amato A. (1999): *Crustal and uppermost mantle structure in Italy from the inversion of P-wave arrival times: geodynamics implications*, Geophys. J. Int., 139, 483-498.
- Doglioni C., Gueguen E., Harabaglia P. and Mongelli F. (1999): *On the origin of W-directed subduction zones and applications to the western Mediterranean*. Geol. Soc. Sp. Publ., 156, 541-561.
- Doglioni C., Carminati E., Cuffaro M., & Scrocca D. (2007): *Subduction kinematics and dynamic constraints*. Earth-Science Reviews Volume 83, Issues 3-4, pp 125-175.

- Dorbath C., Gerbault M., Carlier G., Guiraud M. (2008): *Double seismic zone of the Nazca plate in northern Chile: High-resolution velocity structure, petrological implications, and thermomechanical modelling*. *Geochemistry Geophysics Geosystem*: Vol 9, N 7 doi:10.1029/2008GC002020. ISSN: 1525-2027, 1-29
- Dziewonski A.M. (1975): *Resolution of large scale velocity anomalies in the mantle*. *Eos, Trans. Am. Geophys. Union*, 56, 395.
- Dziewonski A.M. (1984): *Mapping the lower mantle: Determination of lateral heterogeneity in P velocity up to degree and order 6*. *J. Geophys. Res.*, 89, 5929-5952.
- Dziewonski A.M. (1996): *Earth's mantle in three dimensions*. In *Seismic modelling of Earth's Structure*, edited by E. Boschi, G. Ekström G. and A. Morelli for Istituto Nazionale di Geofisica (Editrice Compositori, Bologna), 507-572.
- Dziewonski A.M. and Anderson D.L. (1983): *Travel times and station corrections for P waves at teleseismic distances*. *J. Geophys. Res.*, 88, 3295-3314.
- Dziewonski A.M. and Anderson D.L. (1984): *Seismic tomography of the Earth's interior*. *Am. Sci.*, 721, 483-494.
- Dziewonski A.M. and Woodhouse J.H. (1987): *Global images of the Earth's interior*. *Science*, 236, 37-48.
- Houndsfield G.N. (1973): *Computerized transverse axial scanning tomography: Part I. Description of the system*. *Br. J. Radiol.*, 46, 1016-1022.
- Eberhart-Phillips D. (1986): *Three-dimensional velocity structure in northern California coast ranges from inversion of local earthquake arrival times*. *Bull. Seism. Soc. Am.*, 76, 1025-1052.
- Eberhart-Phillips D. (1990): *Three-dimensional P and S velocity structure in the Coalinga region, California*. *J. Geophys. Res.*, 95, 15343-15363.
- Eberhart-Phillips D., Labson V.F., Stanley W.D., Michael A.J. and Rodriguez B.D. (1990): *Preliminary velocity and resistivity models of the Loma Prieta earthquake region*. *Geophys. Res. Lett.*, 17, 1235-1238.
- Eberhart-Phillips D. and Michael A.J. (1993): *Three-dimensional velocity structure, seismicity, and fault structure in the Parkfield region, central California*. *J. Geophys. Res.* 98, 737-758.
- Ellsworth W.L. (1977): *Three-dimensional structure of the crust and mantle beneath the island of Hawaii*. PhD Thesis, Massachusetts Institute of Technology, Cambridge.
- Evans J.R. and Achauer U. (1993): *Teleseismic velocity tomography using the ACH method: theory and application to continental-scale studies*. In *Seismic tomography: theory and practice*, edited by H.M. Iyer and K. Hirahara (Chapman and Hall, London), 319-360.
- Faccenna C., Davy P., Brun J.P., Funicello R., Giardini D., Mattei M., and Nalpas T. (1996): *The dynamics of back-arc extension: An experimental approach to the opening of the Tyrrhenian Sea*, *Geophys. J. Int.*, 126, 781-795.
- Faccenna C., Funicello F., Giardini D., and Lucente P. (2001): *Episodic back-arc extension during restricted mantle convection in the central Mediterranean*, *Earth Planet. Sci. Lett.*, 187, 105-116.
- Evans J.R., Eberhart-Phillips D. and Thurber C.H. (1994): *User's Manual for SIMULPS12 for Imaging vp and vp/vs: A derivative of the "Thurber" tomographic inversion SIMUL3 for Local Earthquakes and Explosions*. Open:file Report 94:431, U.S. Geological Survey. 1-101.
- Falcone C. and Beranzoli L. (1997): *Introduction to the inverse problem in seismic tomography*. Istituto Nazionale di Geofisica, pubbl. n. 588, Rome.
- Farra V., Virieux J. and Madariaga R. (1989): *Ray perturbation theory for interfaces*. *Geophys. J. Int.*, 99, 377-390.
- Farra V., Madariaga R. and Virieux J. (1994): *The ambiguity, in ray perturbation theory comment*. *J. Geophys. Res.*, 99, 21963-21968.
- Fehler M. and Pearson C. (1984): *Crosshole seismic surveys: applications for studying subsurface fracture systems at a hot dry rock geothermal site*. *Geophysics*, 49, 37-45.
- Finetti, I., and Del Ben A. (1986): *Geophysical study of the Tyrrhenian opening*, *Bol. Geofis. Teor. Appl.*, 28, 75-156.
- Finetti I.R. (2005): *The Calabrian arc and subducting Ionian slab from new CROP seismic data*. CROP PROJECT: Deep Seismic exploration of the Central Mediterranean and Italy ISBN: 0444506934. Elsevier, 393-412.
- Francalanci, L., Taylor S.R., McCulloch M.T., and Woodhead J. (1993): *Geochemical and isotopic variations in the calc-alkaline rocks of Aeolian Arc, southern Tyrrhenian Sea, Italy: Constraints on magma genesis*, *Contrib. Mineral. Petrol.*, 113, 300-313.
- Fréchet, J. (1985): *Sismogene`se et doublets sismiques*, The`se d'Etat, Universite' Scientifique et Me'dicale de Grenoble, 206.
- Fumagalli P, Poli S. (2005): *Experimentally determined phase relations in hydrous peridotites to 6.5 GPa and their consequences on the dynamics of subduction zones*. *Jour. Petrol.*, 46, 555-578.
- Gasperini D., Blichert Toft J., Bosch D., Del Moro A., Macera P., Albarède F. (2002): *Upwelling of deep mantle material through a plate window: evidence from the geochemistry of Italian basaltic volcanics*. *J. Geophys. Res.*, 107, B12, 2367, doi:10.1029/2001JB000418

- Gauthier O., Virieux J. and Tarantola A. (1986): *Two-dimensional nonlinear inversion of seismic waveforms: numerical results*. Geophysics, 51, 1387-1403.
- Giardini D., and M. Velona` (1991): *The deep seismicity of the Tyrrhenian Sea*, Terra Nova, 3, 57-64.
- Gill P.E., Murray W., and Wright M.H. (1981): *Practical optimization*: Academic Press.
- Giunta G., Luzio D., Tondi E., De Luca L., Giorgianni A., D'Anna G., Renda P., Cello G., Nigro F., Vitale M. (2004): *The Palermo (Sicily) seismic cluster of September 2002, in the seismotectonic framework of the Tyrrhenian Sea-Sicily border area*. Annals of Geoph., 47, 1775-1770.
- Grainger P. and McCann D.M. (1977): *Interborehole acoustic measurements in site investigation*. Q.J. Eng. Geol., 10, 241-255.
- Goldstein H. (1980): *Classical mechanics*. Addison Wesley, Reading, Mass. (USA)
- Got, J.L., Fréchet J., and Klein F. W. (1994): *Deep fault plane geometry inferred from multiplet relative relocation beneath the south flank of Kilauea*, J. Geophys. Res. 99, 15,375-15,386.
- Gvirtzman Z., Nur A. (2001): *Residual topography, lithospheric structure and sunken slab in the central Mediterranean*. Earth Plan. Sci. Lett., 187, 117-130.
- Gueguen E., Doglioni C. and Fernandez M., (1998): *On the post-25 Ma geodynamic evolution of the western Mediterranean*. Tectonophysics, 298, 259–269.
- Gueguen E., Doglioni C., Fernandez M., (1997): *Lithospheric boudinage in the western Mediterranean back-arc basins*. Terra Nova 9, 184–187.
- Hadiouche O. and Jobert H. (1988): *Geographical distribution of surface:wave velocities and 3:D upper mantle structure in Africa*. Geophys. J., 95, 87-100.
- Hager B.H., Clayton R.W., Richards M.A., Comer R.P., and Dziewonski A.M. (1985): *Lower mantle heterogeneity, dynamic topography and the geoid*. Nature, 313, 541-545.
- Hacker B.R., Abers G.A., Peacock S.M. (2003a): *Subduction factory 1) Theoretical mineralogy, densities, seismic wave speeds, and H₂O contents*. J. Geoph. Res., 108 (B1) 2029, 03311 doi:10.129/2001JB001127.
- Hacker B.R., Peacock S.M., Abers G.A., and Holloway S.D., (2003b): *Subduction factory 2. Are intermediate-depth earthquakes in subducting slabs linked to metamorphic dehydration reactions?* J. Geophys. Res., 108, 2030.
- Harris J.M. (1987): *Diffraction tomography with arrays of discrete sources and receivers*. IEEE Trans. Geosci. Remote Sensing, GE:25, 448-455.
- Hawley B.W., Zandt G. and Smith R.B. (1981): *Simultaneous inversion for hypocenters and lateral velocity variations: an iterative solution with a layered model*. J. Geophys. Res. 86, 7073-7076.
- Hirahara K. (1993): *Tomography using both local earthquakes and teleseisms: velocity and anisotropy : theory*. In Seismic tomography: theory and practice, edited by H.M. Iyer and K. Hirahara (Chapman and Hall, London), 49-518.
- Hirahara K. and Ishikawa Y. (1984): *Travel:time inversion for three:dimensional P:wave velocity anisotropy*. J. Phys. Earth., 32, 60-71.
- Horiuchi S., Ishii H. and Takagi A. (1982): *Two:dimensional depth structure of the crust beneath the Tohoku District, I. Method and Conrad Discontinuity*. J. Phys. Earth, 30, 47-69.
- Humphreys E., Clayton R.W. and Hager B.H. (1984): *A tomographic image of a mantle structure beneath Southern California*. Geophys. Res. Lett., 11, 7, 625-627.
- Inoue H. (1993): *Teleseismic tomography: global modeling*. In Seismic tomography: theory and practice, edited by H.M. Iyer and K. Hirahara (Chapman and Hall, London), 133-162.
- Inoue H., Fukao Y. Tanabe K. and Ogata Y. (1990): *Whole mantle P:wave travel time tomography*. Phys. Earth Planet. Inter., 59, 294-328.
- Iyer H.M and Hirahara K. (1993): *Seismic tomography. Theory and practice*. Chapman and Hall, London, 842-851.
- Jannane M., Beydoun W., Crase E., Cao D., Koren Z., Landa E., Mendes M., Pica A., Noble M., Roeth G., Singh S., Snieder R. Tarantola, A. Trezeguet, D. and Xie M. (1989): *Wavelength of earth structure that can be resolved from seismic reflection data*. Geophysics 54, 906-910.
- Jeffreys H. and Bullen K.E. (1940): *Seismological tables*. British association for the Advancement of Science, London.
- Jervis M., Sen V. and Porsani M. (1994): *Robust and efficient 3:D traveltimes calculations in arbitrary media*. Proceedings of the 64th Annual Meeting of the Society of Exploration Geophysicists, Los Angeles, CA (USA).
- Jordan T.H. and Lynn W.S. (1974): *A velocity anomaly in the lower mantle*. J. Geophys Res., 79, 2679:2685.
- Julian B.R. and Sengupta M.K. (1973): *Seismic travel time evidence for lateral inhomogeneity in the deep mantle*. Nature, 242, 443-447.
- Julian B.R. and Gubbins D. (1977): *Three:dimensional seismic ray tracing*. J. Geophys., 43, 95-114.
- Kastens, K., et al. (1988): *ODP Leg 107 in the Tyrrhenian Sea: Insights into passive margin and back-arc basin evolution*, Geol. Soc. Am. Bull., 100, 1140-1156.

- Kaufmann, R.D. and Long, L.T., (1996): *Velocity structure and seismicity of south eastern Tennessee*, J. geophys. Res., 101, 8531-8542.
- Kissling E. (1988): *Geotomography with local earthquake data*. Rev. Geophys., 26, 659-698.
- Kissling E. and Lahr J.C. (1991): *Tomographic image of the Pacific slab under southern Alaska*. Eclogae Geol. Helv., 84/2, 297-315.
- Kissling E., Ellsworth W.L., Eberhart-Philips D. and Kradolfer U. (1994): *Initial reference models in local earthquake tomography*. J. Geophys. Res., 99, 19635-19646.
- Kissling E., Husen S. and Haslinger F. (2001): *Model parametrization in seismic tomography: a choice of consequence for the solution quality*. Phys. Earth Planet. Int., 123, 89-01.
- Klein W F (2002): *HYPONVERSE-2000, a Fortran program to solve for earthquake locations and magnitudes*. U.S.G.S. Open- file rep., 02-171.
- Kohler M.D. and Tanimoto T. (1991): *Nature of the outermost core from global inversions of SKS phases*. Eos, 72 Supplement, 200.
- Kosloff D. and Baysal E. (1982): *Forward modeling by a Fourier method*. Geophysics, 47, 1402-412.
- Kosloff D., Reshef M. and Loewenthal D. (1984): *Elastic wave calculation by the Fourier method*. Bull. Seism. Soc. Am., 74, 875-91.
- Kovach R.L. (1979): *Seismic surface waves and crustal and upper mantle structure*. Rev. Geophys. Space Phys., 16, 1-3.
- Lallemand S. Heuret A. Faccenna C. and Funicello F. (2008): *Subduction dynamics as revealed by trench migration*. Tectonics, Vol. 27, Tc3014, Doi:10.1029/2007tc002212
- Lawson C.L., Hanson R.J. (1974). *Solving Least Squares Problems*. Prentice Hall, Englewood Cliffs, NJ.
- Lee W.H.K., Pereyra V. (1993): *Mathematical introduction to seismic tomography*. In Seismic tomography: theory and practice, edited by H.M. Iyer and K. Hirahara (Chapman and Hall, London), 9-20.
- Lee W.H.K, Lahr J.C. (1985) *HYP071: a computer program for determining hypocenter, magnitude and first motion pattern of local earthquake*. U.S.G.S. Open- file rep., 75-311.
- Lees J.M. and Crosson R.S. (1989): *Tomographic inversion for three-dimensional velocity structure at Mount St. Helens using earthquakes data*. J. Geophys. Res., 94, 5716:5728.
- Lees J.M. and VanDecar J.C. (1991): *Seismic tomography constrained by Bouguer gravity anomalies: applications in western Washington*, Pure appl. Geophys., 135, 31-52.
- Leven J.H. (1985): *The application of synthetic seismograms to the interpretation of the upper mantle P-wave velocity structure in northern Australia*. Phys. Earth Plan. Int., 38, 9-27.
- Levshin A.L., Ritzwoller M.H. and Ratnikova L.I. (1994): *The nature and cause of polarization anomalies of surface waves crossing Northern and Central Eurasia*. Geophys. J. Int., 117, 577-590.
- Lines L.R. (1988): *Inversion of geophysical data*. Geophysics Reprints No. 9, Society of Exploration Geophysicists, Tulsa, OK, USA.
- Lines L.R. (1991): *Applications of tomography to borehole and reflection seismology*. The Leading Edge, 10(7), 11-17.
- Lo T.W., Duckworth G.L. and Toksöz M.N. (1990): *Minimum cross entropy seismic diffraction tomography*. J. Acoust. Soc. Am., 87, 748-756.
- Madariaga R. (1972): *Toroidal free oscillations of the laterally heterogeneous Earth*. Geophys. J.R. Astron. Soc., 27, 81-100.
- Lognonné P. and Romanowicz B. (1990): *Modelling of coupled normal modes of the Earth: the spectral method*. Geophys. J. Int., 102, 365-396.
- Lucente F.P., Chiarabba C., Cimini G.B., and Giardini D. (1999): *Tomographic constraints on the geodynamic evolution of the Italian region*, J. Geophys. Res., 104(B9), 20,307-20,327.
- Madariaga R. (1983): *Earthquake source theory. A review*. In Earthquakes, observation theory and interpretations, edited by H. Kanamori and E. Boschi (The Enrico Fermi Summer School of Physics, 55th course, Amsterdam, The Netherlands), 1-44.
- Madariaga R. (1984): *Gaussian beam synthetic seismograms in a vertically varying medium*. Geophys. J.R. Astron. Soc., 79, 589-612.
- Madariaga R. and Aki K. (1972): *Spectral splitting of toroidal free oscillations due to the lateral heterogeneity of the Earth's structure*. J. Geophys. Res., 77, 4421-4431.
- Malinverno, A., and Ryan W.B.F. (1986): *Extension in the Tyrrhenian sea and shortening in the Apennines as result of arc migration driven by the sinking of the lithosphere*, Tectonics, 5, 227-245.
- Marani, M. P., and Trua T. (2002): *Thermal constriction and slab tearing at the origin of a super-inflated spreading ridge, Marsili Volcano (Tyrrhenian Sea)*, J. Geophys. Res., 107(B9), 2188, doi:10.1029/2001JB000285.
- Menke W. (1984): *Geophysical data analysis: discrete inverse theory*. Academic Press Inc., New York, 260, 1989
- McCann D.M., Baria R., Jackson P.D. and Green S.P.D. (1986): *Applications of cross-hole seismic measurements in site investigation surveys*. Geophysics, 51, 914-929.

- McMechan G.A. (1983): *Seismic tomography in boreholes*. Geophys. J. R. Astr. Soc., 74, 637-648.
- Michellini A. and McEvelly T.V. (1991): *Seismological studies at Parkfield. I. Simultaneous inversion for velocity structure and hypocenters using cubic B-splines parameterization*. Bull. Seism. Soc. Am., 81, 524-552.
- Michellini, A., (1993): *Velocity model inversion using parametric curves*, Geophys. J. Int. 115, 337-343.
- Michellini, A (1995): *An adaptive:grid formalism for travelttime tomography*, Geophys. J. Int. 121, 489-510.
- Montagner J.P. (1985): *Regional three:dimensional structures using long:period surface waves*. Ann. Geophys., 4, 283-294.
- Montagner J.P. and Jobert N. (1988): *Vectorial tomography : II. Application to the Indian Ocean*. Geophys. J., 94, 309-344.
- Montagner J.P. and Tanimoto T. (1990): *Global anisotropy in the upper mantle inferred from the regionalisation of phase velocities*. J. Geophys. Res., 95, 4797-4819.
- Montuori C., Cimini G.B., Favali P. (2007): *Teleseismic tomography of the southern Tyrrhenian subduction zone: new results from seafloor and land recordings*. J. Geoph. Res., 112 (B0) 3311 doi:10.129/2005JB004114
- Mora P. (1987): *Nonlinear two:dimensional elastic inversion of seismic data*. Geophysics, 52, 1211-1228.
- Morelli, C. (1970): *Physiography, gravity and magnetism of the Tyrrhenian Sea*, Bol. Geofis. Teor. Appl., 12(48), 275-311.
- Morelli, C. (1997): *Recent deeper geophysical results better account for the tectonics in the Italian area*, Ann. Geophys., 40, 1345-1358.
- Nakanishi I. (1985): *Three:dimensional structure beneath the Hokkaido:Tohoku region as derived from a tomographic inversion of P:arrival times*. J. Phys. Earth, 33, 241-256.
- Nataf H.C., Nakanishi I. and Anderson D.L. (1986): *Measurements of mantle wave velocities and inversion for lateral heterogeneities and anisotropy. 3. Inversion*. J. Geophys. Res., 91, 7261-7307.
- Newton R.G. (1966): *Scattering theory of waves and particles*. McGraw:Hill, New York, 681.
- Nolet G. (1977): *The upper mantle under Western Europe inferred from the dispersion of Rayleigh modes*. J. Geophys., 43, 265-286.
- Nolet G. (1981): *Linearized inversion of (teleseismic) data*. In The solution of the inverse problem in geophysical interpretation, edited by R.Cassinis (Plenum, New York), 9-37.
- Nolet G. (1983): *Inversion and resolution of linear tomographic systems*. Eos, Trans. AGU, 64, 775-776.
- Nolet G. (1985): *Solving or resolving inadequate and noisy tomographic systems*. J. Comput. Phys., 61, 463:482.
- Nolet G. (1987a): *Waveform tomography*. In Seismic tomography, edited by G. Nolet (Reidel Publ. Comp., Dordrecht, The Netherlands), 301-323.
- Nolet G. (1987b): *Seismic wave propagation and seismic tomography*. In Seismic tomography, edited by G. Nolet (Reidel Publ. Comp., Dordrecht, The Netherlands), 1-14.
- Nolet G. (1987c): *Seismic tomography*. Reidel Publ. Comp., Dordrecht, The Netherlands.
- Nolet G. (1990): *Partitioned wave form inversion and 2D structure under the NARS array*. J. Geophys. Res., 95, 8499-8512.
- Nolet G. (1993a): *Solving large linearized tomographic problems*. In Seismic tomography: theory and practice, edited by H.M. Iyer and K. Hirahara (Chapman and Hall, London), 227-247.
- Nolet G. (1993b): *Imaging the upper mantle with partitioned non:linear waveform inversion*. In Seismic tomography: theory and practice, edited by H.M. Iyer and K. Hirahara (Chapman and Hall, London), 248-264.
- Nolet G. and Snieder R. (1990): *Solving large linear inverse problems by projection*. Geophys. J. int., 103, 565-568.
- Nolet G. (1996): *A general view of the seismic inverse problem*. In Seismic modelling of Earth's structure, edited by E. Boschi, G. Ekström G. and A. Morelli for Istituto Nazionale di Geofisica (Editrice Compositori, Bologna), 1-29.
- Novotny M. (1981): *Two methods of solving the linearized two:dimensional inverse seismic kinematic problem*. J. Geophys., 50, 7-15.
- Nur A. and Wang Z. (1989): *Seismic and Acoustic Velocities in Reservoir Rocks, Volume 1: Experimental studies*. SEG Publications, Tulsa, OK, USA, 405.
- Okal E.A. and Anderson D.L. (1975): *A study of lateral heterogeneities in the upper mantle by multiple ScS travel time residuals*. Geophys. Res. Lett., 2, 313-316.
- Oakley, A.J., Taylor, B., Fryer, P., Moore, G.F., and al., e. (2007): *Emplacement, growth, and gravitational deformation of serpentinite seamounts on the Mariana forearc*: Geophysical Journal International, v. 170, 615-634.
- Oppenheimer, D.H. and Herkenhoff, K.E., (1981): *Velocity density properties of the lithosphere from three-dimensional modeling at the Geysers-Clear Lake region, California*, J. geophys. Res., 86, 6057-6065.
- Paige C.C. and Saunders M.C. (1982): *LSQR: an algorithm for sparse linear equations and sparse least squares*. ACM Trans. Math. Soft., 8, 43-71.

- Panza G.F., Peccerillo A., Aoudia A., Farina B. (2007): *Geophysical and petrological modeling of the structure and composition of the crust and upper mantle in complex geodynamic setting. The Tyrrhenian sea and surroundings*. Earth Sci. Rev., 80, 1-46.
- Pasquale V., Verdoya M., Chiozzi P. (2005): *Thermal structure of the Ionian slab*. Pure and Appl. Geophys. 162, 967-986.
- Pascucci, V., S. Merlini, and Martini P. (1999): *Seismic stratigraphy of the Miocene-Pleistocene sedimentary basin of the northern Tyrrhenian Sea and western Tuscany (Italy)*, Basin. Res., 11, 337-356.
- Patacca E., and Scandone P. (1989): *Post-Tortonian mountain building in the Apennines, the role of the passive sinking of a relic lithosphere*, in *The Lithosphere in Italy: Advances in Earth Sciences Research*, vol. 80, edited by A. Boriani, et al., Acc. Naz. Lincei, Rome, 157-176.
- Patacca E., Sartori R., and Scandone P. (1992): *Tyrrhenian basin and Apenninic arcs: Kinematic relations since late Tortonian times*, Mem. Soc. Geol. Ital., 45, 425-451.
- Pavlis G.L. and Booker J.R. (1980): *The mixed discrete:continuous inverse problem: Application to the simultaneous determination of earthquake hypocenters and velocity structure*. J. Geophys. Res., 85, 4801-4810.
- Peccerillo A. (2003): *Plio-Quaternary magmatism in Italy*. Episodes, 26, 222-226.
- Peccerillo A. (2005): *Plio-Quaternary volcanism in Italy*. Petrology, Geochemistry, Geodynamics. Springer, Heidelberg, 365.
- Peacock S.M. (1990) *Fluid processes in subduction zones*. Science 248, 329-337.
- Peacock S.M., Hyndmann R.D. (1999): *Hydrous minerals in the mantle wedge and the maximum depth of subduction thrust earthquakes*. Geophys. Res. Lett., 26, 2517-2520.
- Peacock S.M., (2001): *Are the lower planes of double seismic zones caused by serpentine dehydration in subducting oceanic mantle*, Geology 29, 299-302.
- Pepe F., Sulli A., Bertotti G., Cella F. (2008): *Crustal architecture and Miocene to Recent evolution of the W Calabria continental margin (Southern Tyrrhenian Sea)*. Ext. abs. of the Miscellanea-INGV, 3, 98-99.
- Piomallo C., and Morelli A. (1997): *Imaging the Mediterranean upper mantle by P-wave travel time tomography*, Ann. Geophys., 40, 963-979.
- Piomallo C., Morelli A. (2003): *P wave tomography of the mantle under the Alpine-Mediterranean area*. J. Geophys. Res., 108, NO. B2, 2065.
- Pontevivo A., Panza G.F. (2006): *The Lithosphere-Asthenosphere system in the Calabrian arc*. Pure and Appl. Geophys. 163, 1617-1659.
- Radon J. (1917): *Über die Bestimmung von Funktionen durch ihre Integralwerte langs gewisser Mannigfaltigkeiten*. Ber. Verh. Sächs. Akad. Wiss, Leipzig. Math. Phys. Kl., 69, 262:277.
- Rytov S.M. (1937): *Diffraction of light by ultrasonic waves*. Izv. Akad. Nauk. SSSR, Ser. Fiz. 2-223.
- Richards M.A., Hager B.H. and Sleep N.H. (1988): *Dynamically supported geoid highs over hotspots, seismic heterogeneity, and the large-scale structure of mantle convection*. J. Geophys. Res., 93, 7690-7708.
- Roecker S.W. (1981): *Seismicity and tectonics of the Pamir:Hindu Kush region of central Asia*. PhD Thesis, Massachusetts Institute of Technology, Cambridge.
- Roecker S.W. (1993): *Tomography in zones of collision: practical considerations and examples*. In Seismic tomography: theory and practice, edited by H.M. Iyer and K. Hirahara (Chapman and Hall, London), 584-612.
- Rotolo S.G., Castorina F., Cellura D., and Pompilio M. (2006): *Petrology and Geochemistry of Submarine Volcanism in the Sicily Channel Rift*, Journal of Geology, 2006, volume 114, p. 355-365
- Rosenbaum G., and Lister G.S. (2004): *Neogene and Quaternary rollback evolution of the Tyrrhenian Sea, the Apennines, and the Sicilian Maghrebides*, Tectonics, 23, TC1013, doi:10.1029/2003TC001518.
- Rupke L.H., Morgan J.P., Hort M., Connolly J.A.D. (2004): *Serpentine and the subduction zone water cycle*. Earth Planet. Sci. Lett., 223, 17-34.
- Rupke L.H., Phipps-Morgan J., Hort M., Connolly J.A.D. (2002): *Are the regional variations in Central American arc lavas due to differing basaltic versus peridotitic slab sources of fluids?* Geology 30, 1035-1038.
- Sartori R. (1989): *Evoluzione neogenico-recente del bacino tirrenico e i suoi rapporti con la geologia delle aree circostanti*, Giorn. Geol., 3(51/2), 1-39.
- Sambridge M.S. (1990): *Non-linear arrival time inversion: constraining velocity anomalies by seeking smooth models in 3:D*. Geophys. J. Int. 102, 653-677.
- Sambridge M., and Gudmundsson O. (1998): *Tomographic systems of equations with irregular cells*, J. Geophys. Res. 103, 773-781.
- Scarpa R. (1982): *Travel-time residuals and three-dimensional velocity structure of Italy*, Pure Appl. Geophys., 120, 583-606.
- Schmidt M.W. and Poli S. (1998): *Experimentally-based water budgets for dehydrating slabs and consequences for arc magma generation*. Earth and Planetary Science Letters 163, 361-379.

- Schneider W.A.Jr. (1993): *Robust, efficient upwind finite:difference traveltime calculation in 3D*. Proceedings of the 62nd Annual Meeting of the Society of Exploration Geophysicists, Washington, D.C.
- Schuster G.T. (1996): *Resolution limits for crosswell migration and traveltime tomography*. Geophys. J. Int., 127, 427-440.
- Selvaggi G., and Chiarabba C. (1995): *Seismicity and P-wave velocity image of the southern Tyrrhenian subduction zone*, Geophys. J. Int., 121, 818-826.
- Sen M.K., Frazer L.N., Chapman N.R. and Mallick S. (1988): *Analysis of multipath sound propagation in the ocean*. J. Acoust. Soc. Am., 83(2), 588-597.
- Sengupta M.K. (1975): *Three dimensional velocity model of the Earth mantle*. Eos, Trans. Am. Geophys. Union, 56, 395.
- Sengupta M.K. and Toksöz M.N. (1976): *Three dimensional model of seismic velocity variation in the Earth's mantle*. Geophys. Res. Lett., 3, 84-86.
- Sengupta M.K., Hassel R.E. and Ward R.W. (1981): *Three:dimensional seismic velocity structure of the Earth's mantle using body wave travel times from intra:plane and deep:focus earthquakes*. J. Geophys. Res., 86, 3913-3934.
- Shelly D.R., Beroza G.C., Zhang H., Thurber C.H., Ide S. (2006): *High-resolution subduction zone seismicity and velocity structure beneath Ibaraki Prefecture, Japan*, J. Geophys. Res., 111, B06311, doi:10.1029/2005JB004081.
- Sipkin S.A. and Jordan T.H. (1976): *Lateral heterogeneity of the upper mantle determined from travel times of multiple ScS*. J. Geophys. Res., 81, 6307-6319.
- Snieder R. (1988a): *Large:scale waveform inversions of surface waves for lateral heterogeneity, 1, Theory and numerical examples*. J. Geophys. Res., 93, 12055-12065.
- Snieder R. (1988b): *Large:scale waveform inversions of surface waves for lateral heterogeneity, 2, Application to surface waves in Europe and the Mediterranean*. J. Geophys. Res., 93, 12067-12080.
- Snieder R. (1993): *Global inversions using normal modes and long:period surface waves*. In Seismic tomography: theory and practice, edited by H.M. Iyer and K. Hirahara (Chapman and Hall, London), 23-63.
- Snieder R. and Sanbridge M. (1992): *Ray perturbation theory for travel times and ray paths in 3D heterogeneous media*. Geophys. J. Int., 109, 294-322.
- Snieder R. and Sanbridge M. (1993): *The ambiguity in ray perturbation theory*. J. Geophys. Res., 98, 22021-22034.
- Snieder R., Xie M.J., Pica A. and Tarantola A. (1989): *Retrieving both the impedance contrast and background velocity: A global strategy for the seismic reflection problem*. Geophysics, 54, 991-1000.
- Sonneveld P. (1989): *CGS, a fast Lanczos:type solver for nonsymmetric linear systems*. SIAM J. Sci. Statist. Comput., 10, 36-52.
- Spakman W. and Nolet G. (1988): *Imaging algorithms, accuracy and resolution in delay time tomography*. In Mathematical geophysics, edited by N.J. Vlaar, N. Nolet, M.J.R.. Worthel and S. Cloetingh et al. (Reidel Publ. Comp., Dordrecht, The Netherlands), 155.187.
- Spakman, W. (1990): *Tomographic images of the upper mantle below central Europe and the Mediterranean*, Terra Nova, 2, 542-552.
- Spakman W. (1993): *Iterative strategies for non:linear travel time tomography using global earthquake data*. In Seismic tomography: theory and practice, edited by H.M. Iyer and K. Hirahara (Chapman and Hall, London), 190-226.
- Spakman W., Stein S., Van der Hilst R.D. and Wortel R. (1993): *Resolution experiments for NW Pacific subduction zone tomography*. Geophys. Res. Lett., 16, 1097-1101.
- Spakman W., Van der Lee S. and Van der Hilst R.D (1993): *Travel:time tomography of the European:Mediterranean mantle down to 1400 km*. Phys. Earth Planet. Int., 79, 3-74.
- Spakman, W., and Wortel R. (2004): *A tomographic view on western Mediterranean Geodynamics*, in The Transmed Atlas, Springer, New York,31-52.
- Spencer C. and Gubbins D. (1980): *Travel:time inversions for simultaneous earthquake location and velocity structure in laterally varying media*. Geophys. J.R. Astron. Soc., 63, 95-116.
- Tabbara W., Duchêne B., Pichot Ch., Lesselier D., Chommeloux L. and Joachimowicz N. (1988): *Diffraction tomography: contribution to the analysis of some applications in microwaves and ultrasonics*. Inverse Problems, 4, 305-331.
- Tanimoto T. (1987): *The three:dimensional shear:wave structure in the mantle by overtone waveform inversion : 1. Radial seismogram inversion*. Geophys. J.R. Astron. Soc., 89, 713-740.
- Tanimoto T. (1990): *Long:wavelength S:wave velocity structure throughout the mantle*. Geophys. J. Int., 100, 327-336.
- Tanimoto T., Anderson D.L. (1984): *Mapping convection in the mantle*. Geophys. Res. Lett., 11, 287-290.
- Tanimoto T., Anderson D.L. (1985): *Lateral heterogeneity and azimuthal anisotropy of the upper mantle: Love and Rayleigh waves 100:250 s*. J. Geophys. Res., 90, 1842-1858.

- Tarantola A. (1984): *Inversion of seismic reflection data in the acoustic approximation*. Geophysics, 49, 1259-1266.
- Tarantola A. (1986): *A strategy for nonlinear elastic inversion of seismic reflection data*. Geophysics, 51, 1893-1903.
- Tarantola A. (1987): *Inverse problem theory: methods for data fitting and model parameter estimation*. Elsevier, Amsterdam.
- Tarantola A. (1988): *Theoretical background for the inversion of seismic waveform, including elasticity and attenuation*. Pure Appl. Geophys., 128, 365-399.
- Tarantola A. and Nercessian A. (1984): *Three-dimensional inversion without blocks*. Geophys. J.R. Astron. Soc., 76, 299-306.
- Tarantola A. and Valette B. (1982): *Generalized nonlinear inverse problems solved using the least squares criterion*. Rev. Geophys. Space Phys., 20, 219-232.
- Tarantola A., Koren Z. and Crase E. (1993): *Tomography using waveform fitting of body waves*. In Seismic tomography: theory and practice, edited by H.M. Iyer and K. Hirahara (Chapman and Hall, London), 781-796.
- Thurber C.H. and Ellsworth W.L. (1980): *Rapid solution of ray-tracing problems in heterogeneous media*. Bull. Seism. Soc. Am., 70, 1137-1148.
- Thurber C.H. (1981): *Earth structure and earthquake locations in the Coyote Lake area, central California*. PhD Thesis, Massachusetts Institute of Technology, Cambridge.
- Thurber C.H. (1983): *Earthquake locations and three-dimensional crustal structure in the Coyote Lake area, central California*. J. Geophys. Res., 88, 8226-8236.
- Thurber C.H. (1986): *Analysis methods for kinematic data from local earthquakes*. Rev. Geophys., 24, 793-805.
- Thurber C.H. (1993): *Local earthquake tomography: velocities and V_p/V_s : theory*. In Seismic tomography: theory and practice, edited by H.M. Iyer and K. Hirahara (Chapman and Hall, London), 563-583.
- Thurber C.H. and Aki K. (1987): *Three-dimensional seismic imaging*. Ann. Rev. Earth Planet. Sci., 15, 115-139.
- Thurber C.H. and Eberhart-Phillips (1999): *Local earthquake tomography with flexible gridding*. Comput. Geosci. 23, 809-818.
- Thurber C.H. and Kissling E. (2000): *Advances in travel time calculations for three-dimensional structures*. In Advances in Seismic Event Location, edited by C.H. Thurber and N. Rabinowitz (Kluwer, Dordrecht, The Netherlands), 1-29.
- Toksöz M.N. and Anderson D.L. (1966): *Phase velocities of long-period surface waves and structure of the upper mantle*. J. Geophys. Res., 71, 1649-1667.
- Tommasini S., Heumann A., Avanzinelli R., Francelanci L. (2007): *The fate of high-angle dipping slabs in the subduction factory: an integrated trace element and radiogenic isotope (U, Th, Sr, Nd, Pb) study of Stromboli Volcano, Aeolian Arc, Italy*. Jour. Petrol., 48, 2407-2430.
- Tondi R. and de Franco R. (2006): *Accurate assessment of 3-D crustal velocity and density parameters: application to Vesuvius data sets*. Physics Earth Planetary Interiors, 159, 183-201.
- Toomey D R, Foulger G R (1989): *Tomography inversion of local earthquake data from the Hengill: Grensdalur central volcano complex, Iceland*. J. Geophys. Res., 94 B12, 17497-17510.
- Tromp J. and Dahlen F.A. (1990): *Summation of the Born series for the normal modes of the Earth*. Geophys. J. Int., 100, 527-534.
- Tromp J. and Dahlen F.A. (1992): *Variational principles for surface wave propagation on a laterally heterogeneous Earth: I. Time domain JWKB theory*. Geophys. J. Int., 109, 581-598.
- Turcotte, D. L. and Schubert, G. (1971): *Schubert, Structure of the olivine-spinel phase boundary in the descending lithosphere*. J. geophys. Res. 76, 7980-7987.
- Ulmer P., Trommsdorff V. (1995): *Serpentine stability to mantle depths and subduction-related magmatism*. Science 268, 858-861.
- Ulmer P., Trommsdorff V. (1999): *Phase relations of hydrous mantle subducting to 300 km*. In: Fei Y. W., Bertka C., & Mysen B. (eds) Mantle petrology: field observations and high pressure experimentation: a tribute to Francis R. (Joe) Boyd. Geochemical Society Special Publications 6, 259-281.
- Um J. and Thurber C.H. (1987): *A fast algorithm for two-point seismic ray tracing*. Bull. Seism. Soc. Am., 77, 972-986.
- Van der Sluis A. and Van der Vorst H.A. (1987): *Numerical solution of large, sparse linear algebraic systems arising from tomographic problems*. In Seismic tomography, edited by G. Nolet (Reidel Publ. Comp., Dordrecht, The Netherlands), 49-84.
- Vesnaver, A. (1996): *Irregular grids in seismic tomography and minimum-time ray tracing*, Geophys. J. Int. 126, 147-165.
- Vernant P., Masson F., Bayer R. and Paul A. (2002): *Sequential inversion of local earthquake traveltimes and gravity anomaly—the example of the western Alps*, Geophys. J. Int. 150, 79-90

- Walck M.C. and Clayton R.W. (1987): *P wave velocity variations in the Coso Region, California, derived from local earthquake travel times*. J. Geophys. Res., 92, 393-405.
- Waldhauser, F., and Ellsworth W.L. (2000): *A double-difference earthquake location algorithm: Method and application to the Northern Hayward Fault, California*, Bull. Seism. Soc. Am. 90, 1353-1368.
- Waldhauser, F. (2001): *hypoDD A computer program to compute double-difference hypocenter locations*, U.S. Geol. Surv. Open File Rep. 01-113, 25.
- Wesson R.L. (1971): *Travel:time inversion for laterally inhomogeneous crustal velocity models*. Bull. Seism. Soc. Am., 61, 729-746.
- Wielandt E. and Knopoff L. (1982): *Dispersion of very long:period Rayleigh waves along the East Pacific Rise: Evidence for S wave velocity anomalies to 450 km depth*. J. Geophys. Res., 87, 8631-8641.
- Williamson P.R. (1991): *A guide to the limits of resolution imposed by scattering in ray tomography*. Geophysics, 56, 202-208.
- Woodhouse J.H. and Dziewonski A.M. (1984): *Mapping the upper mantle: three-dimensional modelling of earth structure by inversion of seismic waveforms*. J. Geophys. Res., 89, 5953-5986.
- Wu R.S. and Toksöz M.N. (1987): *Diffraction tomography and multi:source holography applied to seismic imaging*. Geophysics 52, 11-25.
- Zeyen H. and Achauer U., (1997): *Joint inversion of teleseismic delay times and gravity anomaly data for regional structures: theory and synthetic examples*, in NATO Science Series, Partnership Subseries 1, Disarmament Technologies, 17, 155-168.
- Zhang H., Thurber C.H. (2003): *Double-difference tomography: The method and its application to the Hayward fault, California*. Bull. Seism. Soc. Am. 93, 1175-1189.
- Zhang H., Thurber C.H., Shelly D., Ide S., Beroza G.C., Hasegawa A. (2004): *High-resolution subducting-slab structure beneath northern Honshu, Japan, revealed by double-difference tomography*. Geology, 32, 4, 361-364.
- Zhang H. and Thurber C. (2005): *Adaptive mesh seismic tomography based on tetrahedral and Voronoi diagrams: Application to Parkfield, California* Journal of Geophysical Research, Volume 110, Issue B4, CiteID B04303
- Zhao D. (1991): *A tomographic study of seismic velocity structure in the Japan islands*. PhD Thesis, Tohoku Univ., 301.
- Zhao D., Hasegawa A. and Horiuchi S. (1992): *Tomographic imaging of P and S wave velocity structure beneath northeastern Japan*. J. Geophys. Res., 97, 19909-19928.
- Zhao D., Horiuchi S. and Hasegawa A. (1992): *3:D seismic velocity structure of the crust and the uppermost mantle in the northeastern Japan Arc*. Tectonophys., 181, 135-149.
- Zhou C., Cai W., Luo Y., Schuster G.T. and Hossanzadeh S. (1995): *Acoustic wave equation travelttime and waveform inversion of crosswell data*. Geophysics, 60, 765-773.
- Zhou C., Schuster G.T., Hassanzadeh S. and Harris J.M. (1997): *Elastic wave equation travelttime and waveform inversion of crosswell data*. Geophysics, 62, 853-868.

List of the Publications

M. Calò, C. Dorbath, D. Luzio, S. Rotolo, D'Anna G. (2009): Local Earthquakes Tomography in the southern Tyrrhenian region: geophysical and petrological inferences on subducting lithosphere.

Subduction Zone Dynamics Series: Frontiers in Earth Sciences

Lallemand, Serge; Funiciello, Francesca (Eds.), XX, 276 ISBN: 978-3-540-87971-8. DOI 10.1007/978-3-540-87974-9

G. Giunta, S. Orioli, A. Giorgianni, F. Di Trapani, D. Luzio, M. Calò. (2008): Il Terremoto Di Messina Del 1908 In Un Modello Sismotettonico Della Sicilia Settentrionale E Del Basso Tirreno

Extended Abstract of the 27° Work-Shop Miscellanea INGV 1908 – 2008 Scienza e Società a cento anni dal Grande Terremoto Reggio Calabria 10-12 December 2008 pp. 63-64.

G. D'Anna, G. Mangano, A. D'Alessandro, R. D'Anna, G. Passafiume, S. Speciale, G. Selvaggi, L. Margheriti, D. Patanè, D. Luzio, M. Calò. (2008): "Messina 1908-2008" Progetto Di Ricerca Integrato Sull'area Calabro – Peloritana: La Campagna Obs/H

Extended Abstract of the 27° Work-Shop Miscellanea INGV 1908 – 2008 Scienza e Società a cento anni dal Grande Terremoto Reggio Calabria 10-12 December 2008 pp. 45-46.

M. Calò, D. Luzio, M. Vitale, G. D'Anna. (2008): Tomografia WAM integrata dell'area sud-tirrenica e siciliana.

Extended Abstract of the 27° Work-Shop GNGTS, Trieste, 6-8 October 2008 pp. 120-124.

M. Calò, G. Giunta, D. Luzio, S. Orioli, A. Giorgianni, F. Di Trapani. (2008): Schema sismo tettonico preliminare della zona di cerniera tra Sicilia settentrionale e basso Tirreno.

Extended Abstract of the 27° Work-Shop GNGTS, Trieste, 6-8 October 2008 pp. 117-120.

G. Adelfio, M. Calò, M. Chiodi, G. Giunta, D. Luzio. (2008): Stima semi-parametrica della funzione di intensità di un processo di punto spazio-temporale.

Extended Abstract of the 27° Work-Shop GNGTS, Trieste, 6-8 October 2008 pp. 11-15.

M. Calò, C. Dorbath, D. Luzio, S.G. Rotolo, G. D'Anna. (2008): WAM tomography in the southern Tyrrhenian region. petrological inferences and hypotheses on the fluid circulation in the subducting Ionian slab and adjoining mantle domain.

Bollettino di Geofisica Teorica ed Applicata 2008. vol.42, N2 pp. 136-141.

G. Adelfio, **M. Calò**, M. Chiodi, F. Di Trapani, G. Giunta, D. Luzio, E. Oliveri, S. Orioli, M. Perniciaro, M. Vitale. (2008): **Un tentativo di analisi integrata della tettonica e sismicità nella zona di cerniera tra Sicilia settentrionale e basso Tirreno.**

Rendiconti Società Geologica Italiana, annual meeting 2008, vol. 1 pp 5-8.

G. Giunta, D. Luzio, F. Agosta, **M. Calò**, F. Di Trapani, A. Giorgianni, E. Oliveri, S. Orioli, M. Perniciaro, M. Vitale, M. Chiodi, G. Adelfio. (2008): **An integrated approach to the relationships between tectonics and seismicity in northern Sicily and southern Tyrrhenian.**

Tectonophysics. doi:10.1016/j.tecto.2008.09.031

M. Calò, C. Dorbath, D. Luzio, S. G. Rotolo, G. D'Anna. (2007): **Local earthquakes tomography in the southern Tyrrhenian region (Italy): geophysical and petrological inferences on the subducting lithosphere**

AGU FALL MEETING, San Francisco 10-14 December 2007. Abstract in CD-ROM.

M. Calò, G. Adelfio, M. Chiodi, F. Di Trapani, G. Giunta, D. Luzio, E. Oliveri, S. Orioli, M. Vitale. (2007): **Relazioni tra sismicità e tettonica nel margine settentrionale della Sicilia.**

Extended abstract of the 26° Work-Shop GNGTS, Roma, 13-15 November 2007 pp. 230-233.

M. Calò, D. Luzio, M. Vitale. (2007): **Tomografia sismica WAM. Alcuni confronti con tecniche di inversione tradizionale.**

Extended abstract of the 26° Work-Shop GNGTS, Roma, 13-15 November 2007 pp. 527-529.

G. Giunta, A. Giorgianni, E. Oliveri, P. Renda, F. Di Trapani, S. Orioli, M. Perniciaro, M. Alagna, **M. Calò**. (2007): **Una ricostruzione dell'ordine sequenziale delle deformazioni nel margine settentrionale della Sicilia e implicazioni sismotettoniche.**

Abstract of the Work-Shop: The Control of the Mesozoic paleomargin architecture on the Pliocene orogenic system of the central Apennines, Camerino, giugno 2007.

M. Calò, C. Dorbath, D. Luzio, S. Rotolo. (2007): **Modelling of the subducting slab beneath the South Tyrrhenian basin with geophysical and geochemical data.**

Abstract of the 1° Work-Shop SUB.CO, Montpellier, 4-8 June 2007 pp. 57.

M. Calò, R. Davì, C. Dorbath, D. Luzio. (2006): Tomographic images of the Ionian slab by using the tomoDD algorithm.

AGU FALL MEETING, San Francisco, 11-15 December 2006. Abstract in CD-ROM.

M. Calò, R. Davì, C. Dorbath, D. Luzio. (2006): **Tomografia sismica passiva nell'area dell'arco Calabro e del Tirreno sud-orientale.**

Extended abstract of the 25° Work-Shop GNGTS, Roma, 28-30 November 2006 pp 80-81.

